ELECTRICAL TRANSPORT PROPERTIES OF TWO-DIMENSIONAL HOLE GASES IN THE $Si/Si_{1-x}Ge_x$ SYSTEM

BY

CHARLES JOHN EMELEUS

Thesis submitted in partial fulfilment of the requirements for the award of the degree of Doctor of Philosophy by the University of Warwick

Department of Physics,

University of Warwick

April 1993

SUMMARY

This thesis is a report of experimental investigations of hole transport properties in quantum wells formed in Si/SiGe heterostructures grown by Molecular Beam Epitaxy. Initial work was concerned with elucidating the dominant hole scattering mechanisms, the aim being to relate this to the growth conditions and consequently produce enhanced mobility material for further study. Accordingly, low temperature resistance and Hall measurements (down to 4 K) were undertaken, in order to minimise the effect of phonon scattering.

The first samples exhibited strongly localised hole states at liquid helium temperatures, but subsequently, the introduction of growth interrupts as well as the use of higher growth temperatures was shown to give rise to conduction by extended states, with a maximum 5 K mobility of nearly 4000 $cm^2V^{-1}s^{-1}$. Interface impurities at the Si/SiGe heterojunction with a density of 2×10^{11} cm^{-2} are shown to be responsible for the typical carrier mobility of 2000 $cm^2V^{-1}s^{-1}$ obtained in structures grown at 550 °C, and using a model developed by the author this density is found to be consistent with the dependence of experimental data on structural and doping parameters.

Magnetotransport measurements carried out in fields up to 12 T in strength and at temperatures down to 0.3 K yielded the first observation of weak localisation and carrier-carrier interaction phenomena in this materials system. It is possible to confirm that strain lifts the light hole and heavy hole band degeneracy associated with unstrained Si. In addition, a temperature dependence of the Boltzmann conductivity is observed and attributed to the variation of screening efficiency with thermal disorder. Deviations from the expected lnT dependence of the Hall coefficient in the presence of enhanced interaction phenomena might be understood in terms of a recent theory for the weak localisation correction to the Hall conductivity near the metal-insulator transition.

CONTENTS

FIGURES AND TABLES

FIGURES

TABLES

ACKNOWLEDGEMENTS

First of all I would like to thank my supervisor, Dr. T.E. Whall, for his valuable guidance during the course of the research. I am also very grateful to Dr. M.J. Kearney (of G.E.C. Hirst Research Labs) for his comments on the low temperature transport data in the context of current theories. Dr. R.A. Kubiak grew all the material used in the research and I would like to thank him for this. D.W. Smith fabricated the Hall bars used for experiments in the cryomagnetic system and made a very significant contribution to the growth study. Prof. E.H.C. Parker also provided a lot of useful information in the early growth related stages of the work. I would like to acknowledge other members of the my research group (present and former), who have helped with all my enquiries: notably Dr. R.G. Biswas, Dr. N.L. Mattey, J.C. Brighten, E. Basaran, Dr. C.P. Parry, A.D. Plews and G. Braithwaite. Essential technical support was provided by T. Naylor and R. Morris, for which I am very grateful.

I would like to acknowledge my financial sponsors, the UK SERC and British Telecom, who provided me with a CASE award. In addition, the SERC paid my expenses incurred attending the 1992 Spring Meeting of the European MRS in Strasbourg. This enabled me to present a poster, make useful contacts and acquire a general knowledge of the Si/SiGe materials field.

DECLARATION

This thesis is the result of research carried out by the author in the Department of Physics, University of Warwick between October 1989 and March 1993 and is submitted as partial fulfilment of the requirements for the award of the degree of Doctor of Philosophy. The work described here is all my own, except where acknowledged as otherwise in the text.

A large amount of the work has been accepted for publication in the form of journal articles, as follows:

Emeleus, C.J., Whall, T.E., Smith, D.W., Kubiak, R.A., Parker, E.H.C. and Kearney, M.J., "Hole transport in $Si_{0.8}Ge_{0.2}$ quantum wells at low temperatures", Thin Solid Films (1992), 222, 24 (as published proceedings of the Spring meeting of the EMRS, 1992)

Emeleus, C.J., Whall, T.E., Smith, D.W., Kubiak, R.A., Parker, E.H.C. and Kearney, M.J., "Scattering mechanisms affecting hole transport in remote-doped Si/SiGe heterostructures", J. Appl. Phys. (1993), 73, (to appear on 15/4/93)

Emeleus, C.J., Whall, T.E., Smith, D.W., Mattey, N.L., Kubiak, R.A., Parker, E.H.C. and Kearney, M.J., "Observation of novel transport phenomena in a $Si_{0.8}Ge_{0.2}$ two-dimensional hole gas", Phys. Rev. B15 (1993), 47, (to appear on 15/4/93)

Emeleus, C.J., Whall, T.E., Smith, D.W., Kubiak, R.A., Parker, E.H.C. and Kearney, M.J., "Electrical conduction in p-type modulation doped $Si/Si_{0.8}Ge_{0.2}$ quantum wells", in "Proceedings of 21st International Conference on the Physics of Semiconductors (Beijing, August 1992)", (World Scientific, Singapore)

CHAPTER ONE

INTRODUCTION AND REVIEW OF PREVIOUS WORK

1.1 CHARGE TRANSPORT IN LOW DIMENSIONAL SYSTEMS

Pioneering experimental investigations of charge transport in two dimensional (2D) systems were performed using Si MOSFETs. Electron and hole inversion layers induced at the Si/SiO_2 interfaces of these devices by the application of appropriate gate voltages typically have thicknesses of less than 10 nm, and such quantum confinement renders the charges dynamically two dimensional. The large body of information resulting from these studies, which culminated in the discovery of the integer quantum Hall effect (von Klitzing *et al.*, 1980), has been reviewed by Ando *et al.* (1982).

During the same period, significant advances were also made in crystal growth technology, possibly the most important being the application of ultra-high vacuum (UHV) techniques (available pressures as low as 10^{-11} torr) to provide much cleaner environments for epitaxy. Various growth methods using solid, liquid and gaseous starting materials were developed, but in this thesis only one of them, Molecular Beam Epitaxy (MBE), is of concern. The essence of the technique is that selected elements are evaporated from sources placed around a growth chamber, with the generated fluxes impinging on a centrally positioned substrate. Deposition rates may be set low enough such that the crystal grows in a 2D manner, with a possible thickness resolution on the

monolayer scale.

This type of crystal growth facility enables the sequential deposition of, for example, thin layers of different semiconducting materials, to form sandwich-type materials. However, due to the different bandgaps of adjacent materials, potential steps in the valence and conduction bands must be formed at the heterointerfaces. Consequently, if crystals composed of many such layers are grown, it is possible to engineer arrays of potential wells and barriers in the conduction and valence bands, such that charges introduced to these materials migrate to the potential minima, as shown in Fig. 1.1.

Fig. 1.1 Potential wells for holes and electrons in semiconductor heterostructures

This means of choosing material composition, combined with the ability to restrict the thickness of individual layers to one atomic spacing, enables electrons and holes to be quantum mechanically confined to two dimensions, in an analogous way to those in MOSFET inversion layers. However, there is much more flexibility possible in the design of these heterostructures, with the ability to vary the shape of the confining potential, by changing both layer thickness and material composition, and also the carrier population of the quantum well (in a MOSFET, the well shape and carrier density depend

on one another via the gate voltage). Furthermore, it is possible to grow multi-quantum well and superlattice structures, with the distinction between these two being that in the latter case wavefunctions of carriers in adjacent wells overlap, leading to the formation of 'mini-bands'.

In order to study charge transport, suitable doping strategies must be adopted. In many cases, a conduction band population of electrons can be induced by optical excitation using a LED or laser, but the most common method is to dope structures with impurity atoms. The nature of the potential well and barrier environment in these heterostructures has been exploited to develop a novel doping technique, which involves the doping of potential barrier regions only, from where ionised carriers transfer to adjacent potential wells (Dingle *et al.*, 1978). The significance of this spatial separation of charge carrier and ionised parent atom is that the Coulomb attraction between the two is reduced in strength, with the result that the ionised impurity scattering rate falls, leading to higher carrier mobilities. This practice is known as remote doping, but in the literature is also referred to as modulation doping, even though the latter term is used to describe much more general methods of doping.

The enhanced mobilities of electrons and holes in remotely doped (RD) quantum wells came to exceed the corresponding maximum mobilities obtained in Si MOSFET inversion layers by a couple of orders of magnitude, both as a result of the reduction of ionised impurity scattering from dopant atoms and also due to the superior interface and material quality associated with MBE. The highest known values for the four types of system (at liquid helium temperatures) are as follows.

- n-channel MOS, $\sim 4\times10^4$ $cm^2V^{-1}s^{-1}$ (Kukushkin *et al.*, 1988)
- n-channel RD (GaAs/AlGaAs), $\sim 9\times10^6$ $cm^2V^{-1}s^{-1}$ (Foxon *et al.*, 1989)
- p-channel MOS, $\sim 3\times10^3$ $cm^2V^{-1}s^{-1}$ (Gusev *et al.*, 1984)

- p-channel RD (GaAs/AlGaAs), $\sim 2\times10^5$ $cm^2V^{-1}s^{-1}$ (Mendez and Wang, 1985)

One of the important advances made with higher mobility 2DEGs, in conjunction with the availability of very low temperature (<0.1 K) refrigerators, was the discovery of fractional quanta in the Hall resistance. This phenomenon is now understood in terms of electron-electron interactions giving rise to a Fermi liquid ground state, from which quasi-particle excitations carry fractional charge [a review is given by Clark and Maksym (1989)]. Transport in 2D systems in the absence of magnetic flux is itself an area of great interest, and extensive studies were stimulated by the suggestion of Abrahams *et al.* (1979) that all carriers in a 2D metal are localised by disorder at absolute zero temperature. This weak localisation is accompanied by a disorder-induced electron-electron interaction reduction in the density of states at the Fermi energy: at low temperatures both effects lead to a reduction in the conductivity (Lee and Ramakrishnan, 1985). In addition, higher levels of disorder can induce strong localisation of carriers in systems of any dimensionality and at finite temperatures (see Mott and Davis, 1979). Disorder and magnetic field induced localisation have been discussed with reference to Si MOSFETs by Pepper (1985). A review of electrical and optical properties of quantum well structures has been given by Kelly and Nicholas (1985), while an article focusing on electrical structure and transport properties has been written by Harris *et al.* (1989).

More recent developments in the field of LDS physics have come from the application of sub-micron lithographic techniques to the fabrication of devices based on high mobility 2DEGs. It is possible to make structures in which transport is ballistic; that is, where carriers experience no scattering in transit between source and drain contacts because the elastic mean free path is larger than device dimensions (Pepper and Wharam, 1988). The study of 1D transport is also of interest and again relies on fine

scale lithographic techniques, either to produce mesa structures from a 2DHG, or to define arrays of metal gates, to which the application of suitable voltages causes depletion of most of the 2D gas, leaving just a 1D constriction (the split gate technique, developed by the Cambridge group - Thornton *et al.*, 1986). Currently, a great amount of interest is being shown in the properties of quantum point contacts, small islands with tunnel junction contacts which typically contain only a few thousand electrons. The size of these devices is such that capacitances can be as small as 10^{-15} F, and consequently the voltage needed to add or remove one electron is very large (~ 1 mV), so that the process is easily controlled. Single charge tunnelling ('Coulomb blockade') events are seen as peaks in conductance-voltage relationships and have been studied in thin metal films as well as in semiconductor heterostructures [see Kastner (1992) for an introduction to the topic].

1.2 Si/SiGe HETEROSTRUCTURES

Although the physics described in the previous section was discovered in III/V heterostructures, nevertheless some investigations of quantum well and superlattice structures based on the Si/SiGe materials system were pursued at the same time, most of these being growth oriented. The central feature of Si/SiGe hetero-epitaxy is the lattice mismatch between Si and alloy materials (the lattice constants of cubic, unstrained Si and Ge are 5.43 Å and 5.66 Å respectively), such that strain is accommodated in the epi-layers and a critical thickness exists, which if exceeded will be accompanied by relaxation (see section 3.1). The growth of SiGe on Si was first accomplished by Kasper *et al.* (1975) using MBE from solid sources. Pseudo-morphic 2D growth of single crystal $Si/Si_{1-x}Ge_x$ heterostructures (with $x < 0.2$) was successfully demonstrated, with an apparent absence of Ge interdiffusion attributed to the low growth temperature of 750 °C.

The essentials of Si/SiGe MBE are outlined in section 3.1.

There is an obvious attraction of studying low dimensional phenomena in Si, given the technological significance of the material: if advanced devices capable of exploiting the design flexibility offered by MBE and related growth techniques can be fabricated, then integration with Si-based chip technology ought to be a reasonable proposition, certainly more so than trying to deposit III/V and other classes of materials on Si [but see Lo *et al.* (1993) for an example of such attempts]. One of the exciting original proposals for the Si/SiGe system was for a superlattice structure in which the conduction band minima in the growth direction would be folded from their locations near the zone boundary into the zone centre, by careful matching of the crystalline atomic and superlattice potentials, thereby forming a direct bandgap material (Gnutzmann and Clausecker, 1974). Work on monolayer superlattices $[(Si)_n(Ge)_m$ with n and m both less than about 10 because of problems with lattice mismatch - see section 3.1.3] has been pursued vigorously, with some evidence for the existence of direct bandgap optical transitions [see the review by Presting *et al.* (1992)]. There have been reports recently of band to band transitions in photoluminescence from SiGe alloy heterostructures: the reason for this is not certain, but the origin is thought to lie with the random structural composition of SiGe alloy layers. Quantum well hole intersubband photodetectors with a broad band (8-14 μm) response have been fabricated (People *et al.*, 1992).

The focus of attention for SiGe in the arena of purely electronic device research has been with ways of making faster switching circuit components, capable of extending the overall speed of Si-chip technology. Most effort has been directed at the Heterojunction Bipolar Transistor (HBT), for which design features include heavy doping of the base to reduce the time constant in that region, and also making the base as thin as possible, as well as having a potential gradient built in by introducing a slow change in Ge

concentration, to reduce the transit time [see the review by Iyer *et al.* (1989)].

Research into devices based on parallel transport has not been so intense, as there do not appear to be such significant advantages for Si/SiGe FET devices, in terms of speed of operation, over conventional Si MOS technology. Room temperature mobility enhancements are relatively small (no more than a factor of two or so) and in any case devices are normally operated beyond the threshold region, so that a low field mobility is of little practical significance. Applications of short channel modulation doped FETs (MODFETs) fabricated from GaAs/$Al_xGa_{1-x}As$ based heterostructures include usage as very high frequency, low noise amplifiers in microwave circuits (Weisbuch and Vinter, 1991).

Both n-channel (Dämbkes *et al.*, 1986) and p-channel (Pearsall *et al.*, 1985) MODFETS have been fabricated using the $Si/Si_{1-x}Ge_x$ materials system, and recently also SiGe channel MOSFETs (Kesan *et al.*, 1991). In all cases, one of the supreme advantages of fabricating devices from Si is that a stable, passivating, surface dielectric exists in the form of SiO_2 (see section 3.1.3).

1.3 PREVIOUS STUDIES OF CHARGE TRANSPORT IN $Si/Si_{1-x}Ge_x$ QUANTUM WELL STRUCTURES

The first attempt to grow doped $Si/Si_{1-x}Ge_x$ layers was made by Manasevit *et al.* (1982) using a CVD reactor fitted with n- and p-type sources. Epi-layers were doped uniformly, but nevertheless some enhancement in carrier mobility was observed at room temperature for n-type material (20-40% and 100% increases over equivalently doped epitaxial Si and SiGe films respectively). This was provisionally attributed to strain in the alloy layers and its effect on atomic spacing in the lattice, and hence the bandstructure

and effective masses; a belief which was later shown to be well founded (see section 2.2). No mobility enhancement was observed in p-type epi-layers.

The effective use of remote doping (section 1.1) was first demonstrated for p-type Si/SiGe structures by People *et al.* (1984, 1985) at AT & T Bell Labs, with resulting hole mobilities as large as 3300 $cm^2V^{-1}s^{-1}$ at liquid helium temperatures, which is over one order of magnitude greater than in SiGe uniformly doped at an equivalent level (see Fig. 1.2).

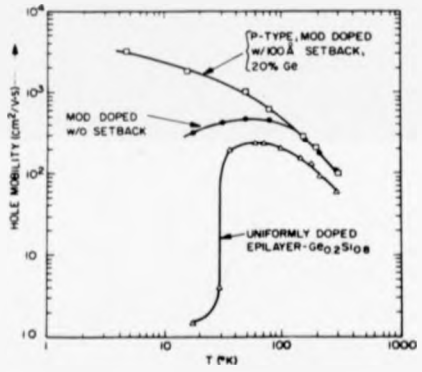

Fig. 1.2 Enhancement of mobility for a 2DHG in a remote doped SiGe quantum well as a function of temperature

The structure studied in this work was a 200 nm $Si_{0.8}Ge_{0.2}$ layer grown commensurately with a Si (100) substrate and B doped on both sides with an undoped spacer thickness of ~ 10 nm. Due to the large thickness of the SiGe layer, two independent quantum wells for holes were formed, one at each heterointerface. Confirmation of the two-dimensionality of the holes came from the large anisotropy of the magnetoresistance (see section 4.3.2.2). An estimation of the effective hole mass from the temperature dependence of Shubnikov-de Haas oscillation amplitudes yielded a value of

$(0.32\pm0.03)m_e$, significantly lower than the unstrained Si heavy-hole (HH) mass of 0.49 m_e, but larger than the light-hole (LH) mass of 0.16 m_e. This is due to strain accommodated in the alloy layer and further discussion is given in section 2.2. Doping either the Si or SiGe layers in these structures n-type did not give enhanced mobility 2DEGs, and this was taken as evidence that most of the bandgap difference is accommodated in the valence band. A solution to the problem of confining electrons was reported by Abstreiter *et al.* (1985), who found that by growing a relaxed $Si_{0.75}Ge_{0.25}$ buffer layer before depositing a $Si/Si_{0.5}Ge_{0.5}$ multi-layer structure, it was possible to strain the Si layers and thus engineer sufficient conduction band offset to trap electrons and generate 2DEGs. Raman scattering studies of these structures showed that the biaxial tensile strain in the Si lifts the six-fold conduction band degeneracy, to give four in-plane and two perpendicular states. The main drawback with using relaxed buffer layers is that misfit dislocations are propagated into the Si/SiGe heterostructure, which degrade the electrical quality of the 2DEGs.

The problem was overcome by changing the Ge concentration in the buffer very gradually, from zero at the substrate/buffer interface, up to the desired level at the buffer/heterostructure interface, and thereby dramatically reducing the density of dislocations in the 2DEG regions. This resulted in a two-decade increase of electron mobility to $\sim 2\times10^5$ $cm^2V^{-1}s^{-1}$ (Schäffler *et al.*, 1992). Magnetotransport studies of these structures have been carried out by Többen *et al.* (1992), and from the large ratio of the transport and single particle scattering times it was deduced that the dominant mobility limiting mechanism was remote ionised impurity scattering. Two other groups also used this technique to produce 2DEGs, with similar resulting mobilities; those at AT & T Bell Labs (Mii *et al.*, 1991) and IBM, where the samples yielded the first observation of fractional quantisation of the Hall resistance in the Si/SiGe materials system (Nelson *et al.*, 1992).

Further 2DHG growth studies followed on from the initial work of People *et al.* (1984, 1985), but in contrast with the 2DEG work, increases in the low temperature mobility were modest, with maximum reported values, until recently, not in excess of about 5000 $cm^2V^{-1}s^{-1}$. A list of groups, growth methods and key publications is given below, followed by a summary and discussion of the major conclusions drawn from these works.

A/ Studies on SiGe 2DHGs following those of the Bell group

i/ Mishima *et al.* (1990) at Philips (Eindhoven) have grown structures by **MBE**, using electron-beam evaporation from solid sources (elemental, except for the dopant, which was a heavily B-doped Si slug).

ii/ Nützel *et al.* (1992), at the Technical University of Munich, also used **MBE** in their studies, with B-doping in this case performed using an effusion cell.

iii/ A group at IBM (Yorktown Heights) have grown structures by **UHV-CVD** (Wang *et al.*, 1989a,b).

iv/ Venkataraman *et al.* (1991) at Princeton University have used rapid thermal CVD **(RT-CVD)** with success.

B/ Principal results of transport experiments

One of the central themes in each of the growth investigations was the interface abruptness of the Si/SiGe heterojunctions as well as of the Si:B doping layers. There are no reports of significant Ge surface segregation (see section 4.1), but in MBE grown material B surface accumulation leads to changes in the undoped spacer layer thickness and hence quantum well hole densities (see section 3.1). This phenomenon was observed by Mishima *et al.* (1990). The transport results from this study indicate that the quality of the 'normal' structures (ones with the doped after deposition of the SiGe layer) is superior to that of 'inverted' structures (doping precedes SiGe deposition); this is

illustrated in Fig. 1.3. In CVD grown material, there does not appear to be any great difference in the quality of normal and inverted interfaces. Venkataraman *et al.* (1991) are able to infer from the difference in Shubnikov-de Haas oscillation frequencies for double interface structures that the two spacer layers in material grown by RT-CVD have identical thicknesses (of nominal value 15 nm) to within 1 nm. This apparent absence of B accumulation in the CVD growth method is attributed to saturation of Si surface dangling bonds by H or Cl species.

Determination of the effective masses for hole transport from Shubnikov-de Haas oscillation amplitudes has been carried out by the IBM group on their CVD material (Wang *et al.*, 1989a). The result is a value of $m^*=0.44m_e$ for $Si_{0.85}Ge_{0.15}$ on Si (for $n_s=3\times10^{12}$ cm^{-2}), somewhat higher than $0.32m_e$ for $Si_{0.8}Ge_{0.2}$ on Si, as obtained by People *et al.* (1985) for MBE material. The difference in hole densities (People's sample had a value of $\sim 7\times10^{11}$ cm^{-2}) and also Ge concentration may go some way to explaining

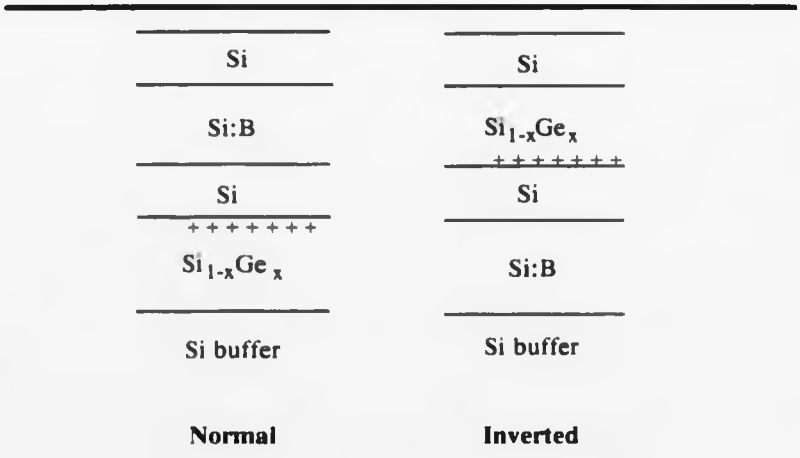

Fig. 1.3 'Normal' and 'inverted' remote doping of quantum wells

this apparent discrepancy, given that the bands are known to be non-parabolic, so that the 'effective' mass changes with wavevector (see section 2.1); however, the precise dependence of m^* on the Fermi wavevector, k_F, has not been determined for $Si/Si_{1-x}Ge_x$ heterostructures. No explanation is given by the IBM group for this discrepancy. It is also pertinent to note that there is no information in their work on the presence, or otherwise, of strain in their epilayers (Wang *et al.*, 1989a,b). Unfortunately, the magnetoresistance in the region $(0 \rightarrow 0.5)$ T is not clear enough, or even shown at all, either in these works or in the magnetotransport paper based on the same material (Fang *et al.*, 1992), so that an analysis in terms of the sign of the low field MR, as followed in chapter 4 of this thesis, is not possible. Negative low field MR in the RT-CVD samples (Venkataraman *et al.*, 1991) indicates that the SiGe layers are strained, following the arguments presented by the author in section 4.3.

A number of attempts have been made to identify likely dominant scattering mechanisms. Nützel *et al.* (1992) observed an increase in mobility with Ge concentration, x, in the alloy up to $x \sim 0.4$, this being attributed to the greater concentration of holes in the quantum well resulting from the larger valence-band offset at the heterojunction and hence more efficient hole-hole screening of scattering potentials. A further point is that m^* should decrease with increasing alloy concentration, as a result of strain-induced band bending (section 2.2). A decrease of mobility is observed for the largest Ge concentration of $x = 0.44$, which is attributed to the critical thickness having been exceeded, with the consequent degradation in structural quality of the material due to the onset of relaxation (section 3.1).

In a direct contradiction of this result, the UHV-CVD experiments showed that the mobility of a $x = 0.15$ composition sample was lower than in an otherwise identical one with $x = 0.12$; but again, no explanation was put forward for this observation. In the same work, a maximum in the mobility, for a constant doping concentration of $\sim 2 \times 10^{18}$ cm^{-3}, occurs at a spacer layer thickness of 6 nm: this implies that remote impurity

scattering is important in these samples, for the following reason. The scattering rate of 2D holes from their ionised parent B-atoms decreases as the spacer layer thickness is increased, due to a reduction in strength of the Coulomb interaction between the two species. However, this is offset by a decrease in the efficiency of screening which the accompanying reduction in carrier density brings about: hence the existence of a mobility maximum. The Munich group suggested that interface roughness scattering was responsible for the lower mobilities observed in narrower quantum wells (Nützel *et al.*, 1992).

Finally, attempts to grow high mobility structures have been made by confining holes in pure Ge channels. This approach has at least two advantages over SiGe channel work: firstly, alloy scattering is eliminated (apart from a small contribution due to leakage into the adjacent potential barriers); and secondly, the effective masses in Ge channels are expected to be somewhat lower than those in SiGe layers. The main technological problem is that to grow such structures on Si substrates, relaxed buffer layers must be used (see earlier). A fifty period, remote doped $Ge/Si_{1-x}Ge_x$ multi quantum well structure has been grown on Si by CVD (Orlov *et al.*, 1990), and the 2D holes have a 4 K mobility of 1.5×10^4 $cm^2V^{-1}s^{-1}$.

1.4 INTRODUCTION TO WORK PRESENTED IN THIS THESIS

This thesis is concerned with the electrical properties of 2DHGs in SiGe channel remote doped heterostructures. It is organised in the following way.

Chapter two contains a description of theoretical aspects of strained $Si/Si_{1-x}Ge_x$ heterostructures, necessary for understanding charge transport processes. The effect of strain and quantum confinement on the bandstructure is discussed first of all, followed by

an examination of the likely scattering processes in terms of their effect on the conductivity. The chapter concludes with a brief review of transport in high magnetic fields.

Chapter three contains a summary of important experimental information; including a discussion of growth phenomena, sample design and fabrication methods and also electrical and cryogenic techniques used.

Experimental results and a full discussion in the context of available theories is presented in **chapter four**. Initial work was concerned with the development of the growth of high mobility 2DHGs and some effort is devoted to explaining the results of the electrical measurements and how the information deduced was used to refine the growth technique. Values of sheet density as a function of structural and doping parameters are compared with those deduced from a model developed by the author. Calculated mobilities for the various mobility limiting mechanisms are compared with the experimental data. Measurements of the resistivity and Hall coefficient in the temperature range (0.3-20) K and in the magnetic fields up to 12 T in strength are then presented. Weak localisation, enhanced hole-hole interaction effects and a temperature dependence of screening all affect the low temperature (< 10 K) conductivity, while magnetoresistance experiments display oscillatory resistance and the quantum Hall effect and provide information about the subband structure.

A summary of conclusions drawn from the work is presented in **chapter five**, along with suggestions for future investigations, both of an experimental and theoretical nature.

CHAPTER TWO

THEORETICAL CONCEPTS

2.1 INTRODUCTION

This chapter houses the basic theory necessary for a discussion of the physical phenomena observed in the course of the experimental work. It may conveniently be divided into a number of sections.

i/ First of all, a description of the band-structure of strained SiGe quantum wells is given (section 2.2), in order to obtain important information such as the number of occupied subbands and their effective masses.

ii/ Once the electrical structure of the material has been determined, it is possible to proceed with an investigation of carrier transport mechanisms (section 2.3). The periodic Bloch potential associated with the atomic basis of the crystal is perturbed by inhomogeneities in the lattice, causing scattering of mobile carriers. Impurities, interface roughness, the random distribution of Ge atoms in the alloy as well as lattice vibrations are all investigated with the aim of determining the transport relaxation time for each scattering mechanism. At very low temperatures ($\leq$10 K) the presence of disorder in a crystal gives rise to weak localisation and enhanced hole-hole interaction effects. Departures from the degenerate limit as well as a temperature dependence of screening give rise to additional temperature dependences of the transport coefficients.

iii/ Finally, transport in strong magnetic fields is discussed (section 2.4). In this

case, providing that the temperature is sufficiently low (liquid helium temperatures are usually adequate), the Landau quantisation is resolved and Shubnikov-de Haas oscillations are observed in the longitudinal resistance (ρ_{xx}) along with quantisation of the Hall resistance (ρ_{xy}) into a series of plateaux.

2.2 SUBBAND STRUCTURE IN $Si_{1-x}Ge_x$ QUANTUM WELLS

2.2.1 BANDSTRUCTURE OF CUBIC SI

The band structure of Si is shown in Fig. 2.1. The valence band maximum lies at the centre of the Brillouin zone, while the 6 conduction band minima are located along the $<100>$ and equivalent directions, about 85% of the way from the zone-centre to the X-points on the boundary (hence cubic Si has an indirect bandgap, as mentioned in chapter one).

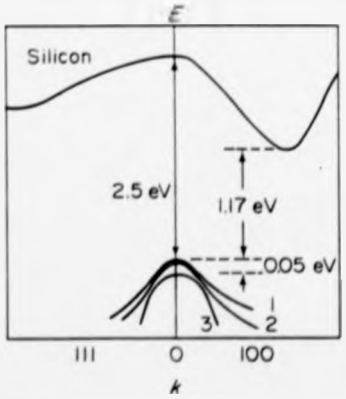

1: heavy hole band
2: light hole band
3: spin-orbit split band

Fig. 2.1 Bandstructure of Si across the forbidden gap (from Bube, 1974)

Due to the 2p character of the outer shell electrons in Si there are actually two valence bands comprising the $\mathbf{k}=0$ maximum. Spin-orbit interaction yields $J=\frac{3}{2}$ and $J=\frac{1}{2}$ levels, which are split by 44 meV at the zone centre, but in addition, the magnetic degeneracy of the $J=\frac{3}{2}$ level is partially lifted away from the zone-centre, giving, in the $|J,M_J\rangle$ representation, $|\frac{3}{2},\pm\frac{3}{2}\rangle$ and $|\frac{3}{2},\pm\frac{1}{2}\rangle$ states. These bands have different shapes, but in addition they are themselves both non-parabolic and anisotropic. This implies that the concept of an effective mass is meaningless unless more rigid identification is provided in the form of a wavevector, such that both the direction of motion and carrier energy are known. Close to the zone centre, for any given wavevector the uppermost band has a smaller curvature than the middle one, so that an effective mass in the upper band will be larger than one in the middle band. This gives rise to a convenient labelling convention, which is followed here.

Quantum state	Name of band	m^* (Si) (zone centre)
$\|\frac{3}{2},\pm\frac{3}{2}\rangle$	heavy-hole	$0.49m_o$
$\|\frac{3}{2},\pm\frac{1}{2}\rangle$	light-hole	$0.16m_o$
$\|\frac{1}{2},\pm\frac{1}{2}\rangle$	spin-orbit	$0.25m_o$

Table 2.1 Energy bands in cubic Si with zone-centre effective masses

In the conduction band, valley minima are ellipsoidal in shape, with their principal axes directed along the <100> and equivalent directions. Consequently, when an electric field is applied along the <100> axis, although current is carried by all six valleys (because they are degenerate in energy), the different relative orientations of the ellipsoids gives rise to one conduction effective mass for the four 'transverse' valleys

($m_l^*=0.19m_o$) and another 'longitudinal' mass for the remaining two valleys ($m_l^*=0.98m_o$) (Sze, 1982). The focus of this study is hole transport and since conduction bands are not intentionally occupied, for instance by optical pumping or the application of a high electric field, then little further study will be devoted to the conduction band.

Typical energy separations of the HH, LH and SO bands in strained material are only tens of meV, so that energy band calculations for these three bands may be carried out ignoring mixing with all other bands, which lie hundreds of meV away. Valence band E-**k** dispersion relationships for strained SiGe quantum well structures have only been calculated for a few specific cases (Ekenberg *et al.*, 1987). However, particular aspects of the problem have been studied in isolation, and it is therefore possible to acquire an understanding of the effects, in turn, of strain and then quantum confinement on the bandstructure, even though calculations must be performed in a fully self-consistent manner in order to obtain accurate data.

2.2.2 EFFECT OF STRAIN ON BAND ENERGIES: DETERMINATION OF THE BAND OFFSET

During sample growth (section 3.1), the $Si_{1-x}Ge_x$ alloy layer is deposited commensurately with a <001> Si substrate, so that there is atomic matching at the hetero-interface. This, however, results in bi-axial compression of the alloy along the interface, because the lattice constant of Ge is 4.2% greater than that of Si, and as a consequence the alloy is tetragonally distorted in the <001> (growth) direction. Using the theory of elasticity it is possible to describe this formally in terms of strain tensors, which then enables a suitable perturbing Hamiltonian to be constructed and shifts in the

energy bands to be calculated.

Calculations of the zone-centre band energies in $Si_{1-x}Ge_x$ lattice-matched to Si <001> were performed in this way by People (1985), and the results for alloy compositions in the range $0 < x < 0.5$ are reproduced in Fig. 2.2. The significant result is that strain lifts the $J = \frac{1}{2}$ zone-centre degeneracy; for $x = 0.2$, the HH-LH separation is about 35 meV.

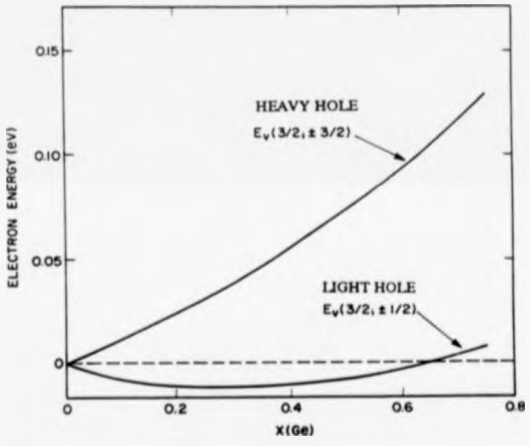

Fig. 2.2 Zone centre band energy shifts for $Si_{1-x}Ge_x$ on Si

Recently, Manku and Nathan (1991) calculated E-**k** dispersion relationships for bulk strained $Si_{0.7}Ge_{0.3}$ alloys and unstrained Si (see Fig. 2.3). The incorporation of strain is seen to cause the following:

i/ the HH band is shifted upwards in energy while the LH band is lowered; and

ii/ the energy bands are deformed, with an increase in radius of curvature and

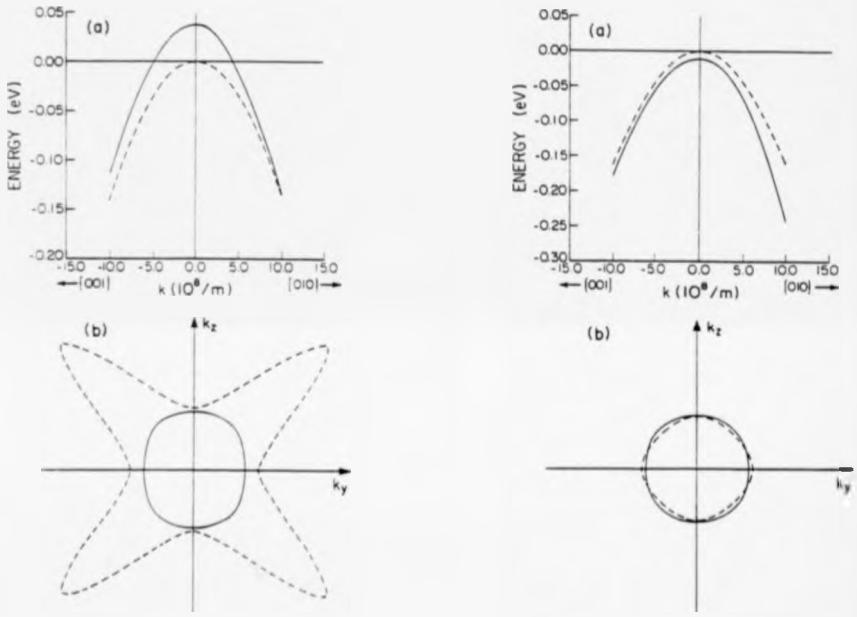

Heavy hole band

Light hole band

Fig. 2.3 Energy-wavevector relationships (with constant energy contours) for bulk, unstrained Si (dashed line) and strained $Si_{0.7}Ge_{0.3}$ matched to Si (001) (solid line) (after Manku and Nathan, 1991)

consequent decrease in effective mass.

This second prediction has been seen in the magnetotransport experiments of People *et al.* (1984), from which a value of $(0.32\pm0.03)m_o$ is deduced for m^* with $n_s = 7\times10^{11}$ cm^{-2} (see section 1.3). This value is significantly different from $0.42m_o$, a linear interpolation between the unstrained elemental Si and Ge values, respectively, of $0.49m_o$ and $0.16m_o$. A further strain-induced change in the band energies results from the dilation of the SiGe unit cell and consequent change in crystal volume. This causes a hydrostatic shift which reduces the bandgap energy.

Together, the uniaxial strain splitting of the band edges and hydrostatic changes to the bandgap energies determine the magnitudes of the two band-offsets at a $Si_{1-x}Ge_x/Si_{1-y}Ge_y$ heterojunction. This concept underpins the bandstructure engineering possibilities discussed in 1.1, so a quantitative knowledge of relevant energies is very important, for use in the design of samples suitable for studying 2D phenomena.

Van de Walle and Martin (1986) have calculated the interface energy shifts using self-consistent pseudopotentials and the local density approximation. Taking known bandgap energies, they proceed to determine the band line-ups at heterointerfaces and magnitudes of the potential steps. The results of these calculations for $Si_{1-x}Ge_x$ lattice-matched to a Si $<001>$ substrate show that nearly all of the bandgap discontinuity is accommodated in the valence band (Fig. 2.4). This was thought to be the case following the modulation doping experiments of People *et al.* (1984), where only 2DHG structures could be manufactured successfully (section 1.3). The value calculated for $\Delta E_v(x=0.2)$ of 170 meV is in fair agreement with the result obtained by People and Bean (1986) using a similar method (150 meV), and is applied with success in Chapter 4 to interpret the experimental data. The size of the band offset corresponds to a thermal energy of

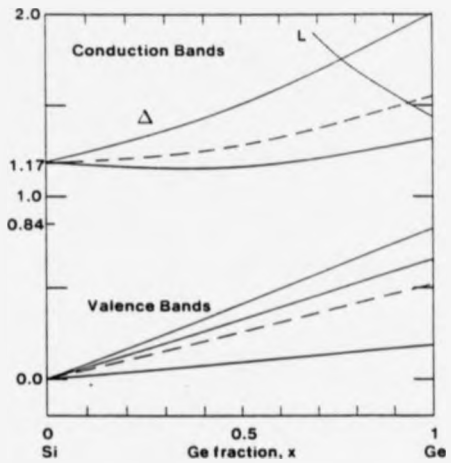

Fig. 2.4 Theoretical band offsets for $Si_{1-x}Ge_x$ matched to Si (001)

roughly 2000 K, and hence this system provides an excellent means of confining holes to two dimensions.

Band offsets have been measured using X-ray photoelectron spectroscopy (XPS) (Ni and Hansson, 1990 and Yu *et al.*, 1990) and temperature-dependent I-V measurements for transport across a heterojunction (Khorran *et al.*, 1991). The comparison of Van de Walle and Martin's theory with the latter results is shown to be extremely favourable, but the disagreement with Ni and Hansson's XPS results is no more than 20%.

2.2.3 REMOTE DOPING AND QUANTUM CONFINEMENT

Quantum confinement produces a ladder of energy eigenstates for each $|J,\pm M_J\rangle$ valence subband. A decrease in the width of the confining potential and a reduction in m^* both cause energy levels to shift away from the bottom of the quantum well. Given that in 3D strained material the HH band has a lower hole energy than the LH band, then quantum confinement will enhance the LH-HH level splitting. The results of **k.p** calculations performed by Ekenberg *et al.* (1987) for 10 nm $Si_{0.5}Ge_{0.5}$ square wells lattice-matched to $Si_{0.75}Ge_{0.25}$ (the nearest strain configuration to that used in the author's work) show that the n=1/n=2 HH energy level separation is about 35 meV [with the LH(n=1)/HH(n=1) levels about 65 meV apart]. In this work, typical hole densities are $\leq 5\times10^{11}$ cm^{-2}, corresponding to a Fermi energy $\leq$4 meV: hence, the possibility of higher (LH) subband occupation may be discounted and transport occurs in the ground (HH) subband only.

Typical sample designs are given in Figs. 4.1 and 4.4. A schematic version of the band line-up across the heterojunction is shown in Fig. 2.5, the physical basis of which may be understood in the following way. The various regions of the heterostructure have particular types and levels of doping, which determine the position of the Fermi level locally, relative to the band edges. In the absence of any externally applied voltage bias, the Fermi level must be uniform across the whole structure: to accommodate this, transfer of charge takes place in two ways.

i/ The existence of a p^{++} region (the Si:B doping spike) adjacent to the n^- substrate means that a depletion region is established across the heterojunction. In between these two layers are nominally un-doped Si and SiGe layers. However, previous analysis of MBE grown material (Houghton, 1991) indicates that a common contaminant

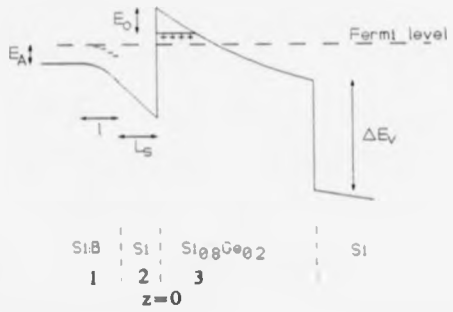

Fig. 2.5 Band alignment across a B-doped Si/SiGe heterojunction

is phosphorus, with concentrations of 10^{14}-10^{15} cm^{-3}; in this case, such a doping level would constitute an extension to the substrate doping profile. The possibility of a significantly lower level of contamination and its effect on the depletion field is addressed in section 2.2.4.

ii/ Some of the holes transferred across the heterojunction are bound at the interface, just inside the SiGe layer, by electrostatic attraction to the ionised parent acceptors in the depleted edge of the doping spike. The accumulation of a sheet of holes at the interface gives rise to the triangular band shape (the potential well), and as the process continues, the bottom of the well is brought nearer to the fixed Fermi level, until the energy difference, (E_F-E_o), corresponds to a number of available states which is equal to the number of holes in the well; at which point, charge transfer is complete.

Fully self-consistent calculations of the bandstructure in doped $Si_{1-x}Ge_x$ single heterojunctions have not been reported in the literature. In the next section, a mathematical description of the subband structure is developed, in order to account for the observed dependence of quantum well hole density on material composition.

2.2.4 QUANTITATIVE DESCRIPTION OF THE QUANTUM WELL SUBBAND STRUCTURE

The electric potential through the heterojunction, $\varphi(x,y,z)$, may be related to the charge density, $\rho(x,y,z)$, using Poisson's equation,

$$\left(\frac{\partial^2}{\partial x^2}+\frac{\partial^2}{\partial y^2}+\frac{\partial^2}{\partial y^2}\right)\varphi(x,y,z)=-\frac{\rho(z)}{\varepsilon_o\varepsilon_r} \quad , \tag{2.2.1}$$

where the z-direction is defined as perpendicular to the 2D gas. Solutions are obtained by ignoring the atomic-scale crystal potential variations, so that (2.2.1) may be reduced to a 1D equation for $\varphi(z)$.

Beginning with the depleted part of the doping spike (region 1 of Fig. 2.5), which has a charge density $\rho(z)=-N_A e$, integration of (2.2.1) yields the potential difference between $z=-(L_s+l)$ and $z=-L_s$ as

$$V_1=\frac{N_A l^2}{2\varepsilon_o\varepsilon_r} \quad . \tag{2.2.2}$$

In region 2 ($-L_s<z<0$), ignoring any background impurity charge (thought to exist at a level $\leq 10^{15}$ cm^{-3}), then $\rho(z)=0$ and the electric field, F_{zz}, is constant. The standard relationship between the electric displacement vectors in two adjacent media,

$$D_{z1}-D_{z2}=\sigma_i \quad , \tag{2.2.3}$$

follows from Maxwell's 2nd Equation, $\nabla.\mathbf{D}=\rho$, where $\mathbf{D}$ is the electric displacement vector, and σ_i is the sheet density of interface charge. Since the average F_x and F_y electric field components are taken to be zero (on the scale of hole wavelengths), then using $\mathbf{D}=\varepsilon\mathbf{F}$, continuity of F_z holds according to

$$\left(F_{z1} - F_{z2}\right)\Big|_{z=-L_s} = \frac{\sigma_i}{\varepsilon_o \varepsilon_r} \quad , \tag{2.2.4}$$

regardless of the presence of any off-diagonal elements in the permittivity $\underline{\varepsilon}$. At $z=-L_s$, $\sigma_i=0$, so that

$$F_{z2} = F_{z1} = \frac{N_A l}{\varepsilon_o \varepsilon_r} \quad , \tag{2.2.5}$$

and the potential difference across region 2 is given by

$$V_2 = F_{z2} L_s = \frac{N_A l}{\varepsilon_o \varepsilon_r} L_s \quad . \tag{2.2.6}$$

Consulting the band diagram (Fig. 2.5), the valence band offset at $z=0$, ΔE_v, may now be expressed in terms of constituent energies as

$$\Delta E_v = E_o + E_F + E_A + e\frac{N_A l^2}{2\varepsilon_o \varepsilon_r} + e\frac{N_A l}{\varepsilon_o \varepsilon_r} L_s \quad , \tag{2.2.7}$$

where E_o is the energy of the lowest bound state in the quantum well and E_A is the B acceptor energy, which for a concentration of 2×10^{18} cm^{-3} is 30 meV (Pearson and Bardeen, 1949).

Starting with $\nabla.\mathbf{D}=\rho$, the electric field inside the quantum well is found to be

$$F_o = \frac{e}{\varepsilon_o \varepsilon_r}\left(n_s + N_{Depl}\right) \quad , \tag{2.2.8}$$

where N_{Depl} is the sheet density of depleted background n-type impurities. In the case of low n-type background doping (10^{14}-10^{15} cm^{-3}), N_{Depl} is given by (Ashcroft and Mermin, 1976)

$$N_{Depl} \equiv \left(\frac{2\varepsilon_o \varepsilon_r N_D E_g}{e^2}\right)^{\frac{1}{2}} \quad , \tag{2.2.9}$$

where N_D is the donor concentration and $N_D << N_A$, so that most of the potential drop occurs in the n-type region [this is roughly equal to the bandgap potential, (E_g/e)]. In

Appendix I, the depletion field is calculated at the Si/SiGe heterojunction for the case of no background doping, with the result

$$F_{Depl} = \frac{eN_D l'}{\varepsilon_o \varepsilon_r} \left\{ \left[1 + \frac{2\varepsilon_o \varepsilon_r E_g}{e^2 N_D l'^2} \right]^{\frac{1}{2}} - 1 \right\} , \qquad (2.2.10)$$

where l' is the total width of the SiGe and Si buffer layer. The depletion field is then estimated to have a value somewhere in between those given by (2.2.9) and (2.2.10).

In the absence of any experimental data, it is assumed that the relative permittivities of Si and $Si_{0.8}Ge_{0.2}$ are the same, which is reasonable given that the elemental values are 11.9 and 16 for Si and Ge respectively (Sze, 1982). Applying the boundary condition (2.2.4) to the electric fields at the Si/SiGe heterojunction gives, on reduction, the expression

$$N_A l = n_s + N_{Depl} , \qquad (2.2.11a)$$

which is a statement of charge neutrality in the structure. In the presence of negatively charged impurities, such as those observed at the heterointerface in C-V profiling studies (see section 4.2.1), (2.2.11a) becomes

$$N_A l + n_i = n_s + N_{Depl} . \qquad (2.2.11b)$$

The confining potential is defined on one side by the vertical band offset and on the other by the potential gradient due to the well and depletion charge. A first approximation of the subband energies may be obtained by taking the case of an infinitely deep triangular well, for which the energy eigenvalues are (Landau and Lifshitz, 1977)

$$E_n = \left(\frac{\hbar^2}{2m^*} \right)^{\frac{1}{3}} \left(\tfrac{3}{2} \pi e F_s \right)^{\frac{2}{3}} \left(n + \tfrac{3}{4} \right)^{\frac{2}{3}} \qquad (n=0,1,2,\ldots) . \qquad (2.2.12)$$

Corresponding eigenfunctions are the Airy functions, but for this work the ground-state

wavefunction used is that introduced by Fang and Howard in their study of electron inversion layers in Si MOSFETs (1966),

$$\chi(z) = \begin{cases} \left(\frac{b^3}{2}\right)^{\frac{1}{2}} z\exp[-\tfrac{1}{2}bz] & (z > 0) \\ 0 & (z < 0) \end{cases} \quad . \qquad (2.2.13)$$

The normalising parameter 'b' is determined using the variational method on the single particle ground state energy,

$$\langle E\rangle = \langle T\rangle + \tfrac{1}{2}\langle V_{h-h}\rangle + \langle V_{h-Depl}\rangle \quad , \qquad (2.2.14)$$

where $\langle T\rangle$ is the mean hole kinetic energy, $\langle V_{h-h}\rangle$ is the mean hole-hole interaction energy [hence the factor of $\frac{1}{2}$ in (2.2.14)] and $\langle V_{h-Depl}\rangle$ is the average energy of interaction for each hole with the depletion charge. In the latter case, the depleted n-type region extends about 1 μm, through the SiGe, Si buffer and into the substrate, while the holes comprising the 2D gas are confined to a region about 5 nm in width at the 'upper' Si/SiGe heterojunction (section 4.2.1). A good approximation to the interaction energy, $\langle V_{h-Depl}\rangle$, is therefore obtained by assuming the interface depletion field, $(e/\varepsilon_o\varepsilon_r)N_{Depl}$, is valid for all z.

Using the wavefunction (2.2.14), expressions for the three energies are (Ando *et al.*, 1982)

$$\langle T\rangle = \frac{\hbar^2 b^2}{8m^*} \quad , \qquad (2.2.15a)$$

$$\langle V_{h-h}\rangle = \frac{33}{16}\left(\frac{e^2 n_s}{\varepsilon_o\varepsilon_r}\right)\frac{1}{b} \quad \text{and} \qquad (2.2.15b)$$

$$\langle V_{h-Depl}\rangle = \frac{3e^2 N_{Depl}}{\varepsilon_o\varepsilon_r b} \quad . \qquad (2.2.15c)$$

Insertion of (2.2.15a-c) into (2.2.14) enables $\langle E\rangle$ to be minimised with respect to b and the result

$$b = \left[\frac{12 m^* e^2}{\hbar^2 \varepsilon_o \varepsilon_r}\left(N_{Depl} + \tfrac{11}{32} n_s\right)\right]^{\frac{1}{3}} \qquad (2.2.16)$$

is obtained.

A realistic treatment of the energy level structure must take account of space charge in the well and its effect on the confining potential. Poisson's equation for the quantum well region ($z > 0$) is

$$\begin{aligned} \frac{d^2\varphi(z)}{dz^2} &= -\frac{e}{\varepsilon_o \varepsilon_r} n_s |\chi(z)|^2 \\ &= -\frac{e}{\varepsilon_o \varepsilon_r} n_s \frac{b^3}{2} z^2 e^{-bz} \end{aligned} \qquad (2.2.17)$$

for which the solution is

$$\varphi(z) = \left\{F_o z - \frac{e n_s}{\varepsilon_o \varepsilon_r}\left(z - \frac{3}{b}\right) - \frac{e n_s}{\varepsilon_o \varepsilon_r}\left(\frac{3}{b} + 2z + \frac{bz^2}{2}\right)\exp[-bz]\right\} \quad (z > 0) \ . \qquad (2.2.18)$$

This well potential is plotted for a range of hole densities in Fig. 2.6 but with the same value of $N_{Depl} = 1 \times 10^{11}$ cm^{-2} in each case. Near the heterojunction, the potential curves reflect the presence of holes in the well in addition to depletion charge (in the limit $bz << 1$, (2.2.18) agrees with (2.2.8), the original expression for the interface electric field), but far from the heterojunction the electric field depends only on depletion charge.

A more accurate value of the ground state energy is now obtained by assuming that (2.2.12) is still valid, but with F_o replaced by F_{eff} (such that $F_{eff} < F_o$), whose value is determined self-consistently in terms of the variable well width parameter 'a' by the set of relations

$$E_o(F_{eff}) = e\varphi(a) = eaF_{eff} \qquad (2.2.19)$$

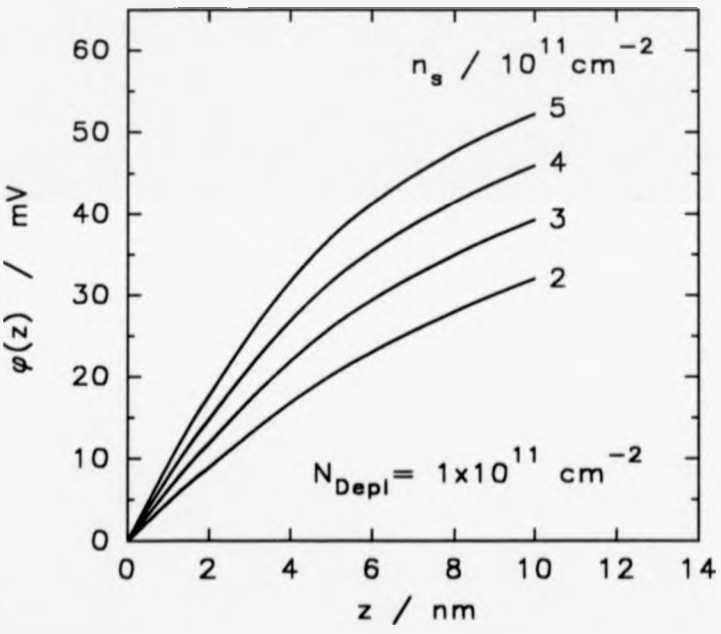

Fig. 2.6 Well potential for different values of confined charge and a constant depletion field.

The value of F_{eff} is now obtained directly, using (2.2.18) for $\varphi(a)$, but with the terms exponential in '-ba' set equal to zero (from the results, ba≥7 - section 4.2.1). Other attempts to account for space charge effects include taking an average ($\frac{1}{2}n_s$) for the hole contribution to the field and adding it to the depletion field (Harris *et al.*, 1989).

Finally, a general relationship between the carrier density and Fermi energy, true for all 2D systems, may be written down as

$$n_s = \int_{-\infty}^{\infty} g(E) f_o(E)\, dE \quad , \tag{2.2.20}$$

where g(E) and $f_o(E)$ are the 2D density of states and Fermi-Dirac state-occupation probability respectively. In a single, isotropic, 2D energy band described by a k^2 dispersion, with a g_s-fold spin degeneracy g(E) is given by

$$g(E) = \frac{g_s m^*}{2\pi\hbar^2} \quad ; \tag{2.2.21}$$

while for all systems of Fermions

$$f_o(E) = \left\{ \exp\left[\frac{E - E_F}{kT} \right] + 1 \right\}^{-1} \quad . \tag{2.2.22}$$

Typical lattice temperatures in the experiments were in the range 0.3-20 K, while the Fermi temperature lies between 20 and 50 K for the carrier densities used. Consequently, it is appropriate to evaluate the integral in (2.2.20) between the limits of 0 and E_F (that is, in the degenerate limit, $T << T_F$), to give (with $g_s = 2$)

$$n_s = \left(\frac{m^*}{\pi\hbar^2} \right) \ln\left[1 + \exp\left(\frac{E_F}{kT} \right) \right] \quad . \tag{2.2.23}$$

In the limit of absolute zero temperature, $f_o(E) = 1$ for $(0 < E < E_F)$, and 0 for all other energies, so that an evaluation of (2.2.20) yields

$$n_s = \frac{m^*}{\pi\hbar^2} E_F = \frac{k_F^2}{2\pi} \quad . \tag{2.2.24}$$

This last result will have to be used in subsequent calculations, despite the shortcomings associated with any uniform effective mass model of this system, as noted in section 2.2.1.

In section 4.2.1, a self-consistent solution to the above series of equations is obtained and the calculated subband structure compared with experimental data for the dependence of sheet density on sample geometry and dopant distribution.

2.3 HOLE TRANSPORT PROCESSES

2.3.1 INTRODUCTION TO THE PRINCIPAL SCATTERING MECHANISMS

Any crystal with a perfect Bloch potential is able to sustain the passage of an electron current without loss of energy to the lattice. In reality, however, a number of factors destroy the periodicity associated with the atomic basis of the crystal, so that it is necessary to apply an electric field in order to maintain a flow of current. In general, two distinct phenomena give rise to electrical resistance: these are imperfections in the lattice and thermal vibration of the atoms. Common examples of lattice imperfections are:

i/ dopant and unintentional impurity atoms;

ii/ a random distribution of alloying atoms (B) in the material $A_{1-x}B_x$; and

iii/ for lower dimensional systems, interface roughness, which causes a lack of abruptness along quantum well boundaries.

Collisions of holes with these types of static lattice imperfections involve no change in the magnitude of momentum, since the scattering centres themselves have no net momentum. Consequently, the hole energies are unchanged in such collisions and the scattering is elastic.

Lattice vibrations are usually discussed in terms of a gas of quasi-particles, phonons, which carry momenta characteristic of the atomic species comprising the unit cells and their mean spatial separations. Collisions of holes with lattice vibrations involve a change in hole momentum due to the absorption or emission of a phonon: as a result, the hole energy is changed and such scattering events are inelastic.

Mathematically, the phonon distribution is represented by the Bose-Einstein

function, $(\exp[\hbar\omega_o/kT]-1)^{-1}$, where $\hbar\omega_o$ is the energy of a particular phonon mode. This expression represents the fact that phonon scattering increases in importance very dramatically with rising temperatures. On the other hand, scattering by lattice imperfections is relatively insensitive to variations in temperature, with much more subtle effects such as those associated with the degeneracy of the system as well as screening, localisation and interaction effects responsible for observed temperature dependences in the transport coefficients. Most of the experimental investigations were performed below 20 K, so that the role of phonon scattering, although important (thermal equilibrium between the 2DHG and crystal lattice is maintained by hole-phonon scattering, thus avoiding 'heating' of the hole gas by the applied electric field), is only minor in the context of trying to determine which of the scattering processes give a significant contribution to the electrical resistance. Phonon scattering in 2DEGs formed in III-V heterostructures has been discussed by Vinter (1984). In very high quality $GaAs/Al_xGa_{1-x}As$ heterojunction samples, the electron-phonon interaction does play a dominant role in transport, even at low temperatures, limiting the carrier mobility to a finite but extremely large value of 8.5×10^6 $cm^2V^{-1}s^{-1}$ at 1.5 K (Foxon *et al.*, 1989). The concern of the rest of this chapter is with elastic scattering processes only.

2.3.2 QUANTITATIVE TREATMENT OF SCATTERING: THE BOLTZMANN EQUATION

The method most frequently used to calculate the scattering rate associated with each type of charge-imperfection interaction is to solve the Boltzmann equation. This describes the departure from equilibrium of the carrier distribution function, $f(\mathbf{k},\mathbf{r},t)$, and, assuming that $\nabla E(\mathbf{k}) = 0$, may be written as (Butcher, 1986)

$$\frac{df}{dt} = -\frac{dr}{dt}.\nabla_r f - \frac{e}{\hbar}\mathbf{F}.\nabla_k f + \left(\frac{\partial f}{\partial t}\right)_{coll} \quad , \tag{2.3.1}$$

which is a statement of particle conservation. The last (collision) term in (2.3.1) describes the interaction of a charge carrier with all entities **other than** the crystal potential and applied fields, such as impurities and phonons.

If (2.3.1) can be written in the form

$$\left(\frac{\partial f}{\partial t}\right)_{coll} = -\frac{f}{\tau} \quad , \tag{2.3.2}$$

which is known as the relaxation time approximation, then in cases of elastic scattering, and with E(**k**) spherically symmetric, the energy dependent relaxation time, $\tau(E)$ is given by (Butcher, 1986)

$$\frac{1}{\tau(E)} = \frac{A}{(2\pi)^2}\int P(\mathbf{k},\mathbf{k}')[1-\cos\theta]d^2\mathbf{k}' \quad , \tag{2.3.3}$$

where A is the area of 2D gas, P(**k**,**k'**) is the probability per unit time of scattering from state **k** to **k'** and θ is the angle between the two wavevectors. Using Fermi's Golden Rule, P(**k**,**k'**) may be written as

$$P(\mathbf{k},\mathbf{k}') = \left(\frac{2\pi}{\hbar}\right)|M(\mathbf{k},\mathbf{k}')|^2\,\delta(E_k - E_{k'}) \quad , \tag{2.3.4}$$

where M(**k**,**k'**) is the matrix element for the transition, with the form of the δ-function ensuring that only elastic scattering processes are permitted.

Section 2.3.4 contains T=0 K results for τ: this is the absolute degenerate limit and the mobility follows as

$$\mu = \frac{e}{m^*}\langle\tau(E)\rangle = \frac{e}{m^*}\tau(E_F) \quad . \tag{2.3.5}$$

Subsequently, expressions for σ may be adapted to incorporate temperature dependences

in the Boltzmann conductivity (section 2.3.5).

2.3.3 SCREENING AND CORRELATION EFFECTS IN 2D SYSTEMS

One of the most important consequences of the existence of disorder within the lattice is that electrons or holes comprising the charge gas are not distributed uniformly in space and instead re-arrange themselves in response to the perturbation, to reach a minimum energy configuration. In this way, the carriers screen one another from the random potential, thus reducing its strength. A mathematical description of screening in 2D gases is provided by Bastard (1988). The dielectric function is often written in the 2D Thomas-Fermi approximation as

$$\varepsilon(\mathbf{q}) = 1 + \frac{q_s}{q} \quad , \tag{2.3.6}$$

where q_s is given by

$$q_s = \left(\frac{e^2}{2\varepsilon_o \varepsilon_r}\right)\frac{\partial n_s}{\partial E_F} = \frac{m^* e^2}{2\pi \varepsilon_o \varepsilon_r \hbar^2} \quad . \tag{2.3.7}$$

Approximations used in the derivation of this expression mean that it is invalid in the limit of vanishing n_s (or $\mathbf{q}$) and therefore the apparent divergence of $\varepsilon(\mathbf{q})$ in (2.3.6) in the limit of vanishing carrier density (at $q=0$) is not of physical significance. In the limit $n_s \rightarrow \infty$, $\varepsilon(\mathbf{q})$ is constant, which reflects the fact that at high carrier densities external potentials are very effectively screened out.

Jonson (1976) has given a more sophisticated treatment of screening by considering directly the effect of charge density fluctuations due to the random potential in the lattice. In this case, a mean-field (Hartree) model is replaced by one in which local-field corrections are taken account of.

2.3.4 SPECIFIC CARRIER SCATTERING MECHANISMS

2.3.4.1 REMOTE IMPURITY SCATTERING

The effectiveness of remote doping may be determined by estimating the strength of the scattering of holes in the quantum well by their ionised parent acceptor atoms, which are located in the depleted edge of the B doped region. In the case of a single heterojunction doped on one side only, taking screening in the 2D Thomas-Fermi approximation, the mobility in the degenerate limit is (Lee *et al.*, 1983)

$$\mu_{RI} = 32\sqrt{2\pi}\,\frac{e}{\hbar}\,\frac{n_s^{\frac{1}{2}}}{N_s}\left[\frac{1}{(L_s+w)^2}-\frac{1}{(L_s+w+l)^2}\right]^{-1}. \qquad (2.3.8)$$

where w is the width of the 2D gas (for the Fang-Howard wavefunction $w=3/b$), L_s is the distance between the edges of the QW and doping spike and l is the thickness of the depleted part of the doping spike (see section 2.2.4). In this work, $l \sim 1$ nm, while $(L_s+w) \geq 15$ nm, so to a good approximation (2.3.8) simplifies to $\mu_{RI} \propto n_s^{3/2}(L_s+w)^3$. The fact that n_s decreases with increasing L_s (section 4.2.1) means that there is some value of L_s at which the value of μ_{RI} has a maximum, as has been observed in experiments (section 1.3).

2.3.4.2 ALLOY SCATTERING

The distribution of Ge atoms in MBE-grown $Si_{1-x}Ge_x$ alloys is, to a good approximation, completely random. This means that in the $x=0.2$ composition material used for the experiments, the Bloch periodicity associated with the Si sub-lattice is severely disrupted at every second or third site. However, a reasonable quantitative

description of the alloy potential may be obtained by using the virtual crystal approximation with a short range potential superposed at each Ge atom site [as developed for III-V quantum wells by Bastard (1983)]. Some controversy exists over the correct energy to use in representing the scattering potential. The inherent problem with taking the difference in band gap energies, ΔE_g, lies with the fact that energy bands derive from macroscopic periodicities in the crystal; and in this case the 'x=0.2' alloy is very far from being dilute. Other possible representations, such as differences in electronegativity or electron affinity, are discussed in the paper by Chattopadhyay *et al.* (1981). In this work, the scattering potential amplitude chosen is $\Delta E_g/e = 0.43$ V, with the assumption made that all the band gap difference is accommodated in the valence band, thereby giving an over-estimate of the scattering rate. There have been a number of reports of long range ordering of Ge atoms in MBE-grown alloys [see, for example, Jesson *et al.* (1992)]. However, the effect of any ordering will be to reduce the strength of the scattering potential and so the calculation which follows may be considered to give a maximum possible scattering rate, and hence an estimate of the minimum likely alloy scattering limited mobility.

In a recent study of 2DEGs in the strained GaAs/$In_xGa_{1-x}As$ system, fluctuations in both the strain field and crystal potential, due to the In atom distribution, are used to account for the magnitude of the electron mobility (Lyo and Fritz, 1992). In this work, anomalously low mobilities were attributed to clustering of In atoms in the alloy. Transmission electron-microscopy (TEM) studies of MBE-grown $Si/Si_{1-x}Ge_x$ superlattices do show a long-range oscillation of the 'Si on SiGe' heterointerface position for $x > 0.3$, which is thought to be due to clustering of Ge atoms, due to their high surface mobility during growth (Powell *et al.*, 1992). Recent studies of the evolution of interface morphology during growth of $Si_{1-x}Ge_x$ on Si, using atomic force microscopy, confirm the existence of long range interface roughness on the scale of 10^2 nm (Pidduck *et al.*, 1992).

The mobility due to alloy scattering in Si/SiGe systems has been calculated by Ogale and Madhukar (1984) using a square well representation of the potential variation at Ge lattice sites. In this work, the approach of Bastard (1983, 1988) is followed, where a δ-function representation of the scattering potential is chosen (this makes the mathematics relatively straightforward). The transition probability $P(\mathbf{k},\mathbf{k}')$ may be written as

$$P(\mathbf{k},\mathbf{k}') = \left(\frac{2\pi}{\hbar}\right)\frac{\Delta E^2}{A n_o} x(1-x)\left[\int |\chi(z)|^4 dz\right] \delta(E_k - E_{k'}) \quad , \tag{2.3.9}$$

where $\Delta E = \Delta E_g$ and n_o is the number density of atoms in the crystal, this being equal to $8/a_o^3$ for a tetrahedral lattice. Using (2.2.3) the scattering rate is then estimated as

$$\frac{1}{\tau} = \frac{1}{2\pi\hbar}\frac{\Delta E^2}{n_o} x(1-x)\left[\int |\chi(z)|^4 dz\right]\iint (1-\cos\theta)\, d^2\mathbf{k}'\, \delta(E_k - E_{k'}) \quad . \tag{2.3.10}$$

Writing $d^2\mathbf{k}' = k' d\theta dk'$ and assuming a parabolic energy-dispersion, $E = \hbar^2k^2/2m^*$, (2.3.10) is then evaluated exactly as

$$\frac{1}{\tau} = \frac{m^* \Delta E^2 x(1-x)}{n_o \hbar^3}\int |\chi(z)|^4 dz \quad . \tag{2.3.11}$$

Taking the Fang-Howard wavefunction (2.2.13), the z-integral in (2.3.11) is equal to $\frac{3}{16}b$, so that the mobility at T=0 K is given by

$$\mu_o = \frac{16 e \hbar^3 n_o}{3(m^*)^2 b x(1-x)\Delta E^2} \quad . \tag{2.3.12}$$

To complete the calculation, screening is incorporated using the Thomas-Fermi approximation for $\varepsilon(\mathbf{q})$ (2.3.6). Following Ando *et al.* (1982), the $\mathbf{k}$-θ part of (2.3.10) becomes

$$\frac{1}{\tau} \propto \int \frac{(1-\cos\theta)\,\delta(E_k - E_{k'})\, d^2\mathbf{k}'}{[\varepsilon(\mathbf{q})]^2} \quad . \tag{2.3.13}$$

Noting that for each elastic scattering event, $\mathbf{k}'=\mathbf{k}+\mathbf{q}$, with $|\mathbf{k}|=|\mathbf{k}'|$ ($=k_F$ in the degenerate limit), then $q = 2k_F \sin\frac{1}{2}\theta$, and the expression (2.3.13) reduces to

$$\frac{1}{\tau} \propto \frac{2m^*}{\hbar^2}\int_0^{\infty} dE_{k'}\, \delta(E_{k'} - E_k) \int_0^{2\pi} \frac{\sin^4 \frac{1}{2}\theta\, d\theta}{(\sin\frac{1}{2}\theta + q_s/2k_F)^2} \quad , \tag{2.3.14}$$

which can be evaluated in the limits of high and low carrier density as

$$\frac{1}{\tau} \propto \frac{2m^*\pi}{\hbar^2} \begin{cases} 1 & [(q_s/2k_F) << 1] \\ 3\left(\dfrac{k_F}{q_s}\right)^2 & [(q_s/2k_F) >> 1] \end{cases} \tag{2.3.15}$$

Taking a linear interpolation between the two corresponding mobilities, the screened alloy scattering limited mobility is

$$\mu_{AL} = \mu_o\left(1 + \frac{q_s^2}{3k_F^2}\right) \quad . \tag{2.3.16}$$

This conforms with the exact results obtained in the limits of low and high carrier density (2.3.15). The unphysical divergence of μ_{AL} in (2.3.16) as $k_F \rightarrow 0$ occurs only because the T.-F. function (2.3.6) is not valid in this limit (see section 2.3.3).

2.3.4.3 INTERFACE ROUGHNESS SCATTERING

Any deviation from an abrupt Si/SiGe heterointerface causes a change in the width of the quantum well, which, in turn, gives rise to variation in the eigenstate energies. If such roughness is located at random sites across the interface, then the perturbation of the energy levels constitutes an effective scattering potential for holes moving along the well. In the limit of very large amplitude roughness, such that the ground state energy variation becomes of the order of the Fermi energy, carriers are strongly localised under degenerate ($T << T_F$) conditions (Airaksinen *et al.*, 1988).

There exist a number of different causes of interface roughness. First of all, the effectively random distribution of Ge atoms in the alloy means that, on an atomic scale, one or two atomic layers across the 'heterojunction' should be considered as a transition region between the SiGe and Si. On the other hand, inappropriate selection of growth temperature and deposition rate can lead to growth by islanding in 3 dimensions rather than with advancing terrace edges, in the preferred two-dimensional manner: the result is a heterojunction whose z co-ordinate may vary in position in the x-y plane with a period of many atomic spacings. Finally, the possibility that Ge atoms form clusters in the alloy due to their large surface energies during growth would give rise to localised distortion of the interface due to a non-uniform distribution of the strain energy associated with the accommodation of 4% larger Ge atoms in the lattice.

In this work, the conventional treatment of interface roughness is used, as described by Ando *et al.* (1982). It is assumed that the asperities have a mean displacement Δ from the position of the interface and are correlated in a Gaussian manner, with a characteristic length Λ: the scattering potential is then written as

$$\left\langle \left|U(\mathbf{q})\right|^2 \right\rangle = \pi(\Delta\Lambda)^2 q_s^2 E_F^2 \left(1+\frac{2N_{Depl}}{n_s}\right)^2 e^{-q^2\Lambda^2/4} \quad . \tag{2.3.17}$$

The scattering rate has been calculated by Gold and Dolgopolov (1986), using a more realistic form of the screening function in which local-field corrections (section 2.2.3), as well as the finite extension of the 2D gas perpendicular to the heterointerface, are accounted for. The relaxation time is given by

$$\frac{1}{\tau} = \frac{1}{2\pi\hbar E_F} \int_0^{2k_F} dq \frac{q^2}{\left(4k_F^2 - q^2\right)^{\frac{1}{2}}} \left(\frac{q}{q_s}\right)^2 \frac{\left\langle \left|U(q)\right|^2 \right\rangle}{\left[F(q)(1-G(q)) + q/q_s\right]^2} \quad , \tag{2.3.18}$$

where F(q) accounts for the thickness of the gas and G(q) is Hubbard's approximation of

the local field correction:

$$F(q)=\left[1+\frac{9}{8}\left(\frac{q}{b}\right)+\frac{3}{8}\left(\frac{q}{b}\right)^2\right]\left(1+\frac{q}{b}\right)^{-3} \quad ; \text{and} \tag{2.3.19}$$

$$G(q)=\frac{q}{2\left(q^2+k_F^2\right)^{\frac{1}{2}}} \quad . \tag{2.3.20}$$

Using the appropriate expressions and substituting for q by using $q = 2k_F \sin\frac{1}{2}\theta$ (elastic scattering), the relaxation time (2.3.18) becomes

$$\frac{1}{\tau}=4(\Lambda\Delta)^2\frac{E_F k_F^4}{\hbar}\left(1+\frac{2N_{Depl}}{n_s}\right)^2 I(\theta) \quad , \tag{2.3.21a}$$

$$\text{with} \quad I(\theta)=\int_0^{\pi}\frac{\sin^4\frac{1}{2}\theta\, e^{-(k_F\Lambda)^2\sin^2\frac{1}{2}\theta}\,d\theta}{\left[F(2k_F\sin\frac{1}{2}\theta)\left(1-G(2k_F\sin\frac{1}{2}\theta)\right)+(2k_F/q_s)\sin\frac{1}{2}\theta\right]^2} \quad . \tag{2.3.21b}$$

If analytical solutions for τ are to be obtained, some approximations must be made in order to render the integral, I(θ), in a tractable form. It is convenient both from physical and mathematical viewpoints to consider the three limits $k_F\Lambda << 1$, ≈ 1 and $>> 1$, as one would expect the scattering rate to depend strongly on the relative sizes of the disturbance (Λ) and the inverse wavevector (k_F^{-1}) representing the motion of holes interacting with it: when the two are similar in magnitude, the scattering rate is a maximum.

1/ Short range scattering ($k_F\Lambda << 1$)

In this limit, the exponential term in (2.3.21) is of the order of 1, while the $\sin^4\frac{1}{2}\theta$ function dictates that the dominant contribution comes from $\theta \sim \pi$. The denominator stays roughly constant by comparison, so using these approximations, τ is found to be

$$\frac{1}{\tau}=\frac{3\pi}{2}(\Delta\Lambda)^2\frac{E_F}{\hbar}k_F^4\left(1+\frac{2N_{Depl}}{n_s}\right)^2\left[F(2k_F)\left[1-G(2k_F)\right]+\frac{2k_F}{q_s}\right]^{-2} \quad . \tag{2.3.22}$$

The mobility varies approximately as k_F^{-6}, reflecting a very strong wavevector dependence for the short range scattering mechanism.

2/ Long range scattering ($k_F\Lambda >> 1$)

One way of simplifying (2.3.21) in this case is to note that the long range interaction favours small angle scattering. Writing $\sin\frac{1}{2}\theta << 1$, then $k_F\Lambda\sin\frac{1}{2}\theta \approx 1$, and so retaining only the explicit θ-dependence of the $\sin^4\theta$ function in (2.3.21), the scattering rate becomes

$$\frac{1}{\tau} = \frac{3\sqrt{\pi}}{\hbar}\left(\frac{E_F}{k_F}\right)\frac{\Delta^2}{\Lambda^3}\left(1+\frac{2N_{Depl}}{n_s}\right)^2\left\{F\left(\frac{2}{\Lambda}\right)\left[1-G\left(\frac{2}{\Lambda}\right)\right]+\frac{2}{q_s\Lambda}\right\}^{-1} \quad . \tag{2.3.23}$$

In contrast to short range scattering, the mobility in this case is relatively insensitive to the magnitude of the hole wavevector.

3/ Maximum scattering rate ($k_F\Lambda\cong 1$)

Using the same approximations as for case 1, a numerical integration of the appropriately simplified form of (2.3.21b) gives

$$\frac{1}{\tau} = 2.1\,\Delta^2\frac{E_F}{\hbar}k_F^2\left(1+\frac{2N_{Depl}}{n_s}\right)^2\left[F(2k_F)\left[1-G(2k_F)\right]+\frac{2k_F}{q_s}\right]^{-2} \quad . \tag{2.3.24}$$

Gold and Dolgopolov (1986) also performed numerical calculations of $\tau(n_s)$, to compare with their analytical results (cases 1 and 2 only). The agreement is sufficiently accurate, with the two methods giving convergent values in the limit $n_s \to 0$, as one would expect from an inspection of the various q-dependent form factors [(2.3.19) and (2.3.20)], while the disagreement is no more than 50% for $n_s = 1\times10^{12}$ cm^{-2}. Consequently the use of analytic formulae is adequate for the diagnostic purpose of this work (the mobilities calculated for the different scattering mechanisms span about 5

decades, while experimental mobilities are all around 2000 $cm^2V^{-1}s^{-1}$ - see section 4.2.1).

2.3.4.4 INTERFACE IMPURITY SCATTERING

Contamination of the heterostructures with impurities is an inevitable consequence of performing growth in a metallic environment (see section 3.1), and this is compounded by high growth temperatures, which enhance the rate of diffusion processes. A discussion of specific impurities and their likely sources is deferred until Chapter 4.

A quantitative treatment of scattering from charged interface impurities has been given by Gold and Dolgopolov (1986) using the same formalism developed by them to describe interface roughness scattering. The scattering potential representing the interaction of a 2D gas with a sheet of impurities of density n_i is

$$\left\langle \left|U(q)\right|^2 \right\rangle = n_i \left(\frac{e^2}{2\pi\varepsilon_o\varepsilon_r} \right)^2 \frac{1}{q^2} \left[F_i(q)\right]^2 \quad , \tag{2.3.25}$$

$$\text{with} \qquad F_i(q) = \left(1 + \frac{q}{b}\right)^{-3} \quad . \tag{2.3.26}$$

Using (2.3.18), the scattering rate is

$$\frac{1}{\tau} = \frac{2n_i E_F}{\hbar n_s} \int_0^{\pi} \frac{\left[F_i\left(2k_F \sin\tfrac{1}{2}\theta\right)\right]^2 \sin^2\tfrac{1}{2}\theta \; d\theta}{\left[F\left(2k_F \sin\tfrac{1}{2}\theta\right)\left[1 - G\left(2k_F \sin\tfrac{1}{2}\theta\right)\right] + \left(2k_F/q_s\right)\sin\tfrac{1}{2}\theta\right]^2} \quad . \tag{2.3.27}$$

As with short range surface roughness scattering the dominant contribution to the integral in (2.3.27) comes from $\theta \sim \pi$, so an approximate solution is obtained by setting $\sin\frac{1}{2}\theta = 1$ in the denominator and in the numerator 'F_i' function, with the result

$$\frac{1}{\tau} = \frac{\pi n_i E_F}{\hbar n_s} \left[\frac{F_i(2k_F)}{\left(F(2k_F)\left[1 - G(2k_F)\right] + 2k_F/q_s\right)} \right]^2 \quad . \tag{2.3.28}$$

2.3.5 TEMPERATURE DEPENDENCE OF THE CONDUCTIVITY

At low temperatures, the density of phonons is relatively small, and so inelastic scattering processes hardly affect the electrical resistance. Changes in the resistivity with temperature are nevertheless observed (see Fig. 4.25, for example) and this behaviour must be attributed to phenomena associated with the various elastic scattering mechanisms. There are at least two results of raising the temperature from 0 K:

i/ the relaxation time averaged over all available energies, $\langle \tau(E) \rangle$, departs from the temperature independent value of $\tau(E_F)$; and

ii/ the efficiency of carrier-carrier screening from scattering potentials changes with the onset of thermally induced disorder.

In the following sections, a brief quantitative description of these two effects is given.

2.3.5.1 ENERGY-DEPENDENT RELAXATION TIME

Relaxation times may be written in the form

$$\langle \tau(E) \rangle = \frac{\int_0^\infty \tau(E) E \left[\frac{\partial f_o}{\partial E} \right] dE}{\int_0^\infty E \left[\frac{\partial f_o}{\partial E} \right] dE} \quad , \tag{2.3.29}$$

where f_0 is the equilibrium Fermi-Dirac distribution function (2.2.22). By substituting $\tau(E) \propto E^\gamma$, (2.3.29) may be evaluated in the limit $T << T_F$, using standard results for Fermi integrals (Blakemore, 1985), and the conductivity determined as

$$\sigma(T) = \frac{n_s e^2}{m^*} \langle \tau(E) \rangle = \sigma(0) \left[1 + \frac{\pi^2}{6} \gamma(\gamma+1) \left(\frac{T}{T_F} \right)^2 \right] \quad . \tag{2.3.30}$$

The temperature exponent, γ, typically has a value of one (see also section 2.3.6), in which case the coefficient of the $(T/T_F)^2$ term is roughly 3. In these samples, T_F=(20-50) K, so for $T<2$ K the change of conductivity from its value at $T=0$ K is only a few percent or less.

2.3.5.2 TEMPERATURE DEPENDENCE OF SCREENING

This has been investigated by Gold and Dolgopolov (1985, 1986) following the initial numerical calculations of Stern (1980) which were stimulated by the experimental observation of a decreasing, linear change in the conductance of a 2DEG in a Si MOSFET with increasing temperature (Cham and Wheeler, 1980). Their result is, with $T<<T_F$,

$$\sigma(T)=\sigma(0)\left[1-C(\alpha)C(n_s)\left(\frac{T}{T_F}\right)-D(\alpha)D(n_s)\left(\frac{T}{T_F}\right)^2-....\right], \qquad (2.3.31)$$

where $C(\alpha)$ and $D(\alpha)$ depend on the particular scattering mechanism. The function $C(n_s)$ is given by

$$C(n_s)=\left\{1+\frac{2(k_F/q_s)}{F(2k_F)\left[1-G(2k_F)\right]}\right\}^{-1}. \qquad (2.3.32)$$

and is plotted in Fig. 2.7 for the range of hole densities appropriate to these experiments. In the case of dominant interface roughness scattering, $C(\alpha=0)=\frac{1}{3}\ln 2$, while for charged impurity scattering $C(\alpha=-1)=2\ln 2$. The prefactor $D(\alpha)D(n_s)$ is about an order of magnitude smaller than $C(\alpha)C(n_s)$, and given also that the condition $T<<T_F$ must hold in order for (2.3.31) to be valid, a good approximation for σ is obtained by keeping only the first ('C') temperature dependent term in (2.3.31). Fig. 2.7 shows that

$C(n_s)$ decreases as the charge density increases: taken with the form of (2.3.31) and (2.3.32), this is consistent with the screening efficiency increasing with hole density such that the decrease of the conductivity due to thermal disorder is not so great.

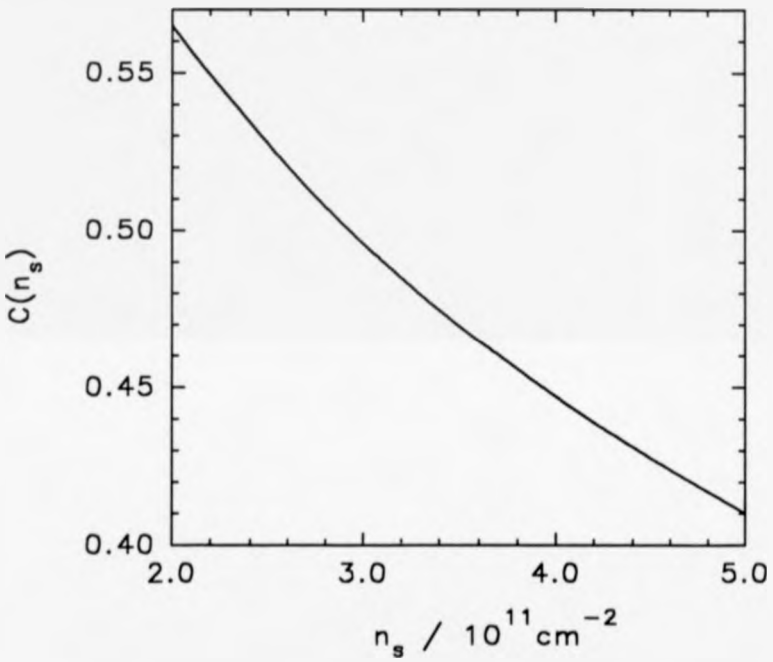

Fig. 2.7 Screening parameter $C(n_s)$ in the Boltzmann conductivity plotted against hole densities, n_s, appropriate to these samples (from Gold and Dolgopolov, 1986)

2.3.6 WEAK LOCALISATION CORRECTIONS TO THE CONDUCTIVITY

2.3.6.1 PHYSICAL BASIS OF WEAK LOCALISATION

Up to this point the presence of disorder in crystals has been considered as a perturbation on conduction by extended states. An alternative approach is now presented. Illustrated in Fig. 2.8 are a few possible paths for charged particles moving under the influence of an electric field between two points, A and B.

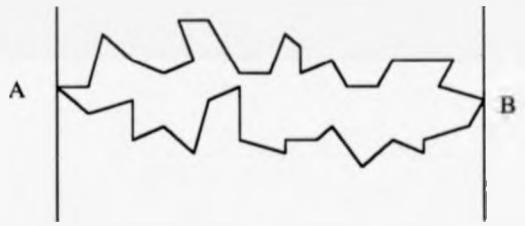

Fig. 2.8 Possible paths from A to B in the presence of disorder

Quantum mechanically, the total charge current, I_{AB}, is obtained by summing the probability amplitudes, a_i, for motion along every possible path, i, and then taking the square of the modulus:

$$I_{AB} = I_o \left| \sum_i a_i \right|^2 = I_o \left[\sum_i |a_i^2| + \sum_{i \neq j} a_i^* a_i \right] . \qquad (2.3.33)$$

Evaluation of the first term inside the square brackets yields the familiar semi-classical Boltzmann conductivity, corresponding to independent motion of charged carriers in an

electric field. The second term, however, represents interference between the partial waves for motion along each path. In general, the phases of the waves arriving at B are uncorrelated since many different routes have been followed, each one with a particular length and journey time. Provided that the sample is large enough, such that there is a large number of possible routes from A to B, the interference term will average to zero.

On the other hand, for systems which are not so large (often termed mesoscopic), such as those with sub-micron dimensions defined using electron-beam lithography, the interference term is finite. Experimentally, the conductivity and other transport coefficients exhibit reproducible (universal) fluctuations which are characteristic of the **particular** device geometry (for a review, see Washburn and Webb, 1992).

A much more general situation occurs, regardless of sample size, when one of the conduction paths contains a closed loop: this is in fact very common for motion in disordered systems, with predominantly short range (isotropic) scattering. In this case, the loop may be traversed in either the clockwise or anti-clockwise directions, with respective probabilities p_1 and p_2. These are equal so long as phase coherence is maintained between the two waves, which is the case provided that all the scattering events are elastic. Firstly, the spatial phase lag, $\sum_{\text{loop}} \mathbf{k}.\mathbf{r}$, is the same for each wave since $|\mathbf{k}|$ is constant under elastic scattering and the paths are identical, with each sequence of scattering events being just the other one time-reversed; and secondly, the time-dependent phase lag, $(E/\hbar)t$, is the same for both waves ($|\mathbf{k}|$ remaining constant implies that $\Delta E = 0$). Using (2.3.33), the probability of finding a carrier at the point of the intersection is $4p_1^2$, exactly double the value expected in the absence of quantum interference. As a result, the carrier is less likely to be found at B: the diffusion constant is reduced by disorder and carriers in such a system are said to be weakly localised.

This phenomenon was first predicted using scaling theory by Abrahams *et al.* (1979). In the case of 2D systems at 0 K, it is argued that no extended states can exist, and a calculation of the conductivity yields the expression

$$\sigma = \sigma_o - A\frac{e^2}{\hbar}\ln\left(\frac{l_\varphi}{l}\right) , \qquad (2.3.34)$$

where l and l_φ are the elastic scattering and de-phasing lengths and A is constant, which was shown subsequently to have a value of $1/\pi^2$ (Lee and Ramakrishnan, 1985).

An alternative method of calculating the weak localisation correction to the conductivity was provided by Bergmann (1983). The two different passages around the loop are represented by the momentum fan diagram (Fig. 2.9) for scattering from state **k** to -**k**: note how the diagram illustrates correctly the relationship between the exchanged momenta, $\mathbf{g}_i$, for two paths with time-reversal symmetry. Bergmann shows that the backscattered intensity is inversely proportional to the number of possible intermediate states for any one elastic scattering event on the loop: the available number of k-states for such a process is equal to the smeared area of Fermi surface ($2\pi k_f \delta k$, where $\delta k \approx l^{-1}$

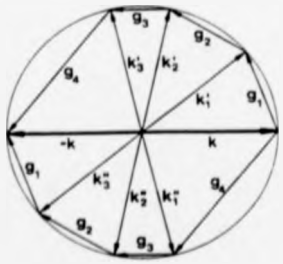

Fig. 2.9 Momentum fan diagram for both paths around a loop, illustrating time-reversal symmetry (from Bergmann, 1983)

from the Uncertainty Principle) multiplied by the density of states in k-space, $1/(2\pi)^2$. Available final states are contained within a k-space area of size L^{-2}, where $L = \sqrt{Dt}$, so that the net backscattered intensity contributing to weak localisation is $l/(2\pi k_F Dt)^{-1}$. The current is proportional to the time-integrated momentum: a forward contribution comes from state k for an elastic scattering time τ, but then the interference term must be subtracted, this being proportional to the total backscattered intensity from time $t=\tau$ to $t=\tau_\varphi$, where τ_φ is a de-phasing time corresponding to the cut-off distance, l_φ, the size of the largest loop with coherent backscattering. The 2D diffusion coefficient is $D = \frac{1}{2} v_F^2 \tau$ and so the weak localisation correction to the conductivity can be evaluated as

$$\Delta\sigma = -\frac{e^2}{2\pi^2\hbar} \ln\left(\frac{\tau_\varphi}{\tau}\right) , \qquad (2.3.35)$$

which agrees with the scaling theory result (2.3.34), on converting from time to length scales.

At T=0 K, l_φ is just the size of the sample. However, finite temperatures, carrier-carrier interactions and also scattering from magnetic impurities all cause abrupt changes in the wavefunction phases, with the result that quantum interference around some loops is destroyed. In the following sections, some pertinent scattering mechanisms are examined along with one other de-phasing perturbation, the application of a magnetic field.

i/ Temperature dependent inelastic scattering

The phase-breaking rate due to inelastic scattering of carriers by lattice vibrations may be written as $\tau_\varphi^{-1} \propto T^p$, from (4.3.1), with p=1 for 2D disordered systems (Al'tshuler and Aronov, 1985). Making the substitution in (2.3.35) for τ_φ yields a temperature dependence of the conductivity,

$$\Delta\sigma(T) = +\left(\frac{e^2}{2\pi^2\hbar}\right) p \ln T \quad . \tag{2.3.36}$$

As the lattice temperature is increased, inelastic scattering becomes ever more frequent (τ_φ is reduced), so that the number of backscattering loops making a quantum interference contribution to σ decreases: consequently the weak localisation is diminished in strength and σ increases, as borne out in (2.3.36).

The first report of a lnT dependence of resistance as a signature of 2D weak localisation was made by Dolan and Osheroff (1979), in measurements of Au:Pd films; and this was followed soon afterwards by observations of similar behaviour in the electron inversion layer of a Si MOSFET (Bishop *et al.*, 1980). Weak localisation phenomena in 2DHGs (formed in Si MOSFETs) have been observed by Gusev *et al.* (1982).

ii/ Magnetic impurity scattering

Scattering from magnetic impurities is also known to cause the quenching of weak localisation, since the spin-flip Hamiltonian destroys time-reversal symmetry. Measurements of the resistance of thin Mg films before and after coverage with $\frac{1}{1000}$ of a monolayer of Fe have been used to study this effect (Bergmann, 1982a).

iii/ Spin-orbit scattering

Spin-orbit scattering does preserve time-reversal symmetry, but because the s.-o. interaction rotates the spins in opposite senses for the two directions in which loops are traversed, the interference can change from being constructive to destructive, depending on the strength of the interaction and density of scattering centres. Bergmann considers a system in which s.-o. scattering is dominant as exhibiting weak anti-localisation (1982b). The extent of this is represented mathematically by multiplying $\Delta\sigma$ in (2.3.35) and

(2.3.36) by a factor α: for spin-$\frac{1}{2}$ states, in the absence of s.-o. scattering $\alpha=1$, whilst for dominant s.-o. scattering $\alpha=-\frac{1}{2}$ (Hikami *et al.*, 1980). Calculations by Al'tshuler *et al.* (1981) show that for $J=\frac{3}{2}$ states, such as holes in the valence bands of undeformed Si or Ge, $\alpha=-\frac{1}{4}$.

2.3.6.2 MAGNETORESISTANCE IN THE 2D AND QUASI-2D WEAK LOCALISATION REGIMES

The application of a magnetic field causes a change in phase of the wavefunctions representing motion around the loops: if S is the area of loop normal to **B**, then the phase change is $\Delta\varphi=\pm(e/\hbar)BS$. Once the phase difference between forward and backscattered waves, $2\Delta\varphi$, exceeds 2π, weak localisation is effectively quenched. Thus for a perpendicular field of strength B, the size of the largest loop able to give a contribution to the quantum interference is

$$L_c \approx \left(\frac{S}{\pi}\right)^{\frac{1}{2}} \approx \left(\frac{\hbar}{eB}\right)^{\frac{1}{2}} \quad ; \qquad (2.3.37)$$

this is also the cyclotron length associated with the semi-classical motion of an electron in a magnetic field.

It can be seen that there is a large number of possible de-phasing mechanisms, and so it is necessary to compare the scattering rates associated with each one when interpreting experimental data. In the case of weak fields ($B << \hbar/4eD\tau$) the magnetoconductance is (Al'tshuler *et al.*, 1980a)

$$\Delta\sigma(B,T) = \sigma(B,T) - \sigma(0,T)$$
$$= \alpha\left(\frac{e^2}{2\pi^2\hbar}\right)\left[\Psi\left(\frac{1}{2}+\frac{\hbar}{4eDB\tau_\varphi}\right) - \Psi\left(\frac{1}{2}+\frac{\hbar}{4eDB\tau}\right) + \ln\left(\frac{\tau_\varphi}{\tau}\right)\right] , \qquad (2.3.38)$$

where Ψ is the digamma function, for which definitions are given by Spanier and Oldham (1989). The analytic limit

$$\Psi(\tfrac{1}{2} + z) \underset{z\to\infty}{=} \ln z + \frac{1}{24\,z^2} \quad . \qquad (2.3.39)$$

may be used to obtain expressions for $\Delta\sigma(B)$ valid for the three characteristic field strengths:

	B-field	Length scale	$\Delta\sigma(B)$
low field	$B << \hbar/4eD\tau_\varphi$	$L_c >> l_\varphi$	$\propto B^2$
medium field	$\hbar/4eD\tau_\varphi << B << \hbar/4eD\tau$	$l << L_c << l_\varphi$	$\propto \ln B$
high field	$B >> \hbar/4eD\tau$	$L_c << l$	constant

In the high-field régime, the fact that the de-phasing length (L_c) is less than the minimum possible backscattering loop size ($\sim l$) means simply that the weak localisation is completely quenched by the magnetic flux. The theory of magnetoresistance in the presence of significant spin-orbit and spin-flip scattering has been developed by Hikami *et al.* (1980) and is reviewed by Bergmann (1984).

The situation with magnetic fields parallel to a 2D gas is somewhat different. For a perfectly 2D system, any magnetic flux in plane with backscattering loops cannot alter the phases of the waves, so one would expect the weak localisation to remain unchanged. However, the quasi-2D nature of most systems, due to a finite thickness, w,

perpendicular to the heterointerface(s) (in this work $w - 5$ nm), means that a parallel field does induce a change in the weak localisation correction to the conductivity, which in the limits $w << l_\varphi, L_c$ is (Al'tshuler and Aronov, 1981)

$$\Delta\sigma(B) = \frac{e^2}{2\pi^2\hbar} \ln\left[1 + \left(\frac{w^2 l_\varphi^2 e^2}{3\hbar^2}\right) B^2\right] . \qquad (2.3.40)$$

If the condition $L_c << w$ is satisfied, the system may be considered 3D, for which the appropriate form of the weak localisation magnetoconductance is (Kawabata, 1982)

$$\Delta\sigma(B)_{3D} = \frac{e^2}{2\pi^2\hbar}\left(\frac{eB}{\hbar}\right)^{\frac{1}{2}} . \qquad (2.3.41)$$

2.3.7 INTERACTION EFFECTS

2.3.7.1 CARRIER-CARRIER INTERACTIONS IN DISORDERED SYSTEMS

The treatment of Coulomb interactions between charged particles exclusively in terms of independent particle motions in an effective field (the Hartree approximation) must be reconsidered when motion is diffusive, due to disorder, rather than simply plane wave-like, as in Bloch potential which is only slightly perturbed. The disorder results in carriers spending greater or lesser amounts of time in particular regions of the crystal so that specific carrier-carrier interaction energies are either enhanced or diminished from some average value. This is considered to produce a reduction in the density of states near the Fermi energy, with the formation of a Coulomb gap, and hence an increase in electrical resistance (Lee and Ramakrishnan, 1985).

Using the methods of diagrammatic perturbation theory, Al'tshuler *et al.* (1980b) provided the first quantitative description of this phenomenon in 2D systems. Four different processes are accounted for; two of which are exchange interactions and two direct (Hartree) interactions, with each one occurring in the so-called diffusion (particle-particle) and Cooper (particle-hole) channels. Exchange processes serve to increase the conductivity, as the interaction between like-spin particles is reduced in strength, while the direct (Hartree) interactions reduce the conductivity, but with a strong dependence on the degree of carrier-carrier screening. The result obtained for the interaction correction to the conductivity of a 2D system is (Al'tshuler *et al.*, 1980b)

$$\Delta\sigma = \frac{e^2}{2\pi^2\hbar}(1-F)\ln\left(\frac{kT\tau}{\hbar}\right) , \qquad (2.3.42)$$

where F is a screened interaction term and is given by

$$F = \int_0^{2\pi} \frac{d\theta}{2\pi}\left[1+\frac{2k_F}{q_s}\sin\tfrac{1}{2}\theta\right]^{-1} . \qquad (2.3.43)$$

Lee and Ramakrishnan (1985) have provided a renormalised calculation of the interaction correction to the conductivity, which necessitates the replacement of (1-F) in (2.3.42) by $(1-\frac{1}{4}F^*)$, but with the renormalised screening parameter, F*, given by

$$F^* = \frac{8}{F}(1+\tfrac{1}{2}F)\ln(1+\tfrac{1}{2}F) - 4 . \qquad (2.3.44)$$

The parameters F and F* are plotted in Fig. 2.10 for a system with $m^*=0.32m_0$ in the range $n_s=(0\text{-}1)\times10^{12}$ cm^{-2}. This is a reasonable approximation for the 2DHGs studied in this work, bearing in mind, however, that m^* does depend on n_s (section 2.2).

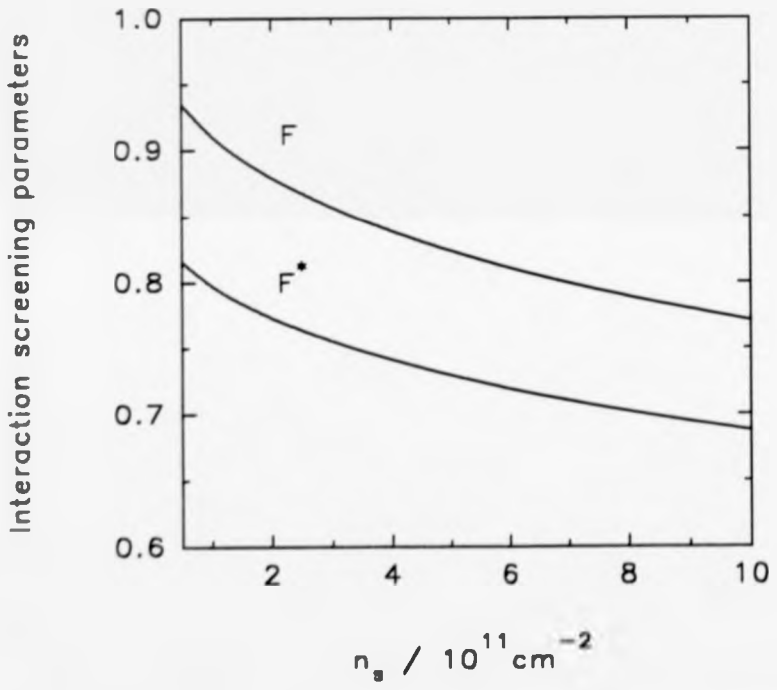

Fig. 2.10 Variation of the screened interaction parameters, F and F*, with n_s

2.3.7.2 MAGNETOCONDUCTANCE DUE TO INTERACTIONS

Magnetoresistance associated with interactions is considered in terms of orbital and spin-splitting (Zeeman) effects. The former are active when the magnetic length, l_c, is less than the inelastic thermal length, L_T (Al'tshuler and Aronov, 1985) [otherwise the interaction conductivity correction is given by (2.3.42)]. Mathematically this is given by

$$\left(\frac{\hbar}{eB}\right)^{\frac{1}{2}} < \left(\frac{\hbar D}{kT}\right)^{\frac{1}{2}} \tag{2.3.45a}$$

which may be rewritten for 2D systems using $D = \frac{1}{2}v_F^2\tau$ as

$$kT < (\mu_B B)(k_F l)\left(\frac{m^*}{m_o}\right)^{-1} . \tag{2.3.45b}$$

Once the condition $g\mu_B B > kT$ is satisfied (g is an effective g-factor incorporating spin), then anti-parallel spin exchange interactions are suppressed and the resistance increases. The corresponding negative magnetoconductance is (Lee and Ramakrishnan, 1985)

$$\Delta\sigma_1 = -\frac{e^2}{2\pi^2\hbar}\frac{F}{2}G(h), \quad \text{with } h = \frac{g\mu_B B}{kT} . \tag{2.3.46}$$

The function G has been evaluated numerically by Burdis and Dean (1988), but it also has the following analytic forms:

$$G(h) = \begin{cases} 0.091h^2 & (h << 1) \\ \ln(h/1.3) & (h >> 1) \end{cases} \tag{2.3.47}$$

2.3.8 HALL EFFECT IN THE PRESENCE OF WEAK LOCALISATION AND INTERACTION EFFECTS

In the experimental work for this thesis, the quantities measured directly were the resistivity tensors, ρ_{xx} and ρ_{xy} (section 3.2.5.2). When current flows only in the x-direction, and in the absence of any magnetic flux, the relationship $\sigma_{xx}=\rho_{xx}^{-1}$ holds, so that a comparison of the experimental results with the theory described is possible. The measurement of ρ_{xy} is usually made to obtain the Hall coefficient ($R_H=\rho_{xy}/B$) for the purpose of estimating the carrier density in the sample. Given the form of the tensor relationship,

$$\rho_{xy}=\sigma_{xy}/\left(\sigma_{xx}^2+\sigma_{xy}^2\right) \quad . \tag{2.3.48}$$

it is important to determine how interaction and localisation effects change σ_{xy} as well as σ_{xx}, in order to understand the behaviour of the Hall coefficient. This problem has been addressed by Al'tshuler *et al.* (1980a) who obtain the following expressions for the Hall conductivity:

$$\frac{\Delta\sigma_{xy}}{\sigma_{xy}}=\begin{cases}\dfrac{2}{\pi k_F l}\ln\left(\dfrac{kT\tau}{\hbar}\right) & \text{(weak localisation)}\\ 0 & \text{(interactions)}\end{cases} \quad . \tag{2.3.49}$$

Using (2.3.48) to obtain an expression for $\Delta\rho_{xy}$ due to small changes $\Delta\sigma_{xx}$ and $\Delta\sigma_{xy}$ on account of localisation or interaction effects, in the limit $B\rightarrow 0$

$$\frac{\Delta\rho_{xy}}{\rho_{xy}}=\begin{cases}0 & \text{(weak localisation)}\\ -2\dfrac{\Delta\sigma_{xx}}{\sigma_{xx}} & \text{(interactions)}\end{cases} \quad . \tag{2.3.50}$$

Thus, from a first order calculation, the Hall coefficient is sensitive only to interactions. The temperature variation of R_H due to inelastic scattering is therefore given by

$$\frac{\Delta R_H}{R_H} = -\frac{2}{\sigma_{xx}}\left(\frac{e^2}{2\pi^2\hbar}\right)\left(1-\tfrac{3}{4}F^*\right)\ln\left(\frac{kT\tau}{\hbar}\right) \quad . \qquad (2.3.51)$$

The implication of this result is that a measurement of the temperature dependence of the Hall coefficient enables the interaction constant, F*, to be determined directly (σ_{xx}, on the other hand, is sensitive to both interaction and localisation effects). The experiments of Uren *et al.* (1980) provided the first verification of the form of (2.3.51), including the existence of the multiplicative factor, 2. The same group of workers also used a perpendicular B-field to quench weak localisation and thus obtain F* directly from the temperature dependence of the magnetoconductance.

2.4 HIGH FIELD MAGNETOTRANSPORT

The application of a magnetic field in the direction normal to the plane of a 2D gas results in further quantisation of the carrier motion. Each of the subbands formed as a result of spatial confinement is split into an infinite series of Landau levels, which have a harmonic oscillator spectrum of the form (Landau and Lifshitz, 1977)

$$E_{LL} = (n + \tfrac{1}{2})\hbar\omega_c \qquad (n=0,1,2,....) \ , \qquad (2.4.1)$$

where $\omega_c = (eB/m^*)$ is the cyclotron frequency. The degeneracy of each level is found by multiplying the density of states, g(E), as given by (2.2.21), with the energy interval, $\hbar\omega_c$, to yield (eB/h), which is just the magnetic flux density divided by the quantum of flux, (h/e).

Disorder causes these levels to be broadened and a band of states is formed: at high enough temperatures the smearing of the Fermi surface means that the Landau quantisation has no effect on transport properties (for the samples studied here, this occurs below ~ 1 T at liquid helium temperatures). Conversely, at high fields and low temperatures, the expected ladder structure is present in the energy spectrum. In this case, each Landau level comprises a region of extended, conducting states in the central region with localised states on each side overlapping with those of adjacent Landau levels.

If the strength of the quantising magnetic field is changed, then both the Landau level spacing and occupancy must also vary. However, the total number of filled states remains constant because the potential well ensures that all charges are confined. Consequently, the Fermi level passes alternately through regions of extended and localised states as the field is swept up or down and the conductivity, σ_{xx}, and resistivity, ρ_{xx}, display strong oscillatory behaviour: this is the Shubnikov-de Haas effect.

Magnetic fields at which ρ_{xx} and σ_{xx} have minima correspond to an integral number of filled Landau levels, since the Fermi level lies exactly in between the extended state

regions: in these cases, the system behaves as an insulator. On the other hand, when the highest occupied Landau level is only half full, then by definition the Fermi level is at the centre of a region of de-localised states, and so the system is metallic. Consequently the conductivity, σ_{xx}, has a maximum and the reason why the resistance, ρ_{xx}, simultaneously has a maximum is that there are many vacant states next to the Fermi level for scattering holes into. The value of the Hall resistance at each resistance minimum may be found by relating the magnetic field which corresponds to an integral number of filled Landau levels to the sheet carrier density by a filling factor, ν, such that

$$n_s = \nu\left(\frac{eB_{min}}{h}\right) \quad . \tag{2.4.2}$$

Using the standard relationship between the Hall resistance and Hall coefficient, $R_H = \rho_{xy}/B$, then with $R_H = 1/ne$ the Hall resistance is just

$$\rho_{xy} = \frac{1}{\nu}\left(\frac{h}{e^2}\right) \quad , \tag{2.4.3}$$

irrespective of sample geometry and doping, depending only on the filling factor, ν. In cases where disorder is weak, such that the band of localised states corresponds to a large fraction of the Landau level spacing energy, $\hbar\omega_c$, then $\rho_{xx} \sim 0$ for relatively large intervals of B. The Hall resistance is therefore given by (2.4.3) for the same range of B field to a good approximation: in other words, the Hall resistance is quantised into a series of plateaux. This is the quantum Hall effect and was first reported by von Klitzing *et al.* (1980) following investigations on Si MOSFET electron channels, in which a constant quantising magnetic field was used, with the well population varied by changing the gate bias voltage.

It is therefore possible, by careful correlation of the MR peaks with the values of adjacent Hall plateau resistances, to assign filling factors to the various resistance minima. The MR peaks may then be labelled in terms of $(\nu + \frac{1}{2})$ filling factors, and the carrier density deduced with the aid of (2.4.2).

CHAPTER THREE

EXPERIMENTAL METHODS

3.1 GROWTH CONSIDERATIONS

The principal material requirements for a study of 2DHGs in SiGe quantum wells are:

i/ single crystal Si and $Si_{1-x}Ge_x$;

ii/ smooth $Si/Si_{1-x}Ge_x$ heterointerfaces, giving good definition to quantum well boundaries;

iii/ an abrupt edge to the doping spike on the side nearest to the quantum well, so that the remote doping mechanism is effective; and

iv/ a minimum impurity contamination of the electrically active region.

The 2DHG samples used in this work were grown by Molecular Beam Epitaxy. This technique is able to satisfy all the requirements listed above, but in doing so places some restrictions on the type of structure which may feasibly be grown. The purpose of this initial 'growth' part of the chapter is two-fold: firstly, to explain the limitations of the growth technique, as an aid to the design of suitable structures for 2DHG investigations; and secondly, to provide the necessary background knowledge of the structural character of the material to aid interpretation of the results of electrical experiments.

3.1.1 Si/SiGe MOLECULAR BEAM EPITAXY

A commercially built Vacuum Generators V90S MBE machine was used by the grower to provide all the structures for this research. A detailed description of Si MBE system design and operation is given by Kubiak *et al.* (1988) and the published proceedings of the 4th International Symposium on Si MBE [MRS Proc. 220 (1991)] contain reports of recent work in the field.

Si and Ge fluxes are established using electron-beam evaporation from elemental sources, while a B flux is generated by passing current through a graphite rod which holds a small lump of elemental B, such that sublimation of B occurs with the rod remaining solid. The substrate holder is fitted with a heater so that ad-atoms on the growing crystal surface may be provided with the appropriate energies for 2D rather than 3D epitaxy, in order to maximise the abruptness of Si/SiGe and Si/Si:B interfaces. All three sources have shutters placed above them so that deposition may be commenced and terminated instantaneously (typical growth rates are ~ 0.1 nms^{-1}) without disturbing the stable operating condition of each cell. Substrates used in the work were 3" or 4" in diameter, cut and polished in the (100) direction. No chemical cleaning of substrates was carried out prior to growth, as this was not found to give improved epi-layer material quality in terms of electrical transport properties. The substrate holder was rotated at 60 r.p.m. during growth to compensate for any spatial inhomogeneity in the beam fluxes, with the aim of giving uniform epi-layer composition across each wafer. At the beginning of every growth series, calibration samples were characterised, using double angle x-ray diffraction to determine $Si_{1-x}Ge_x$ alloy compositions (Powell *et al.*, 1991) and electrochemical capacitance-voltage profiling (ECV) to determine B doping levels (Leong *et al.*, 1985).

3.1.2 BORON DOPING IN Si MBE

There is a tendency for deposited B atoms to accumulate on the surface of growing Si and $Si_{1-x}Ge_x$ crystals, rather than immediately taking up lattice positions. This process is understood to be driven by the local stresses at B-surface bonding sites, due to the large mismatch in atomic radii, and has been studied in both Si and SiGe MBE by Parry *et al.* (1991a,b). Using Secondary Ion Mass Spectrometry (SIMS), an atomic, species-specific, depth profiling technique with nanometre scale resolution, and ECV measurements to determine, respectively, the variation of B atom and hole concentration with depth, it has been shown that surface accumulation of B leads to the formation of shoulders in concentration-depth profiles on the surface side of the doped regions, the shape and size of which are strongly dependent on the growth temperature and growth rate.

The specific mechanism of B incorporation is accounted for quantitatively in terms of equilibrium and kinetically limited accumulation processes which cause, respectively, an increase and decrease of the accumulation length, Δ, on a reduction of growth temperature (Δ is defined as the exponential decay length of the boron concentration on the surface side of the doping spike). The diffusion rates of atoms on the surface may only be considered in terms of an equilibrium model once they exceed the deposition rate of the host matrix material: therefore the maximum in accumulation length, which results from interplay of both accumulation processes, is a function of substrate temperature and growth rate, and for B in Si occurs at T_s=600 °C for a growth rate of 0.1 nms^{-1} (Parry *et al.*, 1991a). The reason for paying close attention to B surface accumulation processes is that the effectiveness of the remote doping process may be altered: inverted structures (ones doped prior to deposition of SiGe) should have larger than expected hole concentrations due to a reduction in spacer thickness, L_s, while the opposite should occur for normal structures, as one expects surface accumulation to lead to an increase in spacer

layer thickness.

3.1.3 STRAINED LAYER EPITAXY

Silicon and germanium both have diamond crystal structures in their unstrained, bulk phases, but the unit cells have different associated lattice constants of 5.43 Å and 5.66 Å respectively (Ashcroft and Mermin, 1976). When a $Si_{1-x}Ge_x$ matrix is deposited on a Si surface, growth is initially pseudo-morphic: in other words, there is atomic matching of the two materials at the hetero-interface so that the in-plane lattice constant of the alloy epi-layer is identical to that of the Si substrate. However, the larger average size of the alloy atoms causes dilation in the direction normal to the interface and strain energy is accommodated as a result of the change in shape of the unit cell.

Hetero-epitaxy continues in this manner until a critical thickness of material has been deposited, at which point the layer begins to relax, with misfit dislocation propagation through it (see Fig. 3.1). This situation is undesirable from an electrical transport perspective, since the dislocations themselves, along with impurity atoms diffusing through the material which may become trapped around these sites, give rise to a random potential environment which will reduce carrier mobilities (section 2.3).

The mechanism for the relief of this metastable equilibrium state of the alloy has been the focus of many studies of the Si/SiGe system. The process has been shown to be kinetically limited, by growing identical epilayers, but at different substrate temperatures, with the observation of a greater density of misfit dislocations in the samples grown at higher temperatures (Timbrell *et al.*, 1990). A value of ~ 1.5 eV was deduced for the activation energy associated with the relaxation of a metastable $Si_{0.82}Ge_{0.18}$ layer grown on Si.

Van der Merwe (1963) used an interface energy balance model in a first attempt

to account quantitatively for critical thickness in the hetero-epitaxy of lattice mismatched materials. Later, a mechanical equilibrium theory was proposed, in which the forces on a hypothetical dislocation introduced to a strained layer are calculated (Matthews and Blakeslee, 1974). Subsequently, experimental work on strained Si/SiGe heterostructures commenced and the measured values of critical thickness were found to be somewhat in excess of those calculated using either of the above theories for a range of SiGe alloy compositions. The reason for this discrepancy was provided by Dodson and Tsao (1987), who performed calculations of critical thickness which embodied kinetic aspects of the relaxation process (dislocation multiplication processes and glide velocities, for example) and good agreement with experiment was now reached (see Fig. 3.1).

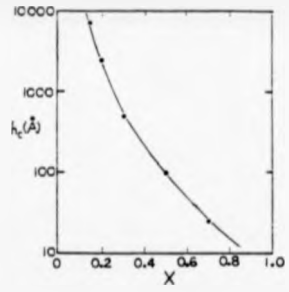

Fig. 3.1 Critical thickness for relaxation of $Si_{1-x}Ge_x$ on Si(001) (after Hull and Bean, 1989)

Possible factors leading to the onset of relaxation have been discussed by Dodson (1988). It is argued that local stress concentrations, such as those due to clusters of impurity atoms, constitute favourable nucleation sites for dislocations. Higgs *et al.* (1991) have demonstrated the effect of adding a thin film of Cu atoms (0.003 monolayers thick) to the surface of a metastable, but dislocation-free, $Si_{0.93}Ge_{0.07}$ layer grown on Si and subsequently annealing the sample at 600 °C. The introduction of surface defects by

Cu contamination promotes the formation of dislocation half-loops below the surface which become the components of misfit dislocation relaxation of the strained SiGe layer. Enhanced rates of strain relaxation observed in ion-implanted $Si/Si_{1-x}Ge_x$ heterostructures have also been attributed to the introduction of point-defect concentrations, a result which has important implications for devices based on this materials system (Hull *et al.*, 1990). By way of contrast, the introduction of large concentrations of oxygen ($\sim 10^{20}$ cm^{-3}) to strained $Si_{1-x}Ge_x$ layers (with $x=0.15$ and 0.21) has been shown to double the critical thickness for relaxation. This is because the smaller oxygen atoms are present in sufficient quantity to compensate partially for the strain induced by the larger Ge atoms (Noble *et al.*, 1991).

One solution to the problem of surface defect formation is to use surfactants such as Sb and As, which saturate dangling bonds on the surface. This method has been applied successfully in the growth of dislocation free Ge layers on Si (100) up to 15 monolayers (ML) in thickness [without a surfactant the critical thickness of Ge on Si is only 6 ML, with 3D growth taking over after deposition of the third ML because of the high surface mobility of the Ge atoms: see LeGoues *et al.* (1989)]. One problem with the use of surfactants is that they do become incorporated in the growing crystal; in the case of Sb at a level of ~ 1 part in 10^5, which is likely to be a problem for device applications (Sakomoto *et al.*, 1992).

One other potential solution to the problem of dislocation formation in these heterostructures is to grow SiGe on mesa islands of Si with micron dimensions, so that the layers are free to expand laterally, as well as in the growth direction. Such an approach has been reported by Powell *et al.* (1991) using MBE to deposit 750 nm thick $Si_{0.85}Ge_{0.15}$ layers (far greater than the metastable critical thickness for this system), with the result that for widths of less than ~ 10 μm the layers relax elastically without the generation of any misfit dislocations.

Hull and Bean (1989) have demonstrated the superior thermal stability of a double interface (buried) SiGe layer compared to one without a surface Si layer. In any case, it is desirable to cap SiGe heterostructures with pure Si which then grows a protective oxide layer in air. Investigations of the oxidation behaviour of SiGe layers in wet O_2 have been carried out by a number of groups (see, for example, Liou *et al.*, 1991, and other published work cited in their article). The conclusion is that, for low Ge concentrations (less than 50%) the role of the Ge atoms is purely as a catalyst (there is a three-fold increase in the oxidation rate of $Si_{0.5}Ge_{0.5}$ compared with Si), such that a Ge-rich layer develops at the SiO_2/SiGe interface. As a result, local areas of stress are induced along this interface, which should lead to an enhanced rate of dislocation formation, following the argument of Dodson (1988). In order to form a more stable passivating layer than that provided by the native oxide, either thermally grown or plasma deposited oxides may be used, with the latter approach being more suited to this materials system because the process takes place at room temperature, thus ensuring that the structural integrity of the partially strained epi-layers is preserved.

3.2 ELECTRICAL EXPERIMENTS

3.2.1 DESIGN OF THE HETEROSTRUCTURES

In order to design suitable structures for the measurement of 2DHG transport properties, it is necessary to balance the restrictions presented by the growth method with those inherent to the intended electrical measurement techniques. The principal objective is to provide low resistance access to the buried 2DHG layer by forming ohmic contacts,

whilst eliminating the effects of parallel conduction paths, preferably directly, or alternatively in the subsequent analysis of data.

Most of the samples have the Si:B doping spike in between the 2DHG and the surface, to ensure that B surface accumulation does not cause contamination of the QW regions. It is therefore impossible to avoid physical contact of the diffused Al regions with the doping region and also the surface oxide, when making electrical connection from the surface to the 2DHG. These experiments are performed mainly at liquid helium temperatures, so that as long as impurity concentrations are well below the Mott 'metal-insulator' critical concentrations, then at 4 K the non-metallic regions should be insulating. The most conductive of these is the Si:B doping spike, for which the Mott critical concentration is $\sim 4\times10^{18}$ cm^{-3} (Dai *et al.*, 1992). In this work, the B doping concentration is $\sim 2\times10^{18}$ cm^{-3}, and so using the data of Morin and Maita (1954) the resistivity of this layer at 4 K is estimated to be $\geq$100 Ωcm. Consequently, for the devices studied, the 50 nm thick doping regions should have resistances in excess of 10^8 Ω, compared with 2DHG channel resistances of $\leq 10^4$ Ω, such that the resultant error in R_{2DHG} ($\leq$0.01%) is negligible. Inspection of Fig. 4.25 shows this assertion to be justified: no activation is observable below T$\sim$20 K, with the steady change in the value of the Hall coefficient below this temperature caused by enhanced hole-hole interaction effects (section 4.3.3), and not a variation of the QW hole population.

The design of samples changed with time but a number of growth features are common to all of them.

i/ an 850 °C Si flux clean was used to desorb the native SiO_2 on the wafer and a Si buffer layer of $\sim$300 nm thickness was then deposited while cooling the substrate to the (usual) heterostructure deposition temperature of 550 °C;

ii/ a growth rate of 0.1 nms^{-1} was used; and

iii/ epi-layers were always capped with Si to provide structural stability (section 3.1.3).

3.2.2 DEVICE FABRICATION

Two types of experiments were performed: firstly, resistance and low field Hall measurements to fulfil basic characterisation needs; and secondly, much more detailed studies of resistance and Hall coefficient made in magnetic fields up to 12 T. In the first case, use of the Van der Pauw measurement technique (1958, 1958/59) is convenient and sufficiently accurate. However, for the high field magnetoresistance (MR) measurements a well defined rectangular geometry is needed, in order to measure the two resistivity tensor components, ρ_{xx} and ρ_{xy}, directly (MR measurements using the Van der Pauw technique require very careful analysis to remove geometrical effects).

A/ Greek cross shaped samples

The first stage in the fabrication process was to deposit 1mm diameter discs of aluminium on the corners of a square with an approximate side length of 7 mm, which was done using a magnetron sputterer (Ion Tech). The samples were then annealed in flowing N_2 gas at 450 °C for 15 minutes, in order to diffuse Al from the surface to the 2DHG in sufficient quantity for ohmic contact formation. Crosses of black wax were painted on by hand, making sure that there were no pinholes and also that the two cross arms were as orthogonal as possible (see section 3.2.5.1). Etching of the wafer for 10 s in CP4A, a mixture of HNO_3, CH_3COOH and HF acids in the ratio 5:3:3, followed by cleaning in xylene to dissolve and remove the wax, left the 2DHG in a mesa cross structure, about 10 μm in height, ready for electrical assessment.

B/ Hall Bar samples

Hall bar mesa structures were fabricated for the author using resists, photolithography and etchants. Processed wafers of size 3 cm × 3 cm, each containing 4 Hall Bar structures, were cleaved by hand and individual devices, about 7 mm × 4 mm in size, were checked to ensure that the contacts were Ohmic and that all equivalent pairs of contacts had similar resistances (see section 3.2.5.2). Suitable samples were then glued with epoxy resin into packages (Epak Electronics) and the package leads connected by gold wire to contact pads on the device using a thermosonic ball wedge bonder (Kulika and Soffa).

3.2.3 CRYOGENIC FACILITIES

3.2.3.1 HIGH TEMPERATURE MEASUREMENTS (5-300 K)

A bath cryostat (Thor Cryogenics), shown in Fig. 3.2, was used for investigations in this temperature range. Cooling was achieved initially with liquid nitrogen and then with liquid ^{4}He to reach temperatures of $\sim$4 K (no pumping facility was available for reducing the boiling point of the ^{4}He below 4.2 K). A $SrTiO_3$ capacitance temperature sensor and a resistance heater, both mounted in the bottom of the sample space, were connected to an a.c. bridge temperature controller (Lake Shore Cryotronics, Model CSC-400) equipped with proportional and integral control (see Forgan, 1991). It was observed that the most stable operating conditions were achieved by using only the minimum cooling power necessary for reaching a given temperature. Suitable adjustment of the pressure of ^{4}He gas in the sample space and exchange gas jacket enabled this requirement to be met. Good temperature stability was achieved with this apparatus (±10 mK at T=4 K), more than complementing the accuracy attained in the sample

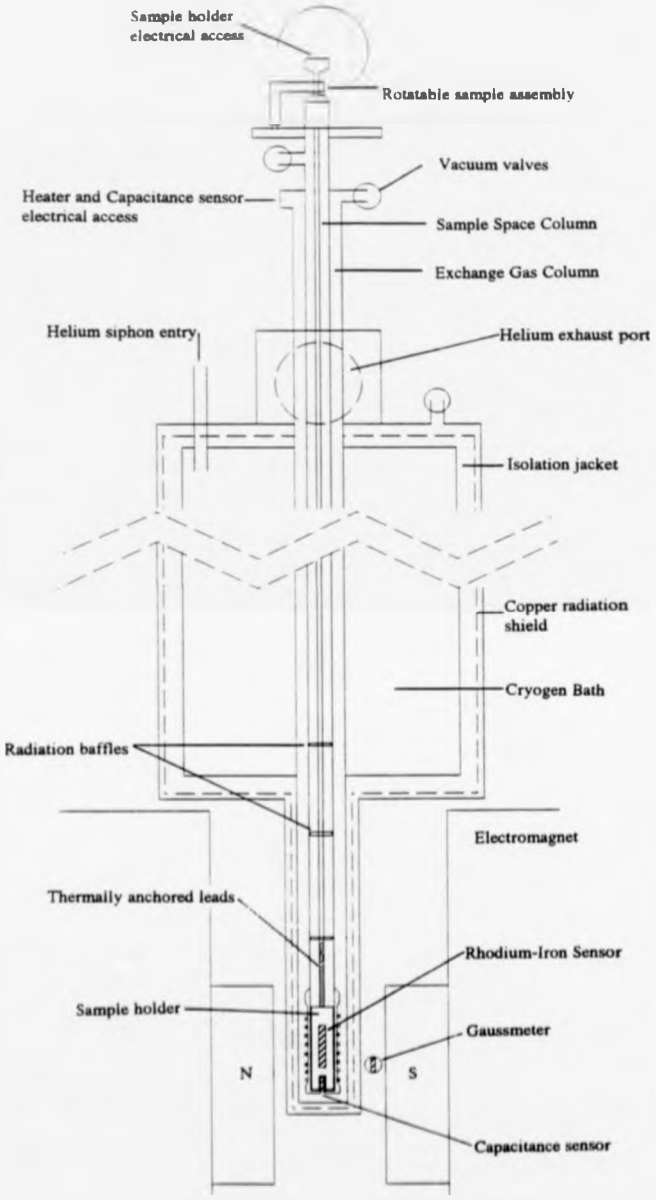

Fig. 3.2 Bath cryostat used for low field measurements above 4 K (after Biswas, 1992)

resistance measurements.

Magnetic fields of ≤0.5 T in strength were provided by a water-cooled electromagnet, its jaws adjusted to accommodate the tail of the cryostat, enabling the sample to be positioned at the centre of the pole piece region (see Fig. 3.2). Magnetic flux densities were measured in-situ using a Hall probe connected to an Oxford Instruments magnetometer. The capacitance sensor was unaffected by the magnetic fields used in the Hall measurements (the tolerance was ≤±0.05% in fields up to 14 T), so that automatic control of the sample temperature was possible throughout these experiments.

3.2.3.2 EXPERIMENTS BELOW 4.2 K AND IN HIGH MAGNETIC FIELDS

An Oxford Instruments Cryomagnetic system fitted with a ^{3}He insert and a 12 T superconducting solenoid was used for these experiments. The central part of the cryostat is shown in cross-section in Fig. 3.3: essentially, the design is governed by the large cost of ^{3}He with the consequent need to keep it isolated and recover all of it in a dump vessel. Prior to any experiment in this system liquid ^{4}He is drawn from the main bath into the 1 K pot, which is then pumped continuously to give a base temperature somewhere in the range 1.3-1.6 K.

In order to reach the lowest possible temperatures (~0.3 K), ^{3}He is condensed inside the sample space and then pumped on using a charcoal sorb (the pumping speed depends on the temperature of the charcoal, which is cooled via a heat exchanger, using ^{4}He from the main bath). The sorb (and hence sample) temperature is controlled automatically by an Oxford Instruments ITC4 Controller which uses the P.I.D. technique (Forgan, 1991), although differential control was not used in the experiments, with a Speer resistor mounted on the sorb as a temperature sensor (this has a tolerance of ≤±0.5% in fields up to a couple of Tesla). When the sorb reaches a temperature

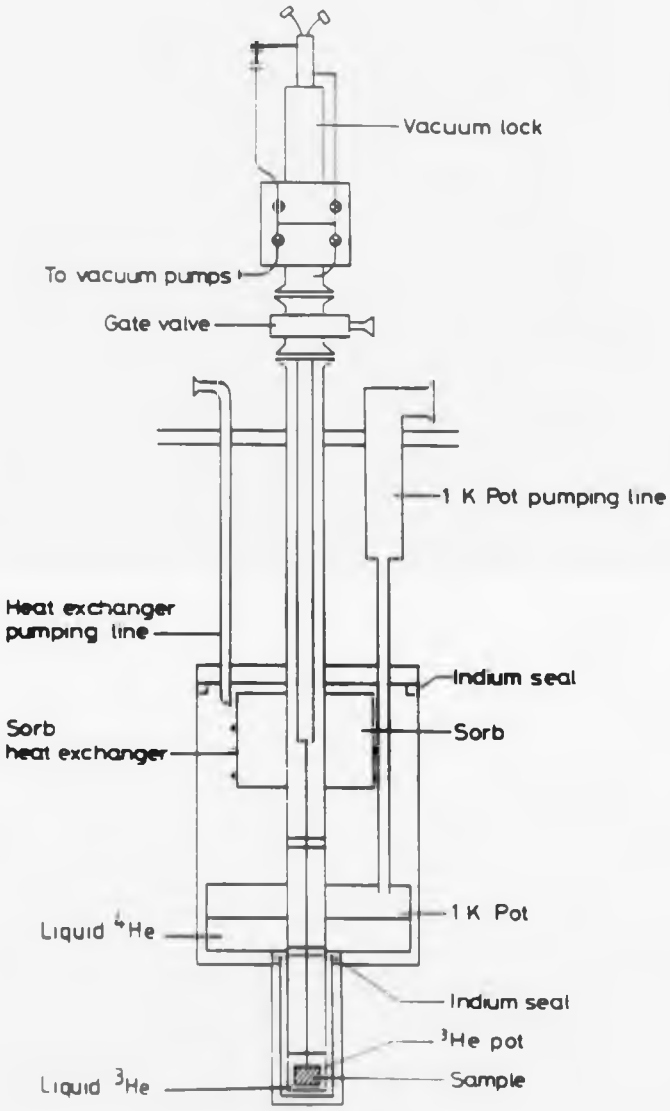

Fig. 3.3 Central region of ^{3}He, 12 T cryomagnetic system (Oxford Instruments)

of ~35 K it ceases to act as a pump and is heated to 50 K to free all the adsorbed ^{3}He atoms. Stable temperatures above 1.5 K are achieved by passing appropriate currents through a resistor mounted on the sample holder to balance the cooling power of the 1K pot, with temperature sensing being performed by a capacitor connected to the 'Lake Shore' controller (section 3.2.3.1).

3.2.4 THERMOMETRY

In every case, current and voltage leads were connected to each thermometer terminal to try and ensure that measured voltages agreed with those in the supplied calibration data, thus avoiding erroneous measured voltage drop along unnecessary extra current carrying lead. A Rh-Fe resistance thermometer was mounted on the sample holder used in the high temperature cryostat. Temperatures were obtained from a reduction of the measured resistance using computer generated fits to the calibration data, such that the quoted accuracy was ±10 mK and ±20 mK respectively, below and above 27 K.

Thermometry requirements in the cryomagnetic system were more stringent, mainly because the rate of hole-phonon scattering, necessary for the maintenance of thermal equilibrium between the 2DHG and crystal lattice, decreases with temperature. The sample holder for this system was made from oxygen-free copper of very high thermal conductivity, which satisfied two main aims:

i/ It acted as a large thermal anchor, to which the sample and thermometry could both be mounted; the aim being, to ensure that the thermometers gave a correct reading of the 2DHG temperature. All these items, along with as much wiring as space allowed, were glued to the sample holder using GE varnish (Oxford Instruments) to ensure good

thermal contact between them, but also to prevent movement of current carrying wire and potential circuit breakage while large magnetic fields were being applied.

ii/ The size of the Cu block, which more or less fills the sample space bore, ensured that thermal gradients in the ^{3}He were kept to a minimum.

A doped Ge resistance thermometer (Lake Shore Cryotronics), calibrated in the range (0.3-6) K to an accuracy of ±0.75 mK, was used in the low temperature work. The only drawback with this type of thermometer is the very large magnetoresistance, such that temperature measurement can only be made in the absence of magnetic flux. This does not present a practical problem for work at low fields, however, because the sensors used in temperature control (a Speer resistor at low temperatures and capacitor at higher temperatures) have negligible MR (see section 3.2.3.2), thus ensuring that the sample temperature remains constant throughout such experiments.

Temperature measurement in high fields was a problem, because it was usually impractical to sweep down to zero field, take a temperature reading and then return to high fields for the next sample measurement, both for reasons of helium economy and efficient use of time (slow changes in field are necessary to avoid excessive eddy current heating around the sample and in the main bath with the magnet). MR measurements in fields up to 12 T were only made at the two available base temperatures; those of the pumped ^{4}He in the 1K pot [(1.3-1.6) K] and pumped ^{3}He (0.3 K). Temperature measurements were taken at the start and finish of field sweeps to check for stability, and during the course of the experiment the apparent temperature reading from the Speer resistor was noted and plotted against magnetic field to check for a continuous rather than erratic variation.

At higher temperatures (>5 K) a diode thermometer, calibrated in the range

(1.5-300) K with an uncertainty of ±30 mK, was used for temperature measurement (Institute of Cryogenics, Southampton University). Changeover from Ge resistance to Si diode thermometers in the (0.3-20) K temperature runs was made around T ~ 5 K with disagreement between the two thermometers never greater than 50 mK.

3.2.5 SAMPLE RESISTANCE AND HALL MEASUREMENTS

3.2.5.1 VAN DER PAUW GEOMETRY SAMPLES

The theory of Van der Pauw (1957, 1958/59) was derived for a lamina of arbitrary shape, with no holes inside its boundary (hence the reason for ensuring that there were no pinholes on the black wax mask), and four infinitesimally small contacts. The Greek cross structure shown in Fig. 3.4 constitutes an excellent approximation to this ideal, with a quantifiable error given by (Versnel, 1979)

$$\frac{R_{meas.}}{R_{VdP}} = 1 + \left\{\frac{2}{\ln 2}\exp\left(-\frac{\pi}{2}\right)\right\}\exp\left[-\frac{\pi}{\lambda}\right] , \qquad (3.2.1)$$

where λ is the ratio of the contact and total boundary lengths. For typical cross shapes used in this work, the value of λ is $\sim\frac{1}{4}$, so that the difference between Van der Pauw and measured resistances is only 2 parts in 10^6, far less than other experimental uncertainties, and may therefore be ignored. The method of resistance measurement is straightforward (see Fig. 3.4). Current flows between two neighbouring contacts while the voltage between the other two is measured in forward and reverse polarity to correct for misalignment of the cross arms. Resistances are then deduced for the four equivalent configurations using the Van der Pauw theory (1958/59), which takes into account defects in the sample geometry, highlighted as different resistance results for each probe configuration, and an average value calculated.

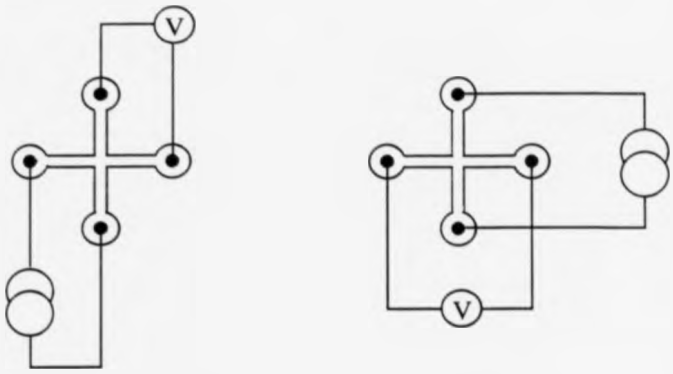

Resistance configuration Hall configuration

Fig. 3.4 Greek cross used in Van der Pauw measurements

Hall measurements are made by passing current between opposite contacts (Fig. 3.4), applying a perpendicular field and then measuring the transverse voltage between the remaining two contacts. All thermo-magnetic voltages, apart from those due to the Nernst-Ettinghausen Effect, were eliminated when calculating the Hall voltage, by taking differences of forward and reverse current, and then field, voltages, as described in Wieder (1979); however, e.m.f.s of thermo-magnetic origin should in any case be absent if samples are sufficiently well thermally anchored to eliminate thermal gradients in the 2DHG.

3.2.5.2 HALL BAR GEOMETRY MEASUREMENTS

Resistance and Hall coefficient measurements using Hall bars were made by applying an a.c. current to the end terminals, 1 and 2, shown in Fig. 3.5. The potential drop between side arms of spacing, *l*, gives a value for resistance, R_{xx}, of (V_{4-3}/I_{1-2}), with

terminal configurations i-j=3-5 and 4-6, which translates into a sheet resistivity, $\rho_{xx} = (w/l)R_{xx}$, where w is the width of the bar. The Hall coefficient is given by $R_H = \rho_{xy}/B$, where $\rho_{xy} = (V_{i-j}/I_{1-2})$, with i-j=3-4 and 5-6 [$V_{i-j}$ is field averaged to eliminate thermo-magnetic e.m.f.s (section 3.5.2.1)].

3.2.6 MEASUREMENT APPARATUS AND OPERATING CONDITIONS

The Van der Pauw measurement circuit was built using a Keithley Instruments 220 constant current source and 181 nanovoltmeter, which were connected to the sample via a 705 scanner with general purpose (7056) and low voltage (7059) cards installed for switching current and voltage lines respectively. The input resistance of the voltmeter is $> 10^9\ \Omega$ and the circuitry gave good accuracy in the measurement of sample resistance up to $\sim 200\ k\Omega$ (this was ascertained by checking the meter readings on different ranges for agreement within 0.1%). In the measurement of higher resistance samples, lines to the voltmeter were buffered using 7650 amplifiers (input resistance of $10^{12}\ \Omega$ and input bias current of 10 pA) wired in the unity-gain configuration. This arrangement facilitated resistance measurement up to the highest encountered values of between 10^6 and $10^7\ \Omega$. The noise level increased to about 1 μV with the high resistance buffers in place, but this did not lead to significant error in the d.c. measurements as typical sample voltages were (1-10) mV.

The Hall Bar measurement circuit is shown in Fig. 3.5. The principal component is a lock-in amplifier (EG & G Instruments, Model 5209) which acts both as an a.c. voltage source and phase sensitive detector. Signal frequencies of ~ 7 Hz were used to avoid picking up any stray mains frequency (50 Hz) related signals. A star earthing procedure to a single electrical ground was followed when setting up the apparatus (both

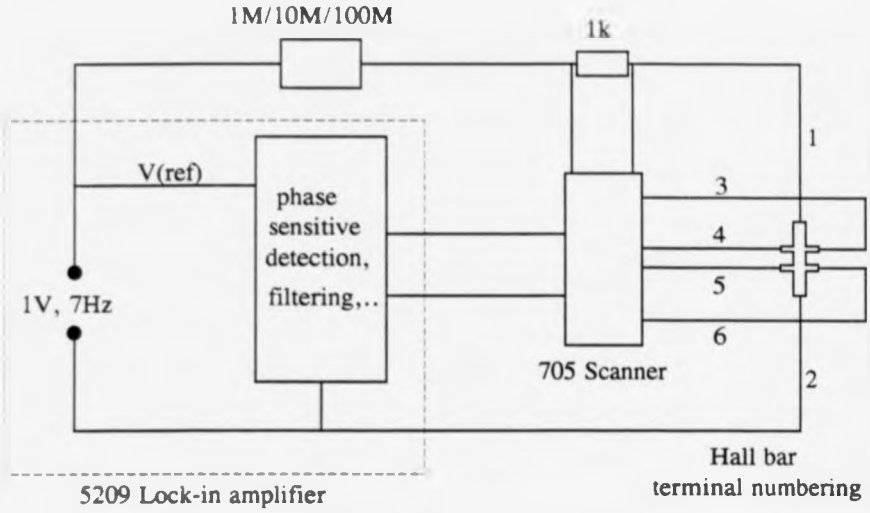

Fig. 3.5 Hall Bar a.c. measurement circuit

the electrical measurement system and cryostat, which is mostly metallic), to try and eliminate additional, unwanted closed loops in the reactive measurement system. The sample current was set by the choice of series resistor (usually 10 MΩ) so that with a 1V output signal from the lock-in amplifier, currents of ~ 100 nA were supplied. The magnitude of the current was determined by measuring the voltage across a precision (±0.1 % tolerance) 1 kΩ resistor in series with the sample.

In all experiments, care was taken to keep electric fields across the samples below ~ 1 Vm^{-1}, to ensure that the 2DHG remained in thermal equilibrium with the surrounding crystal lattice (to which the thermometry was thermally anchored). This is especially important at low temperatures, where a paucity of phonons leads to a low frequency of hole-phonon scattering events, which are necessary for the maintenance of thermal equilibrium between the 2D gas and crystal lattice. Electric field heating of the charge carriers causes a change in their energy dependent relaxation times, and the

corresponding change in resistance should be seen as a departure from linearity in current-voltage relationships. Electrical measurements (samples and thermometry) were controlled by a BBC microcomputer, using a CST Procyon IEEE interface to link up the instruments. Magnetic fields were adjusted by manual control of the power supplies. Specially written software was used for data acquisition in the form of screen, hardcopy and diskette output. The disk files were converted to ASCII format and then imported into a data analysis and graph plotting package (Sigmaplot 5.0, Jandel Scientific) running on an IBM-compatible computer.

CHAPTER FOUR

RESULTS AND DISCUSSION

4.1 GROWTH-RELATED STUDIES

First efforts were devoted entirely to the growth of enhanced mobility 2D hole gas structures, these being a prerequisite for the desired course of the research. In 1990, there was already a considerable amount of relevant published work (section 1.3), but a dearth of growth details meant that initial teething problems did occur. The evolution of the growth technique may be viewed as a three-generation process: in this section, results of resistivity and Hall measurements on samples produced at each stage are presented, along with some explanation for the different types of transport behaviour observed.

4.1.1 INITIAL INVESTIGATIONS: THE PROBLEM OF IMPURITY CONTAMINATION

The first successful growth of high mobility 2DHGs in the Si/SiGe system was reported by People *et al.* from Bell Labs (1984 - see section 1.3). A logical first step on our part, therefore, was an attempt to replicate this structure, including the use of identical growth conditions, so far as possible. Only one change was made to the growth schedule, as follows. The Bell sample is doped on both sides of a 200 nm $Si_{0.8}Ge_{0.2}$ layer, such that two independent quantum wells for holes are formed. It is well known from work on III/V quantum well structures that the morphologies of the so-called normal and inverted interfaces are different (referring, respectively, to the interfaces at

the upper and lower boundaries of the quantum well, as seen in cross-section; for example in Fig. 1.3). In n-type GaAs/$Al_xGa_{1-x}As$ heterostructures, where the GaAs layers act as quantum wells for electrons, the quality of the inverse (GaAs on $Al_xGa_{1-x}As$) interface is inferior to that of the normal interface, which has been attributed to both alloy and dopant effects during growth (Airaksinen *et al.*, 1988).

A second phenomenon, namely B surface accumulation on the crystal surface during growth (section 3.1.2), also leads to a difference between normal and inverted interfaces, with an increase of the undoped spacer layer thickness, L_s, in the normal geometry sample while the opposite effect occurs for the inverted structure. Consequently, for identical doping spike concentrations on each side of the SiGe layer, different densities of holes arise in each well. Given that the carrier-carrier screening efficiency is density dependent (section 2.3.3), then even if the type and unscreened strength of the dominant carrier scattering mechanism is the same for each well the mobilities will differ. Elucidation of the transport parameters in each well is complicated by parallel conduction and requires more detailed experimental investigation than necessary for a single component system. For these reasons, it was decided at the outset to investigate single quantum well structures only.

Two samples were grown: one doped before and one after deposition of the SiGe layer (13/32 and 13/34 respectively), with nominal spacer thicknesses of $L_s = 10$ nm in both cases (see Fig. 4.1). Results of the temperature dependence of resistance, hole density and Hall mobility are presented in Fig. 4.2. In both samples, the non-vanishing carrier density as $T \rightarrow 0$ K indicates that the remote doping is effective, with confirmation of the type of charge carrier coming from the positive Hall voltage. A rapid increase in n_s for $T > 50$ K is caused by the ionisation of B atoms comprising the undepleted part of the doping spike (over 95% of it). Both these observations concur with the those of the Bell group. The possibility that the doping spike concentration

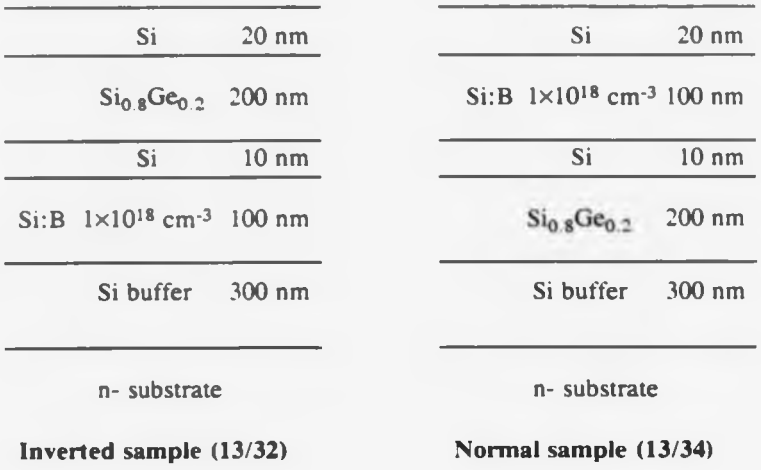

Fig. 4.1 Sample design used in initial 2DHG growth investigations (13/- series)

exceeds the Mott critical concentration for the metal-insulator transition in Si:B (section 3.2.1) may be discounted in view of the fact that the carrier density at 300 K is reduced by about one order of magnitude on cooling to 4K; and, as further proof, the observed mobility is too high for conduction in a Si:B impurity band [for $p=1\times10^{19}$ cm^{-3}, $\mu\sim60$ $cm^2V^{-1}s^{-1}$, for the whole range of temperature, T=(10-200) K (Morin and Maita, 1954)].

The mobility curves exhibit peak values at T=80 K and T=120 K in the normal and inverted structures respectively. At higher temperatures the mobility decreases on account of dominant hole-phonon scattering in the doping spike and, on a smaller scale, in the quantum well itself. The low temperature behaviour is more dramatic, with a rapid decrease in mobility approaching T=0 K.

This low temperature behaviour is quite different from that reported by the Bell

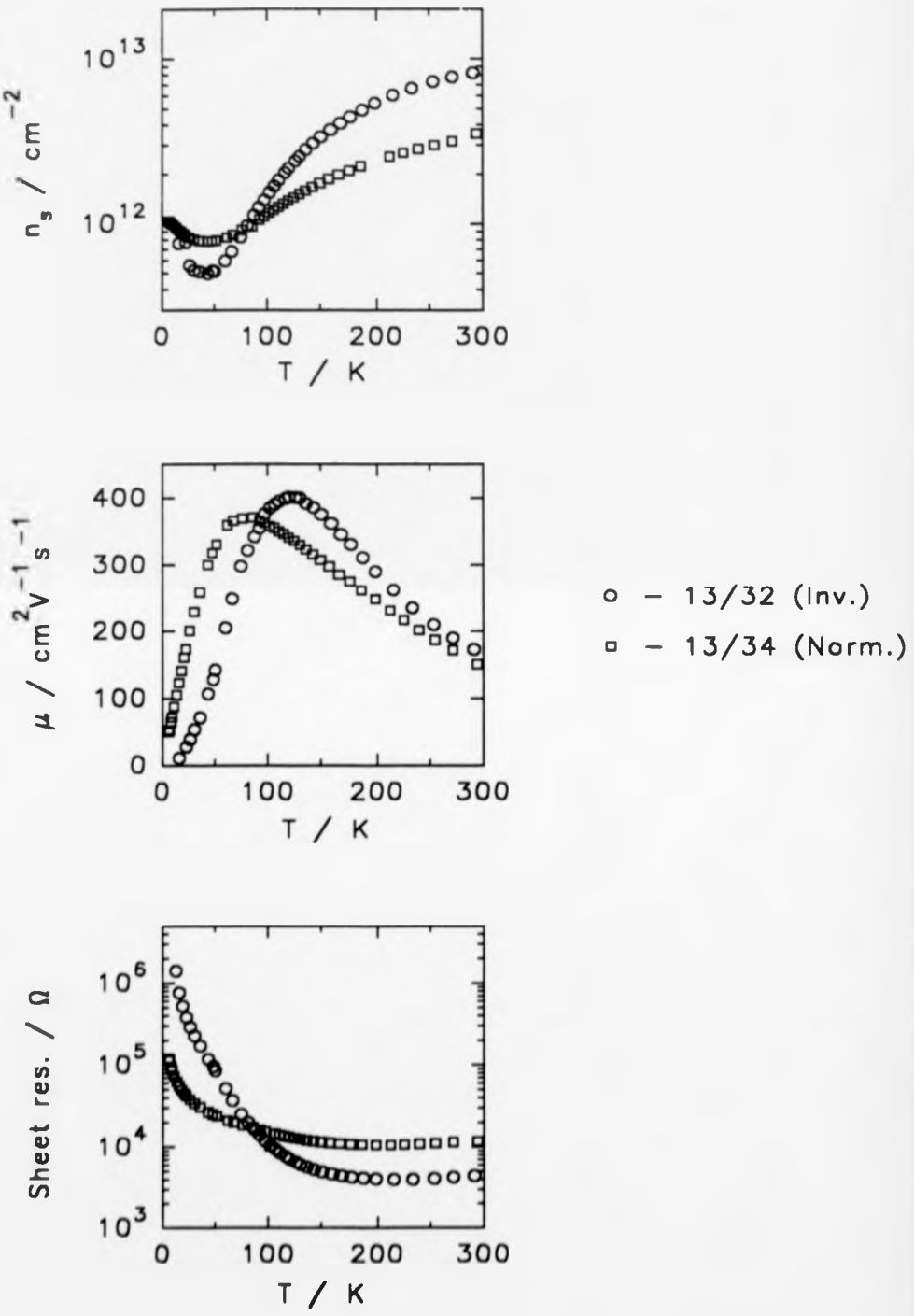

Fig. 4.2 Transport results (n_s, μ and ρ vs. T) for the 13/- series of samples

group (section 1.3). A first appraisal of the results is that either ionised impurity scattering or activated conduction processes are responsible for the nature of the mobility and resistance below 100 K. There are many physical phenomena taking place during growth which could give rise to an interface microstructure capable of promoting one or both of these transport processes: the ones judged most likely to be important are discussed below.

i/ **Boron surface accumulation** might reduce or possibly even eliminate the thickness of Si intended as a spacer layer, giving rise to a stronger ionised impurity scattering rate than expected. However, the form of the mobility is the same in both normal and inverted structures; and furthermore, the expected lower hole density in the normal structure is contrary to the experimental result. The small increase in n_s observed below 50 K is unexpected, but may relate to the nature of the Hall effect in the presence of particular transport mechanisms, rather than to any physical change in the number of holes confined in the well.

ii/ A second possibility is that significant **diffusion of B** from the doping spike takes place, which would lead to a stronger ionised impurity scattering rate in both normal and inverted structures. In uniformly-doped, single-crystal semiconductors, ionised impurity scattering is usually characterised by a sharp drop in mobility with temperature, but with some relief in the fall once neutral impurity scattering becomes active (see Fig. 1.2). It is arguable for this type of structure that, since the potential barrier in the undoped spacer layer inhibits recombination for those ionised acceptors which lie outside the quantum well, particularly at low temperatures, one should observe a temperature dependence of mobility such as that in Fig. 4.2 as being due to ionised impurity scattering. There might also be a neutral impurity scattering contribution to the resistance, but the low temperature Hall measurements imply that a sheet density of at

least 8×10^{11} cm^{-2} ionised B atoms exists outside the well; and if close to the well will cause strong scattering of the confined holes (section 2.3.4.1).

iii/ The undoped spacer layer thickness is also affected by the processes of **Ge solid state diffusion and segregation**. At the maximum growth temperature used (640°C) Ge diffusion is expected to be negligible, but a lack of experimental data for the diffusion coefficient of Ge in Si at these temperatures prevents confirmation of this point. There is little evidence for significant surface segregation of Ge in $Si_{1-x}Ge_x$/Si structures grown by MBE (Smith *et al.*, 1992). Zalm *et al.* (1989) found that segregation of a few $\frac{1}{10}$ths of a monolayer of Ge occurs, but this conclusion has been questioned by Barlow and Dowsett (1992), who have shown that enhanced sputter rates due to pin-hole defects in the SiGe can lead to distortion in Ge depth profiles.

iv/ **Impurity contamination** is likely to be a serious problem in this work on heterostructures, since interfacial regions have some associated disorder and therefore constitute ideal gettering sites for fast diffusing foreign atoms. Consequently, the quantum well located at a Si/SiGe heterojunction ought to become contaminated with more than the average impurity concentration present in the whole sample. Both Coulomb scattering off these sites and interface roughness arising from the lattice distortion due to the accumulation of impurities at the interface (to be discussed next), reduce the average hole mobility.

v/ **Departures from a 2D growth mode** as well as **clustering of Ge atoms** both lead to interface roughness (section 2.3.4.3). If the amplitude of the resulting energy level fluctuations becomes of the order of the Fermi energy, then in the degenerate limit ($T << T_F$) carriers will be strongly localised (Airaksinen *et al.*, 1988 and Gold, 1991). Using X-ray reflectivity, Powell *et al.* (1992) measured the roughness parameter, Δ, for a

five period $Si/Si_{0.79}Ge_{0.21}$ superlattice sample grown just prior to the present samples and found that $\Delta=(0.5\pm0.3)$ nm for both normal and inverted interfaces. The values of the energy eigenstates in a triangular well change with the width, a, as $E \propto a^{-2}$ (section 2.2.4), so that the variation in E_0 may be written as

$$\delta E_0 = 2E_0 \frac{\Delta}{a} \quad . \tag{4.1.1}$$

Using data from the subband structure calculations (section 4.2.1), the energy fluctuations may be calculated for the measured roughness: given the large uncertainty in $\Delta_{r.m.s.}$, calculations are performed for expected and extreme values, with the results collected in Table 4.1. If the roughness has the mean value of 0.5 nm, the energy level

n_s / 10^{11} cm^{-2}	E_0 / meV	E_F / meV	a / nm	δE_0 / meV		
				Δ=0.2 nm	Δ=0.5 nm	Δ=0.8 nm
5.367	42.90	4.03	5.89	2.91	7.29	11.67
4.140	37.39	3.10	6.31	2.37	5.94	9.48
2.997	31.89	2.25	6.83	1.86	4.68	7.47
2.194	27.77	1.64	7.32	1.53	3.81	6.06

Table 4.1 Estimation of the perturbation, δE_0, of the QW ground HH subband due to interface roughness, using (4.1) and well parameters deduced in section 4.2.1.

level fluctuation, δE_0, is always greater than the Fermi energy, by a factor of two or so. In order for these perturbations of the energy level to cause strong localisation of carriers the mean spacing must be less than some critical value for the Anderson transition. Interface charge present will also supplement the roughness induced localisation of holes, while the inclusion of screening will lead to a reduction in the strength of the potential fluctuations. From this basic analysis, it seems plausible that the vanishing mobility approaching T=0 K could be due to strong localisation of holes.

Gold (1985 and 1991) has considered the cases of interface roughness and impurity scattering in a quantum well and gives quantitative confirmation that a mobility edge exists for the reasons outlined above. Experimental evidence for the existence of a disorder-induced metal-insulator (MI) transition comes from Jiang *et al.* (1988) and Tremblay *et al.* (1990), both of whom studied GaAs/AlGaAs heterojunctions with the 2DEG density varied by the application of a surface gate voltage (in the latter case, disorder was ensured by growing a Si δ-layer in close proximity to the quantum well). Similar behaviour has been reported using optical excitation to vary n_s in InP/InGaAs heterostructures by Anderson *et al.* (1986) and also in very high mobility GaAs/AlGaAs heterostructures ($\mu > 10^6$ cm^{2}V^{-1}s^{-1} for $n_s > 10^{11}$ cm^{-2}), where the mobility edge occurs at $n_s \sim 4\times10^9$ cm^{-2} (Sajoto *et al.*, 1990).

Gold (1985) points out that a decrease of mobility with hole density can also be accounted for in terms of a reduction in the efficiency of carrier-carrier screening from scattering potentials, but in that case the decrease is not nearly as rapid as would be expected for a 2D gas approaching the critical concentration for a MI transition. In chapter 2, the idea is introduced that an arbitrarily small amount of disorder is capable of localising all carriers in a 2D system at T=0 K. However, the lnT dependence of the resistance in such cases of weak localisation is different from the exponential variation observed in the present 13/- series samples (see further on).

In the preceding discussion of likely dominant transport mechanisms, the arguments put forward favour very strongly activated transport processes in preference to conduction by extended states with strong impurity scattering (either from B or unintentional metallic species). In general, it was not possible to obtain reproducible transport results from nominally identical samples, which is taken to indicate the presence of some randomly

varying parameter in the growth. The data should be explained on this basis, rather than in terms of the effect of a property such as B accumulation, which for a particular materials system is characteristic of growth conditions such as substrate temperature and flux deposition rate only. It therefore seems important to examine further the case for the existence of strongly localised states, by analysing temperature dependences of the resistance.

When charge carriers are spatially localised a number of different charge transport processes take place. At higher temperatures, carriers are excited to a mobility edge, corresponding to the onset of conduction by extended states, so that the resistance varies as $\exp(T_o/T)$. At lower temperatures, it can be energetically more favourable for carriers to tunnel between localised states. Hopping conduction occurs in the presence of both of these processes; at higher temperatures between nearest neighbour lattice sites, but at lower temperatures with a variable range hopping distance, to minimise the potential energy change between initial and final localised sites (Mott and Davis, 1979). In two dimensions, variable range hopping (VRH) gives rise to an $\exp(T_o/T)^{1/3}$ temperature dependence of the resistance, or, if interactions between charge carriers are strong, such that a Coulomb gap is formed in the density of states, an $\exp(T_o/T)^{1/2}$ dependence (Lee and Ramakrishnan, 1985). Plots of the resistance data on suitable axes to enable identification of the particular conduction process are contained in Fig. 4.3.

Below temperatures of ~ 40 K the resistance exhibits 2D VRH behaviour, as opposed to purely activated transport, but it is not clear from the $T^{1/3}$ and $T^{1/2}$ plots whether or not a Coulomb gap model is appropriate. In both cases, the parameter T_o is much greater for the inverted interface sample, which is due to the existence of more strongly localised states in that case. The higher transition temperature to phonon dominated scattering in the inverted sample is consistent with stronger hole localisation in that case. At higher temperatures, the 2DHG behaviour is masked by transport in the

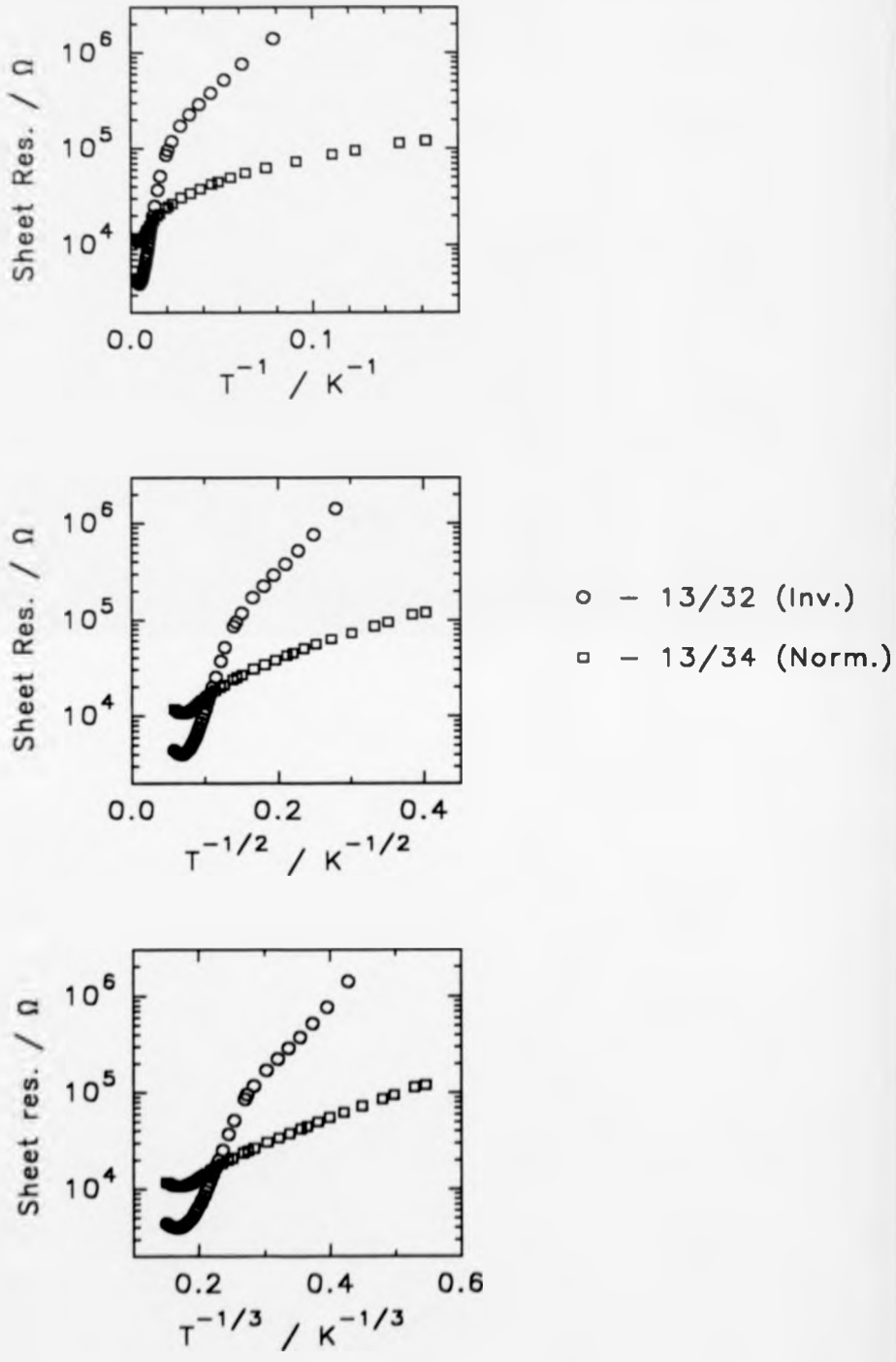

Fig. 4.3 Plots of ρ vs. T, for investigation of the type of hopping or purely activated transport present in the 13/- series of samples

electrically parallel doping spike, as B acceptors become activated, which unfortunately prevents any observation of the onset of purely activated conduction.

4.1.2 ADDITION OF GROWTH INTERRUPTS

In the second series of samples, growth interrupts of a few minutes duration were introduced; the idea being to form disordered layers by leaving the crystal surface exposed only to residual gases in the growth chamber. In this way, potential gettering sites should be formed and thus, with judicious positioning in the epilayer, it might be possible to reduce impurity contamination of the quantum well region.

Details of the samples' structure and growth are provided in Fig. 4.4. In summary, samples 14/22 and 14/26 are identical apart from an additional interrupt 0.5 nm after deposition of the SiGe layer in 14/22, while sample 14/8 is grown without any interrupts at all and has a slightly larger spacer layer thickness. The transport results are presented in Fig. 4.5.

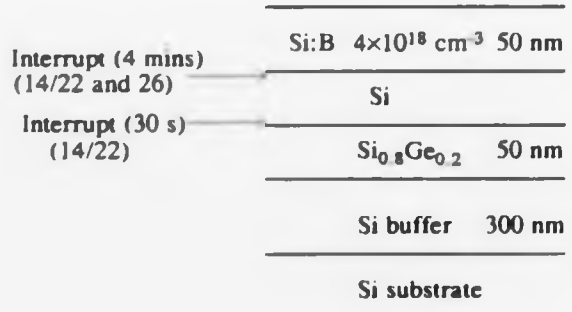

Fig. 4.4 Sample designs for second (14/-) series of growths

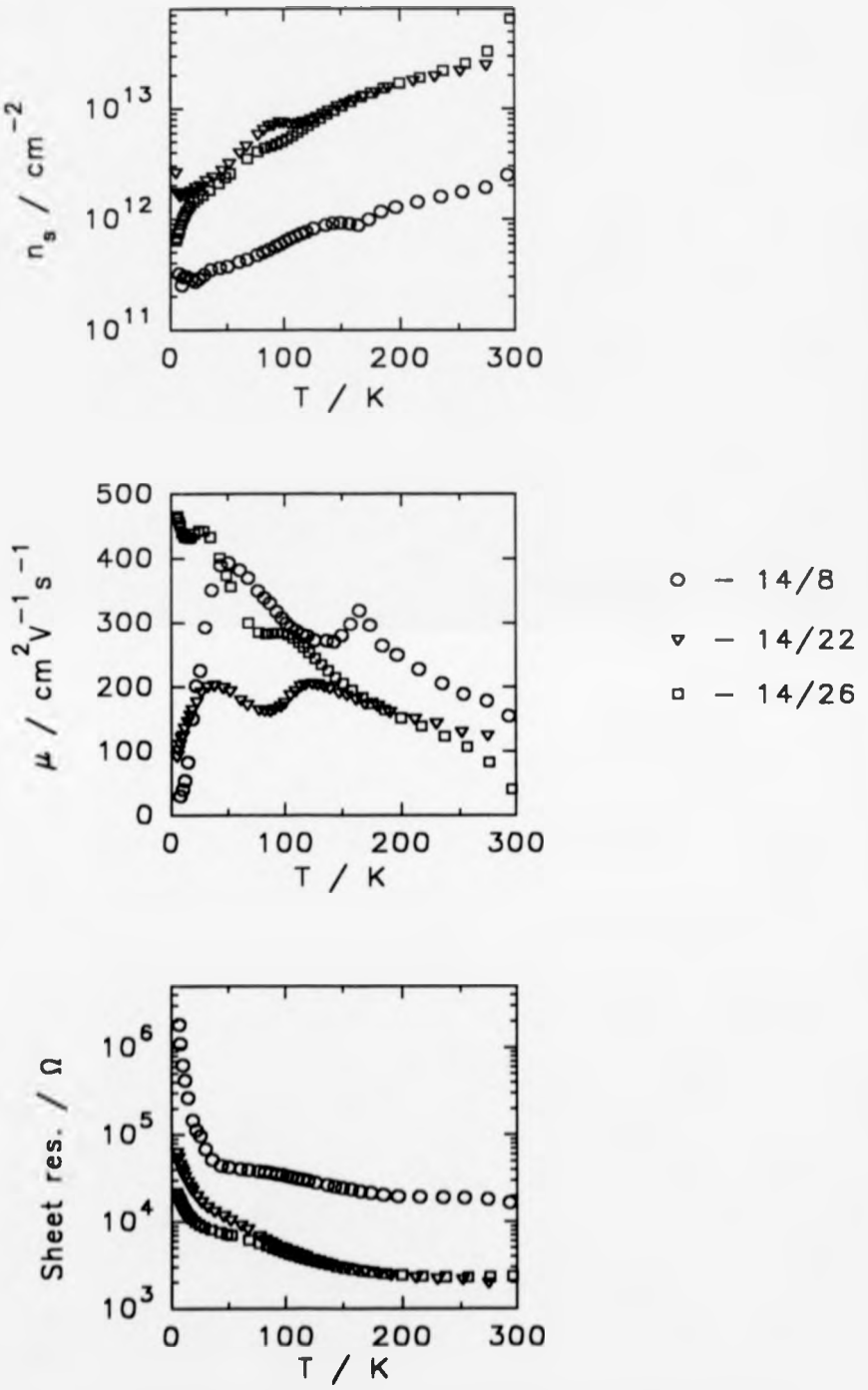

Fig. 4.5 Transport results (n_s, μ and ρ vs. T) for the 14/- series of samples

As expected, the hole densities of samples 14/22 and 14/26 are nearly identical over the whole range of temperature studied. Both 14/8 and 14/22 exhibit the small upturn in n_s at low temperatures seen in the first generation of samples; but in 14/26, there is a continual decrease as T→0 K. This is observed in all samples grown subsequently, and in section 4.3.3.3, the effect is attributed to enhanced hole-hole interactions due to 'weak' disorder, which gives rise to a logarithmic temperature correction in ρ_{xy} (and hence R_H).

Differing behaviour is also seen in the μ-T relationships. Both the sample without any growth interrupts (14/8) and the one with two interrupts, including one only 0.5 nm from the quantum well (14/22), are characterised by a vanishing mobility as T→0 K, as seen in the previous (13/-) series of samples. On the other hand, the sample with a single growth interrupt, sited 8 nm from the edge of the 2DHG (14/26), has a mobility at T=4 K of 450 $cm^2V^{-1}s^{-1}$, with no indication that this will become vanishingly small as T→0 K.

Such a dramatic change in the conduction properties of the hole gas, as induced by an apparently minor alteration to the growth schedule, is consistent with the delocalisation of hole states, through a decrease in roughness and random distribution of charged impurities below some critical value. The argument for the dominance of ionised impurity scattering from B acceptors is now very weak. All three samples should have the same B doping profile, given that the only differences in growth procedure occur before the initiation of B doping. In any case, the two different types of transport behaviour cannot be understood in terms of scattering from ionised B acceptor atoms alone: if, for example, with all other doping and structural parameters kept constant, the ionised B impurity scattering rate were halved, one would expect only a scaling down in magnitude of its effect on the mobility, not a complete change of character, as seen here.

The $\ln\rho - T^{-1/3}$ and $T^{-1/2}$ plots of the resistance data (Fig. 4.6) show some possible

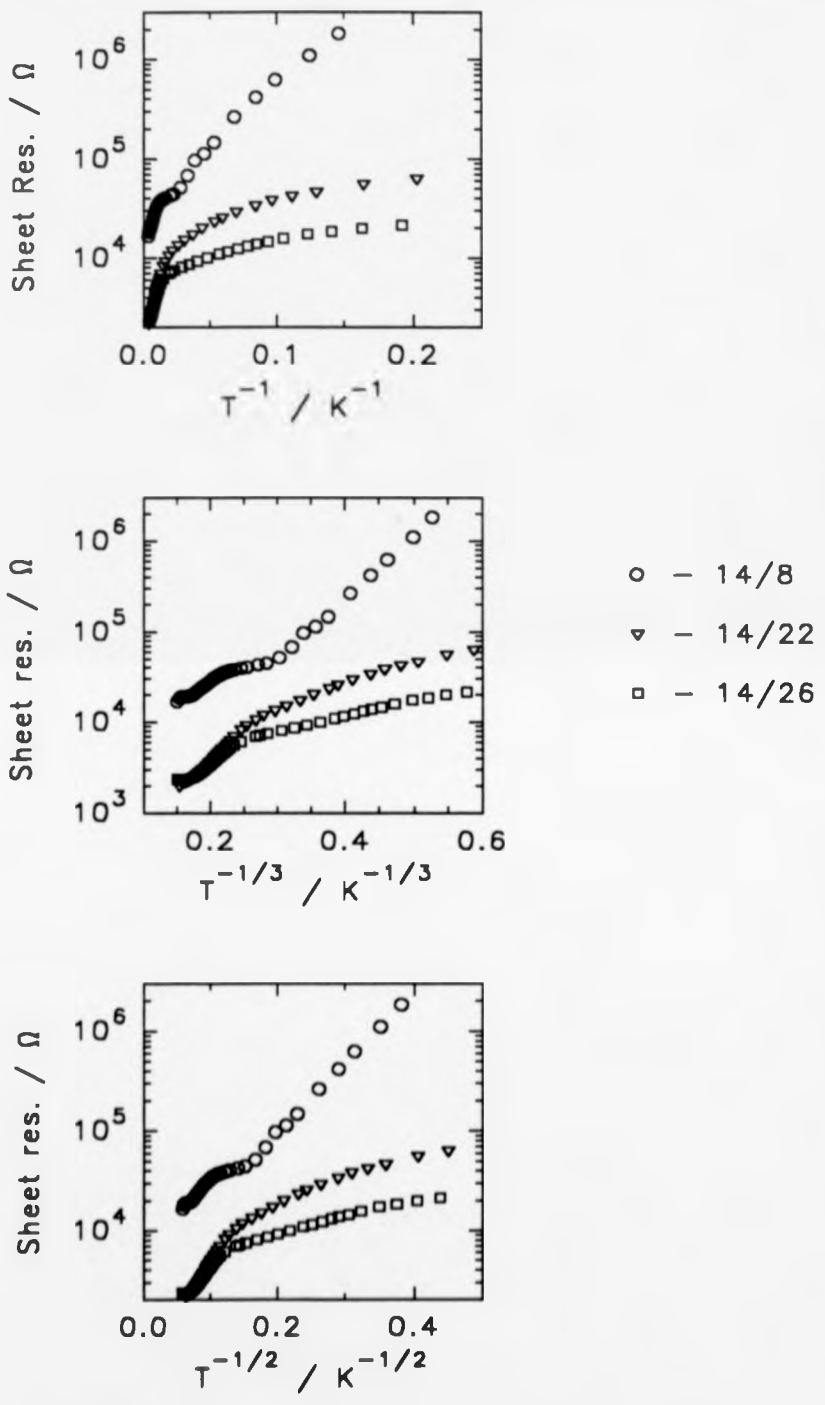

Fig. 4.6 Plots of ρ vs. T, for investigation of the type of hopping or purely activated transport present in the 14/- series of samples

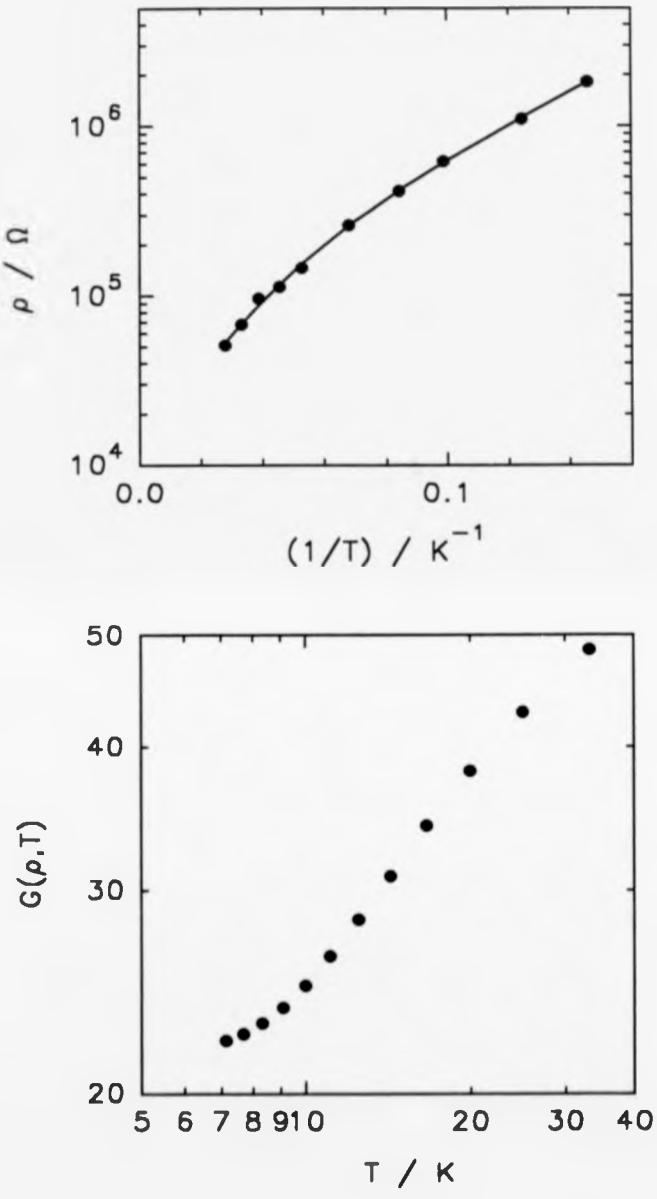

Fig. 4.7 $G(\rho,T)$ plots for determining temperature exponent of resistance in sample 14/8

linear dependences for all the samples at low temperatures (below ~40 K), but most convincingly so for the sample with no growth interrupts (14/8). Values of T_o estimated from both the $T^{-\frac{1}{4}}$ and $T^{-\frac{1}{2}}$ plots are about twice as large as for the equivalent normal structure from the previous growth series (13/34). However, this is further confirmation that the underlying physical process characterising the transport behaviour is random, which is certainly the case with unintentional incorporation of impurities. As with the first series of samples it is not possible by direct plotting of resistance data on $T^{-\frac{1}{4}}$ and $T^{-\frac{1}{2}}$ axes to ascertain whether or not the Coulomb gap theory is appropriate. An attempt was made here by assuming a general temperature dependence of the form $\rho \propto (T_o/T)^{\nu}$ and plotting the function $G(\rho,T)=\partial \ln \rho/\partial(1/T)$ against T on logarithmic axes to extract the straight line gradient, $(1-\nu)$. This was accomplished by making a polynomial fit to the ρ-T data, as shown in the upper part of Fig. 4.7 and then using the functional form of the fit to evaluate $G(\rho,T)$ at various temperatures, as shown. In the rather narrow intermediate temperature range of (10-20) K, the linear relationship present implies a value of $\nu=(0.35\pm0.05)$ which suggests that the conventional Mott 2D VR hopping theory gives a correct description of the conduction process. The reduction of the gradient at high temperatures is expected as the system begins a transition to purely activated conduction, in which case the gradient $(1-\nu)=0$. A study of the deviation at lower temperatures (less than the 5 K minimum in these experiments) would require the use of high impedance measurement techniques.

The metallic nature of the growth environment, with some parts at high temperatures, is likely to be a major cause of impurity contamination. One probable source is the water-cooled Cu hearths in which the Si and Ge charges are located. Despite careful focusing of the electron-beam on the centre of each source, in the case of the Ge, a melt extends as far as the edge, so that Cu comes into contact with a flow of

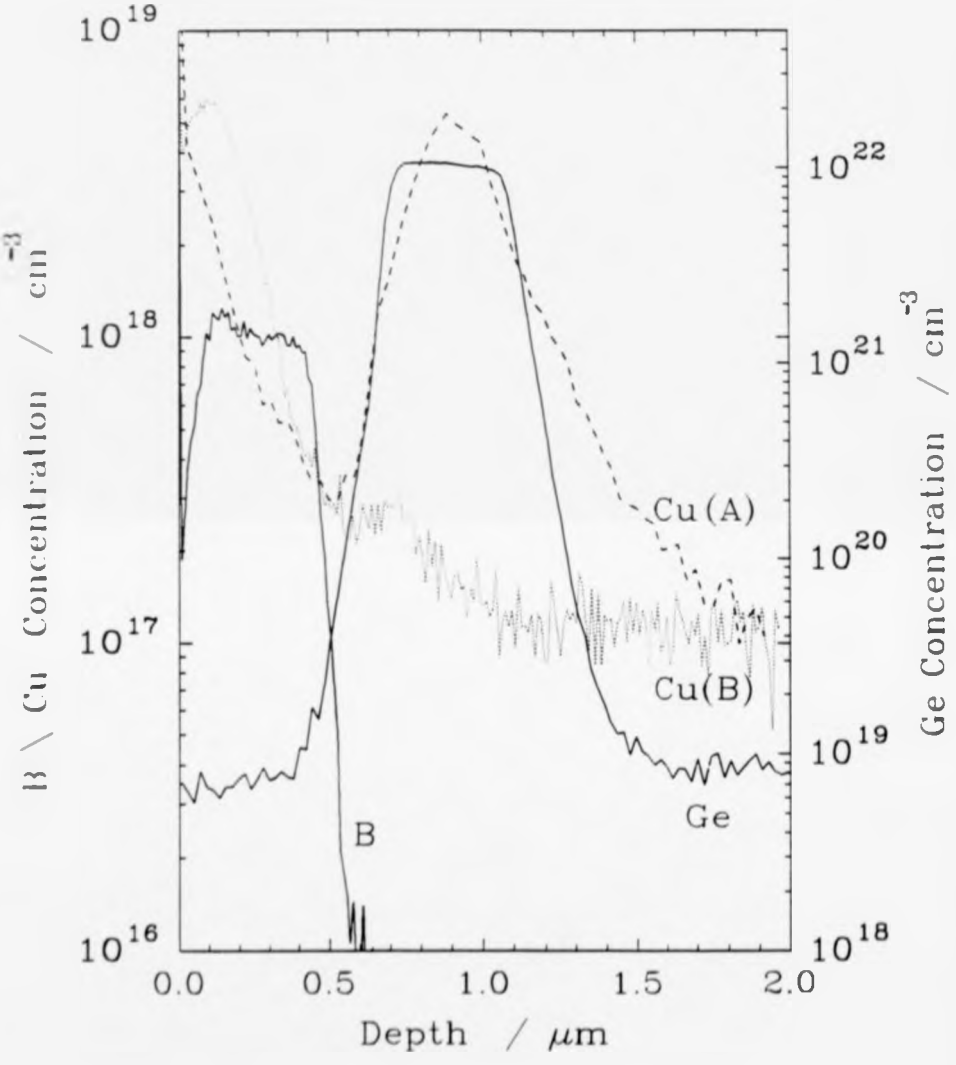

Fig. 4.8 SIMS profiles of Cu, Ge and B in samples 14/8 (A) and 14/26 (B) (from Smith *et al.*, 1992)

Ge: some of this mixture will be evaporated and impinge upon the growing crystal surface. Analysis of the samples by SIMS confirms this effect (Figs. 4.8), where the Cu and Ge signals are seen to be roughly coincident, but with an additional surface concentration of Cu. The comparison of SIMS profiles for samples with and without growth interruption has been made by Smith *et al.* (1992). The profiles show that the Cu concentration in the SiGe region of the growth interrupted sample is almost at the background detection limit, while the surface concentration remains high in both samples. A shoulder is present on the surface Cu peak in the growth-interrupted sample, suggesting that some redistribution of Cu occurs. However, interpretation of the SIMS data presents difficulties, since the apparent peak concentrations (in excess of 10^{18} cm^{-3}) are well above the solid solubility limit for Cu in Si (Hall and Racette, 1964). The presence of Cu precipitates is confirmed by spikes in the profile, reflecting a non-uniform distribution of Cu through the material.

4.1.3 REFINEMENTS TO THE Ge SOURCE

In light of these results, a third set of samples was grown using a modified Ge source. The alteration was simply to house the Ge within a larger piece of Si before locating the whole unit in the Cu hearth. In this way, it was hoped to keep the Ge melt away from solid Cu, with the Si liner remaining solid at the Ge melt temperature of 937 °C (the melting point of Si is 1415 °C). Any further Cu contamination of the epi-layers must be due to solid state diffusion through the Si liner: at 700 °C (a hypothetical average temperature of the Si liner during growth), the diffusion coefficient for Cu in Si is $D=4\times10^{-5}$ cm^2s^{-1} (Hall and Racette, 1964), so that for a growth time of one hour, the diffusion length, $\sqrt{Dt}$, is 0.3 cm, enough to allow significant contamination of the Ge charge, given that the thickness of the Si liner is only a few centimetres. This cause of

contamination is compounded by the fact that the charge may typically be used for 100 hours of growth before being replaced.

The results of transport measurements provide vindication for this development, with a four-fold increase in 4 K mobility, to 2000 $cm^2V^{-1}s^{-1}$. SIMS analysis of the samples was unable to detect the presence of Cu, with the implication that Cu contamination, if present, is at a level below the SIMS detection limit of $\sim 1\times10^{17}$ cm^{-3} (this is seen as a background count rate in Fig. 4.8). Although a direct correlation between the level of the mobility and presence of Cu impurities cannot be proved, the possibility of such a link remains likely. Later on (section 4.2.2), it will be demonstrated that the only scattering potential capable of accounting for the magnitude of the mobility in this new generation of samples (20/- series) is that due to a random distribution of charged impurities inside, or within a screening length of, the quantum well. It is noted that substitutional Cu atoms in SiGe alloys give rise to 3 acceptor levels (Kh. Azhdarov *et al.*, 1992).

Having refined the growth procedure to a point at which high mobility 2DHGs were routinely produced, a number of sample sets were grown to provide material for further, more detailed transport studies. Two experimental parameters were varied: firstly, the undoped spacer thickness, L_s, to provide a sample set with a range of QW hole densities; and secondly, the substrate temperature, to try and acquire an understanding of metallic impurity contamination processes. To conclude this initial report on growth studies, transport results for the variable growth temperature samples are presented, before embarking on a study of subband structure and scattering processes.

4.1.4 VARIATION OF GROWTH TEMPERATURE

The four samples investigated had identical structures (as in Fig. 4.4, but with L_s=20 nm and N_A= 2×10^{18} cm^{-3} and a single 4 minute growth interrupt at the edge of the doping spike), with different substrate temperatures used, in the range 520-640 °C. Transport measurements were carried out at temperatures down to 4 K, and the results for T < 100 K are shown in Fig. 4.9. Table 4.2 contains a summary of the principal transport characteristics of the 2D gases, as extracted from the 4 K data.

Sample ID	T_s / °C	n_s / cm^{-2}	μ / $cm^2V^{-1}s^{-1}$
20/53	520	2.9×10^{11}	1250
20/49	550	3.3×10^{11}	2200
20/52	580	2.9×10^{11}	3250
20/54	640	2.5×10^{11}	3650

Table 4.2 Transport parameters for samples grown with different substrate temperatures

Clearly, there is a very dramatic increase in mobility with growth temperature; but, in addition, the hole density varies from sample to sample, even though the sample doping is nominally the same in each case.

The variation in mobility may be understood if the dominant scattering process is charged interface impurity scattering. The effect of increasing growth temperature is to enhance solid state diffusion rates; thus, in the case of Cu doping of the SiGe region during growth, the impurity contamination of the quantum well region should decrease via solid state diffusion processes. However, a lack of knowledge concerning which impurity species are present, and at what concentration, prevents a quantitative analysis of the data.

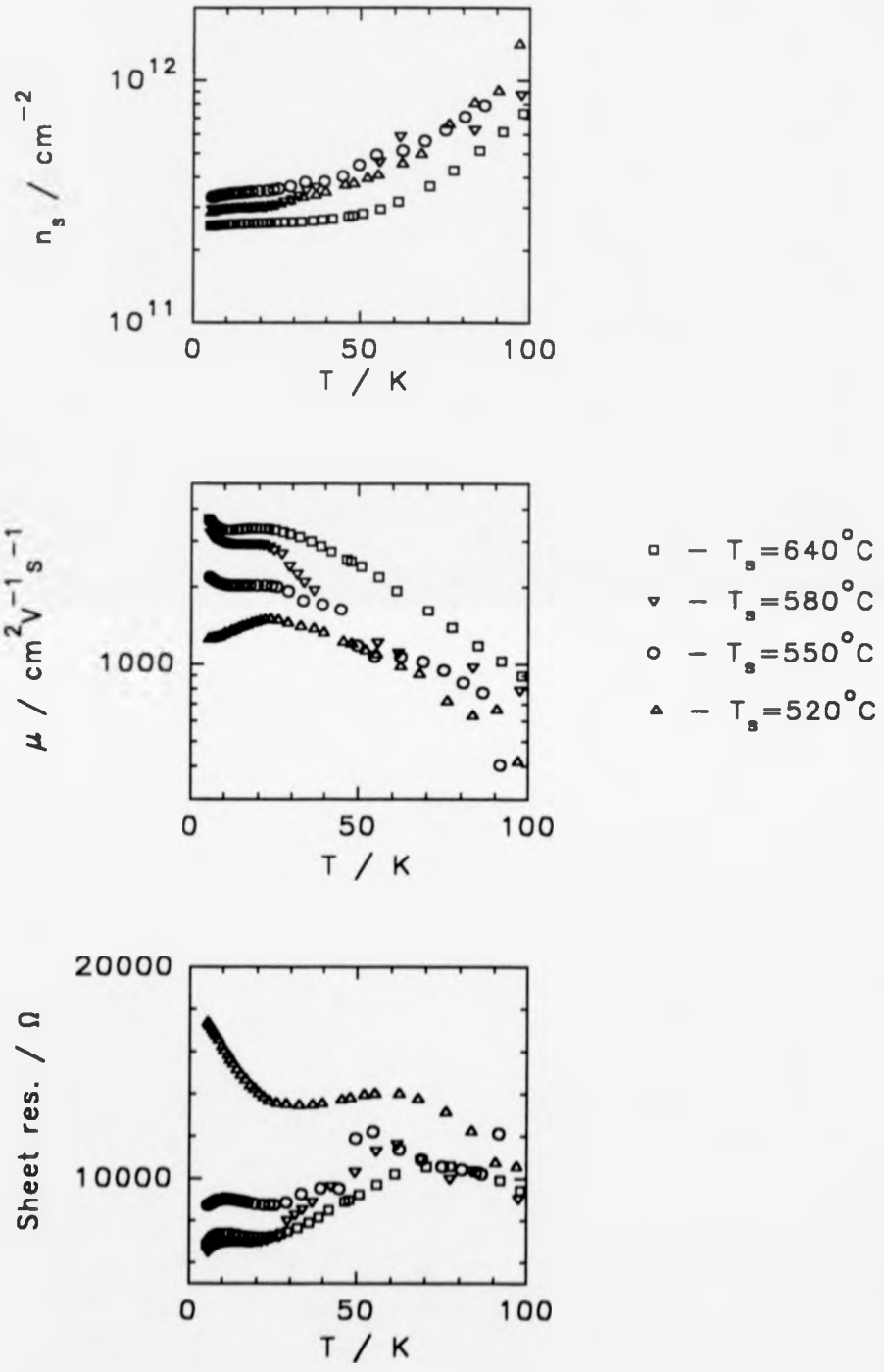

Fig. 4.9 Transport results (n_s, μ and ρ vs. T) for the 20/- series of samples

The variation of QW hole density with T_s is not completely understood. In normal doped samples, one expects that L_s should increase with T_s up to $\sim 650°C$, due to the kinetically limited phase of the B surface accumulation process (section 3.1.2), with a corresponding decrease in n_s. It will be shown in section 4.2.1 that a change in sheet density from $3.3 \rightarrow 2.5 \times 10^{11}$ cm^{-2} can be accounted for by an increase of about 5 nm in L_s: this value is consistent with the growth temperature dependence of leading edge (surface side) accumulation lengths for B doping in Si MBE at a level of $\sim 5 \times 10^{18}$ cm^{-3} (Parry *et al.*, 1991), although the data for the substrate side of the doping spike, as relevant to this work, is not available. The lower value of n_s at $T_s = 520$ °C is unexpected and cannot be explained by the author. The result is not due to random error, as this would be evident as noise in the μ-T plots (Fig. 4.9). The difference from a value consistent with the other 3 samples ($> 3 \times 10^{11}$ cm^{-2}) is also too large to be attributable to systematic errors in the Hall measurements, such as those associated with sample geometry.

4.2 SUBBAND STRUCTURE AND SCATTERING MECHANISMS

Nine samples from the 20/- series with different spacer layer thicknesses (and hence hole densities) have been characterised by resistance and Hall measurements down to temperatures of ~5 K. In the following section (4.2.1), 5K sheet densities are compared with theoretical estimates obtained using a model developed by the author. Subsequently, limiting hole mobilities due to all the likely scattering mechanisms are calculated as a function of hole density and plotted alongside the experimental mobility data (section 4.2.2).

4.2.1 SUBBAND STRUCTURE IN THE QUANTUM WELL

In chapter 2 (section 2.2.4), a mathematical description of the variation of the band potential across the heterojunction was given. In order to determine how many holes transfer from the B-doped region to the SiGe, it is necessary to solve the series of equations (2.2.1-2.2.24) self-consistently. Fortunately, a lot of elimination of unknown variables may be carried out, leaving two equations for n_s in terms of E_F and L_s. These have been solved simultaneously, for chosen values of L_s, using a BASIC computer program, in which the main routine is simply to increase E_F from zero, with increments of 0.5 meV, until some convergence is observed as one value of n_s exceeds the other: the process is then repeated, having subtracted 0.5 meV from the last value of E_F, this time using steps of +0.01 meV, but applying the same convergence condition.

Results of the sheet density, n_s, for various values of impurity density, n_i, and

depletion charge, N_{Depl}, are shown in Fig. 4.10. In the discussion of scattering mechanisms which follows this section, a value of $n_i = 2\times10^{11}$ cm^{-2} is needed to give any feasible explanation for the experimental data: taking this value, a reasonable fit to the n_s-L_s data is made with $N_{Depl} = 1\times10^{11}$ cm^{-2}. This value of depletion charge lies within the expected bounds, given that some uncertainty exists over the background doping level which prevents an accurate estimation of the depletion field in the well (section 2.2.4). Numerical results for this best fit to the data are contained in Table 4.3, along with an estimate of the width of the quantum well, a, found from $e\varphi(a) = E_o$ [$\varphi(z)$ is given by (2.2.18)].

It is interesting to see that if the background doping has a concentration of the order of 10^{15} cm^{-3} (n-type), so that $N_{Depl} = 1.7\times10^{11}$ cm^{-2}, then it is essential to invoke the presence interface charge, otherwise, as the calculations show, with $n_i = 0$ no holes transfer to the SiGe for $L_s \geq 40$ nm, which is at odds with the experimental observation. Direct evidence for the presence of negatively charged impurity states at the Si/SiGe heterojunction in this material at similar sheet densities has been found in capacitance-voltage (C-V) profiling studies (Brighten *et al.*, 1992). It proved impossible to use the same technique to investigate material from the previous (13/- and 14/-) growth series, because large leakage currents caused breakdown of the Schottky barriers necessary for the C-V profiling technique: this is a reflection of the higher levels of impurity contamination in the earlier material.

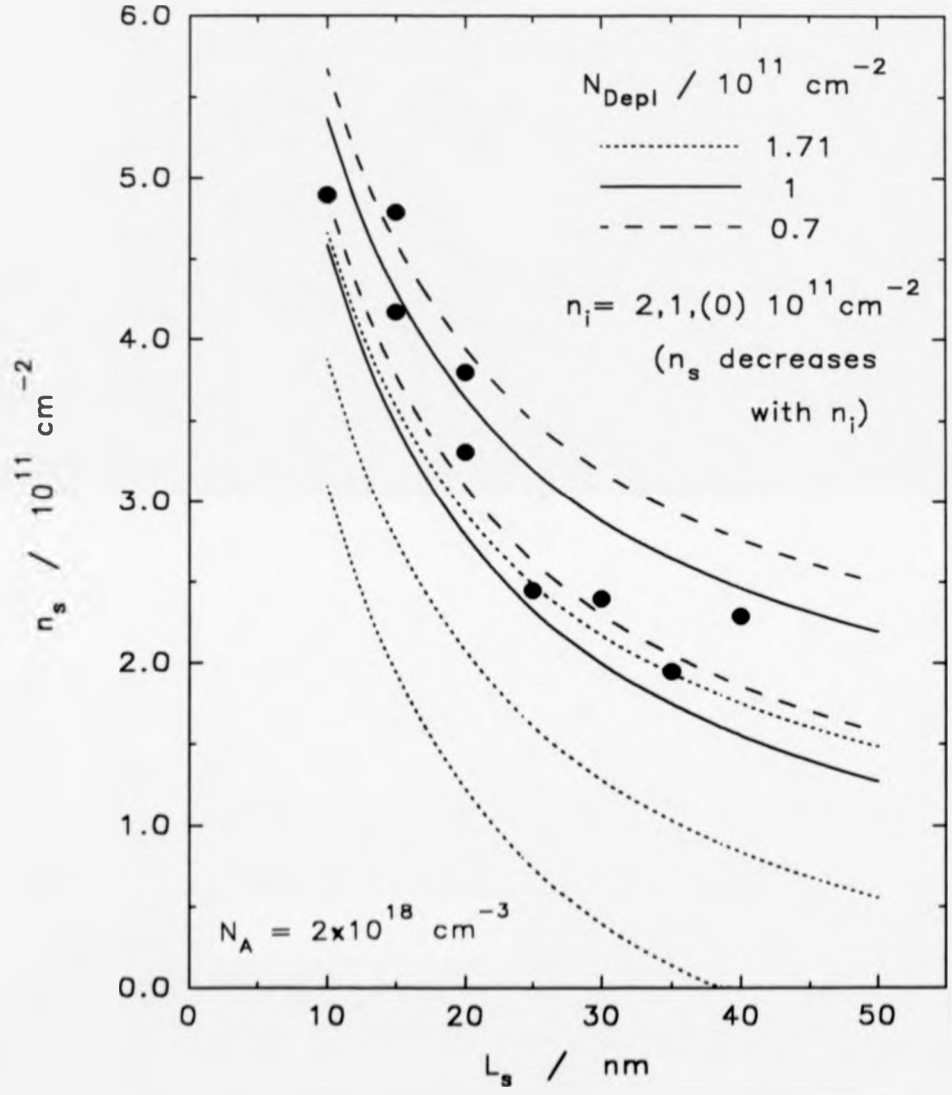

Fig. 4.10 2DHG density dependence on structural and doping parameters

L_s / nm	n_s / 10^{11} cm^{-2}	E_o / meV	E_F / meV	a / nm
10	5.367	42.90	4.03	5.887
12	4.867	40.70	3.65	6.044
14	4.467	38.89	3.35	6.183
16	4.140	37.39	3.10	6.306
18	3.869	36.11	2.90	6.416
20	3.639	35.02	2.73	6.515
22	3.443	34.08	2.58	6.605
24	3.274	33.26	2.45	6.686
26	3.127	32.53	2.35	6.760
28	2.997	31.89	2.25	6.828
30	2.882	31.31	2.17	6.890
32	2.780	30.80	2.08	6.948
34	2.688	30.33	2.02	7.001
36	2.605	29.91	1.95	7.051
38	2.530	29.52	1.90	7.097
40	2.462	29.17	1.84	7.139
42	2.399	28.84	1.80	7.180
44	2.341	28.54	1.76	7.217
46	2.288	28.27	1.71	7.252
48	2.239	28.01	1.68	7.286
50	2.194	27.77	1.64	7.317

Table 4.3 Numerical results for well parameters based on the best fit to the n_s-L_s data.

4.2.2 MOBILITY-HOLE DENSITY RESULTS

Experimental data are shown in Fig. 4.11. The first point to note is that there is no clear correlation between the data points. There is conceivably a trend towards lower mobility at higher values of hole density, but the large scatter in the data, far greater than that expected for experimental uncertainty or error, undermines such an assertion. This is further evidence that the origin of the dominant scattering mechanism is random in character: unintentional impurity contamination levels would be expected to vary from wafer to wafer, as the cleanliness of the growth chamber evolves with time. Charged interface impurity and interface roughness scattering are likely to dominate, but alloy scattering and remote impurity scattering are also inherently present. It is therefore necessary to estimate the scattering rates for all likely hole-imperfection interactions, in order to establish which constitute the principal mobility limiting mechanisms.

Appropriate expressions for the scattering rate in each case have been quoted and, if necessary, adapted in section 2.3.4, where also values for relevant material parameters are given. The resulting mobilities are plotted in Fig. 4.11, alongside the experimental data.

The immediate conclusion to be drawn is that only charged interface impurity scattering, with $n_i \sim 2\times10^{11}$ cm^{-2}, is capable of accounting for the observed magnitude of the mobility. This does imply a very high level of contamination in the MBE system, but, significantly, the same value of n_i is needed to give a satisfactory explanation for the observed n_s-L_s dependence.

Remote ionised B-atoms and alloy potential fluctuations are seen to have a negligible associated scattering rate in the context of these experiments. Values for short and long-range interface roughness scattering rates are also insignificant (taking a mixture of measured and, where necessary, estimated values for the roughness parameters Δ and Λ). In any case, the minimum possible roughness scattering mobility, obtained in the

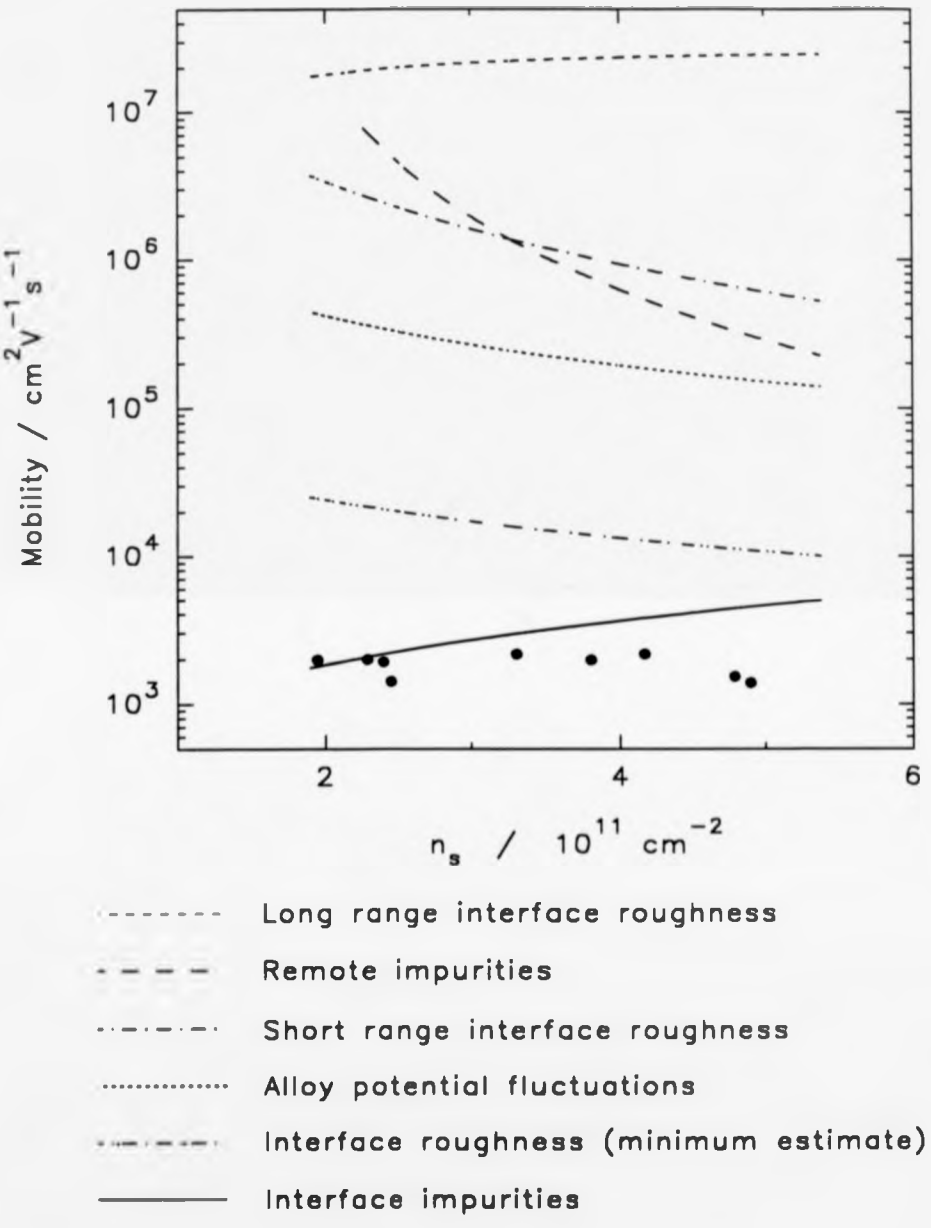

Fig. 4.11 Calculated limiting mobilities for the various scattering mechanisms

limit $k_F\Lambda \sim 1$, is still an order of magnitude larger than the experimental data. While the appropriate value of Λ might be unphysical, a lack of experimental knowledge of the interface morphology in the short range limit means that it is important to establish whether or not interface roughness scattering is able to account for the experimental results: in this case, it is not able to do so.

4.3 EXPERIMENTS AT LOW TEMPERATURES AND IN HIGH MAGNETIC FIELDS

4.3.1 INTRODUCTION

In these experiments, four of the samples from the 20/- series previously characterised down to 4 K were investigated further: three of them (20/18,44 and 46) providing a range of QW hole density and the other (20/54) included because of its significantly lower level of structural disorder. The experimental procedures followed are described in section 3.2. Major experiments performed were the measurement of magnetoresistance (MR) in fields up to 12 T and at low temperatures (0.3 K or $\sim$1.5 K), and the measurement of resistance and Hall coefficient at temperatures in the range 0.3-20 K.

4.3.2 MAGNETORESISTANCE MEASUREMENTS

The use of Hall bars enables the direct measurement of two resistance tensors, ρ_{xx} and ρ_{xy}. The large values of magnetic field used (up to 12 T) were established by ramping up the field slowly ($\leq$1 Tmin^{-1}) in order to avoid excessive eddy current heating and the associated unnecessary boil off of ^{4}He used to keep the magnet cold. Consequently, MR measurements were made with a single polarity of B-field only, instead of taking dual polarity measurements at each field, necessary for the elimination of zero-field offsets in the Hall voltage (these are caused by defects in the sample geometry). This was dictated by the constraints of a maximum hold time at base temperatures (90 minutes at 1.4 K, the usual base temperature of the 1K pot, and 3 hours at 0.3 K when pumping on the full charge of ^{3}He) and the necessity of obtaining enough

data points to resolve all the structure in the MR. Zero-field offsets are negligible, but are just visible for some samples where the Hall resistance fails to intercept the origin of (ρ_{xy},B) co-ordinates. Results for all 4 samples are presented in Figs. 4.12-4.23.

Examining the ρ_{xx} data first of all, there are two regions in each sample with distinctive behaviour. At very low magnetic fields ($\leq$0.5 T) the MR is negative, which is due to quenching of the weak localisation contribution to the resistance (section 2.3.6). Above 0.5 T the MR turns positive and once the field exceeds $\sim$1 T oscillations appear, periodic in 1/B, as the Landau quantisation of the ($M_J = \frac{1}{2}$) ground state becomes resolved. The Hall resistance shows related behaviour: at low fields the gradient $\partial\rho_{xy}/\partial B$ is constant and equal to the Hall coefficient; but as oscillatory behaviour in the MR commences, accompanying structure is seen in ρ_{xy}-B data, with the formation of plateaux, or in some cases adjacent local maxima and minima, above $\sim$5 T. Since the physical origins of the low and high field MR are different, each one will be considered separately.

4.3.2.1 LOW FIELD PERPENDICULAR MAGNETORESISTANCE

A theoretical expression for the low field magnetoconductance associated with the quenching of weak localisation, (2.3.38), has the general form $\Delta\sigma_{xx}(T,B)=\alpha f(T,B)$, where f is always greater than zero and α is a spin-scattering factor. In this work, the observation of negative MR is consistent with a positive value of α, implying that spin-spin and spin-orbit scattering effects, if present, are not dominant. This is in contrast to other related 2D hole systems such as Si:B δ-layers (Mattey *et al.*, 1992) and Ge bi-crystals (Landwehr and Uchida, 1986), 2DHG inversion layers in Si MOSFETs (Gusev *et al.*, 1982) as well as bulk Si:B samples (Dai *et al.*, 1992): in all these cases,

the positive low field MR and hence negative value of α are indicative of strong spin-orbit scattering (section 2.3.6).

However, in the author's samples, strain locked into the alloy layers causes the LH-HH zone-centre degeneracy associated with cubic Si or Ge to be lifted (section 2.2), such that ΔE_{LH-HH} is much greater than the Fermi energy: as a result, transitions between $J = \frac{1}{2}$ and $J = \frac{3}{2}$ states are suppressed, with the consequent elimination of spin-orbit scattering [this was first suggested by Al'tshuler *et al.* (1981a) in connection with the piezo-magnetoresistance of p-type Ge (see reference 12 in the aforementioned work for citation of relevant experiments)]. In section 4.3.3, analysis of the temperature dependences of σ_{xx} and R_H yields values of α in the range 0.1-1.0; however, no consistent explanation for the departure of α from unity can be found.

The increase in resistance at fields above ~0.5 T, before the onset of Shubnikov-de Haas oscillations, is considered to be caused by a decrease of interaction between spin-up and -down states, which occurs once the Zeeman splitting energy, $g\mu_B B$, exceeds the thermal energy, kT. In this case, g is a convolution of the hole momentum state ($J = \frac{3}{2}$) and the effective Landé g-factor for the system. This matter is complicated somewhat by the strain distribution in the alloy layers: the non-cubic nature of the unit cell is responsible for anisotropy in the g-factor, with observed values of ~4.5 appropriate to fields perpendicular to the 2D gas and ≤0.4 for fields parallel to the gas (Glaser *et al.*, 1990). Tilted-field MR investigations of 2DHGs in strained and unstrained SiGe alloys (with the latter grown on relaxed buffer layers, as described in section 1.3) have brought confirmation that strain is the origin of the g-factor anisotropy (Fang *et al.*, 1992)

It is possible to obtain a reasonable fit to the low-field MR data using a combination of (2.3.38) and (2.3.46): this is illustrated for sample 20/44 in Fig. 4.22, taking g=4.5, α=0.60 [using the value of α_p deduced from analysis of the σ_{xx}-T data (Table 4.5) and

assuming that p=1] but with a higher value for F* of 1.4, compared with F*=(0.92±0.12), as obtained from analysis of the R_H-T data. Discrepancy between magnetic and thermal estimations of F* has also occurred in work on electron inversion layers in Si MOSFETs (Burdis and Dean, 1988) and, to the author's knowledge, this problem remains unresolved. The extracted value for the phase coherence length of 160 nm is in agreement with the theoretical value calculated using (4.3.1).

4.3.2.2 PARALLEL FIELD MAGNETORESISTANCE

As a check on the dimensionality of the hole gases, resistance measurements were also performed on one sample (20/44) with the '2D' gas aligned parallel to the magnetic flux inside the solenoid: results are shown in Fig. 4.23. In a perfect 2D system, one would expect to see only positive MR resulting from the (isotropic) Zeeman splitting of anti-parallel spin-states for this B-field orientation: as such, the fact that the low field MR is negative up to ~3 T, due to quenching of weak localisation, signifies a quasi two-dimensionality of the system, which reflects the finite spatial extent of the 2DHG perpendicular to the heterointerface (section 2.2.4). Using (2.3.40) to fit to the data below 2 T, a value of ~4 nm is estimated for the width of the 2D gas, compared with a theoretical estimate of 6.4 nm (Table 4.3). It is noted that the cyclotron length, l_c, in the maximum applied field of 12 T is 7.4 nm, just larger than theoretical estimates of the well width: hence, in a parallel field geometry, the Landau orbit size is always greater than the confining distance perpendicular to the field (in this case, the well width), so that no oscillatory structure is expected in the MR: this is confirmed by experiment.

The fact that the resistance minimum in the parallel-field orientation occurs at a magnetic flux density about ten times greater than for the minimum in a perpendicular field supports the notion of a strong anisotropy of the g-factor, as reported in the previous

section (4.3.2.1). Finally, it is noted that the high parallel field MR was larger than expected from the Zeeman spin-splitting magnetoconductivity theory (2.3.46); this problem also being encountered by Burdis and Dean (1988) in their work on electron inversion layers in MOSFETs.

4.3.2.3 HIGH PERPENDICULAR FIELD MAGNETORESISTANCE AND QUANTISED HALL RESISTANCE

Shubnikov-de Haas oscillations present in the high field MR of all the samples provide the best means of estimating the carrier density, n_s, of the 2DHGs (section 2.4). Values of n_s can be deduced from the low field Hall coefficient measured at low temperatures (hence with the doping spike frozen out) but there is a large associated uncertainty due to quantum corrections present in ρ_{xy} arising from interaction and localisation effects (section 4.3.3 and Fig. 4.25). The best resolution of the oscillatory structure in the MR is achieved at the lowest attainable temperatures (0.3 K), such that thermal broadening of the Fermi surface is as low as possible. This is demonstrated for sample 20/46 in Fig. 4.17, where data taken in the field range 0-6 T at two temperatures, 1.61 K and 0.33 K, is plotted on the same axes: for this reason most of the samples were investigated only at 0.3 K.

The most important feature of the magnetotransport data is the existence of odd as well as even filling factor Hall plateaux in the plots of ρ_{xy}-B data. This provides confirmation that each subband is split into its two constituent ($M_j=\pm\frac{1}{2}$) spin components (the Zeeman effect). If the two-fold spin degeneracy were not lifted by the magnetic field then the Landau level degeneracy, as calculated in section 2.4, would be twice as large, with the Hall resistance following as $(h/2\nu e^2)$. The lower density samples (20/18 and 54) exhibit a $\nu=1$, $\rho_{xy}=h/e^2$, plateau, formed before reaching the maximum

accessible field of 12 T (see Figs. 4.12 and 4.19 respectively). All the samples show a ν=2 plateau (or in some cases, just a semblance of one), which occurs in the range of field co-incident with the up-slope ($\partial\rho_{xy}/\partial B > 0$) of the highest field MR peak. Most of the samples show a third plateau, or some type of peak-dip structure, with $\rho_{xy} \sim 0.4(h/e^2)$, not quite corresponding to the ν=3 filling factor for which theory predicts $\rho_{xy}=h/3e^2$, but nevertheless always at a field higher than the second highest field MR peak: this reflects the doublet spin composition of each of the MR peaks. The exact magnitude of the g-factor ($\sim$4.5, as reported by Fang *et al.*, 1992) determines which Landau level spin states overlap. The reason for this anomalous value of ρ_{xy} is simply that the value of ρ_{xx} is much greater than zero.

In section 2.4, it was explained how the filling factors of the resistance peaks or minima can be used to determine the carrier density. In this case, since each MR maximum corresponds to the convolution of spin-up and spin-down peaks, the value of the magnetic field co-incident with each peak might be assumed to correspond to an integral filling factor. In the high field peak, spin-splitting structure is observable in two samples (20/46 and 54) with a shoulder present on the low field side of the peak (Figs. 4.16 and 4.19). The high field peak is therefore more correctly labelled by $\nu=\frac{1}{2}$, rather than by ν = 2, as would be the case for closely spaced spin-split Landau levels. This is demonstrated for the three samples measured at 0.3 K in Figs. 4.15, 4.18 and 4.21, where the high field peak labelled by $\nu=\frac{1}{2}$ lies on a straight line fit to the $\nu\geq4$ data based on (2.4.2). The values of carrier density deduced from these fits are contained in Table 4.5. It is noted that the Landau level energies do not have a linear dependence on B-field in 2DHGs based on other strained heterostructures, such as the $Ga_{1-x}In_xSb$/GaSb system (Martin *et al.*, 1990). Calculations of the Landau fan diagrams in the valence bands of strained Si/SiGe heterostructures have yet to be performed.

Lower temperature measurements on these samples are needed in order to observe spin-splitting behaviour directly as resolved MR peaks. However, new, higher mobility

material grown recently at Warwick, with $\mu \geq 10{,}000$ $cm^2V^{-1}s^{-1}$, does show two separate peaks appearing in place of the highest MR peak seen in this work, with a Hall resistance plateau of value $\rho_{xy}=0.5(h/e^2)$ located in the intermediate region. This behaviour has also been observed by Fang *et al.* (1992) in 2DHGs with $\mu \sim 7000$ $cm^2V^{-1}s^{-1}$ formed in strained Si/SiGe heterostructures.

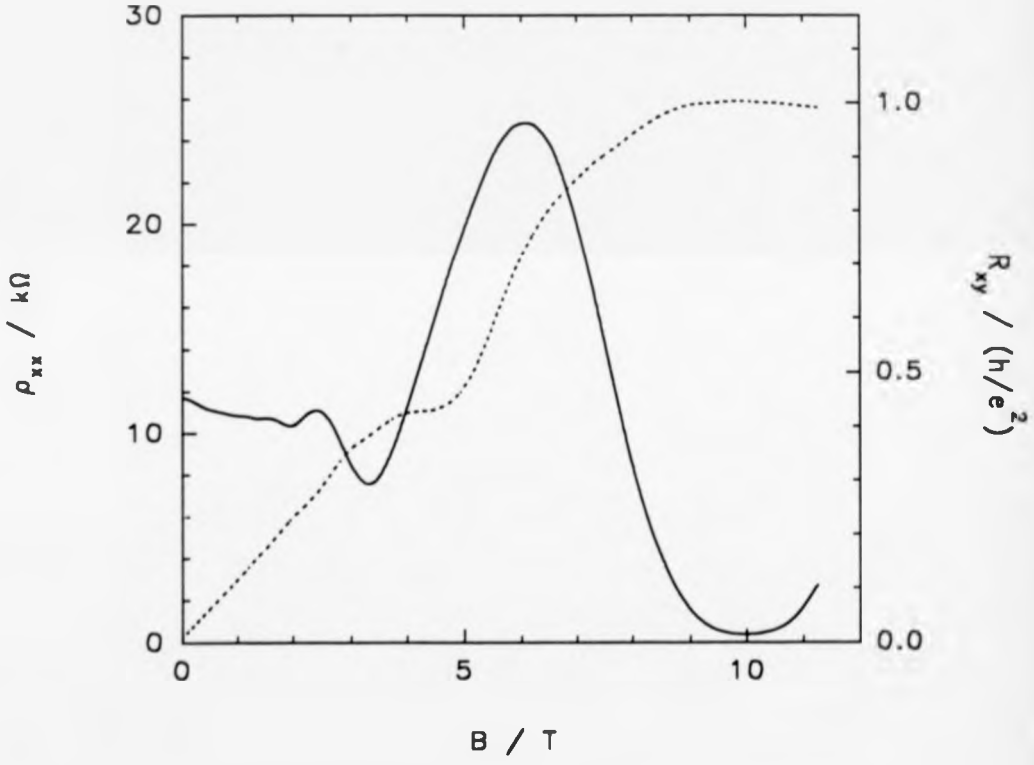

Fig. 4.12 Magnetotransport data (ρ_{xx} and ρ_{xy}) for 20/18 at T = 1.46 K

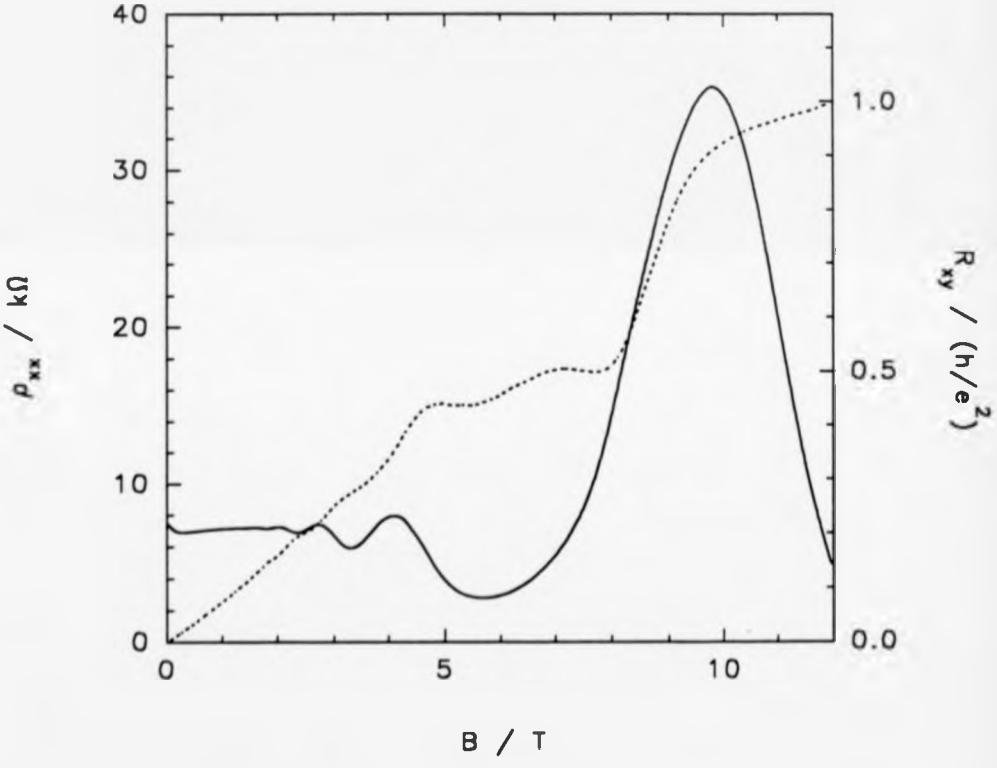

Fig. 4.13 Perpendicular field magnetotransport data (ρ_{xx} and ρ_{xy}) for 20/44 at T=0.33 K

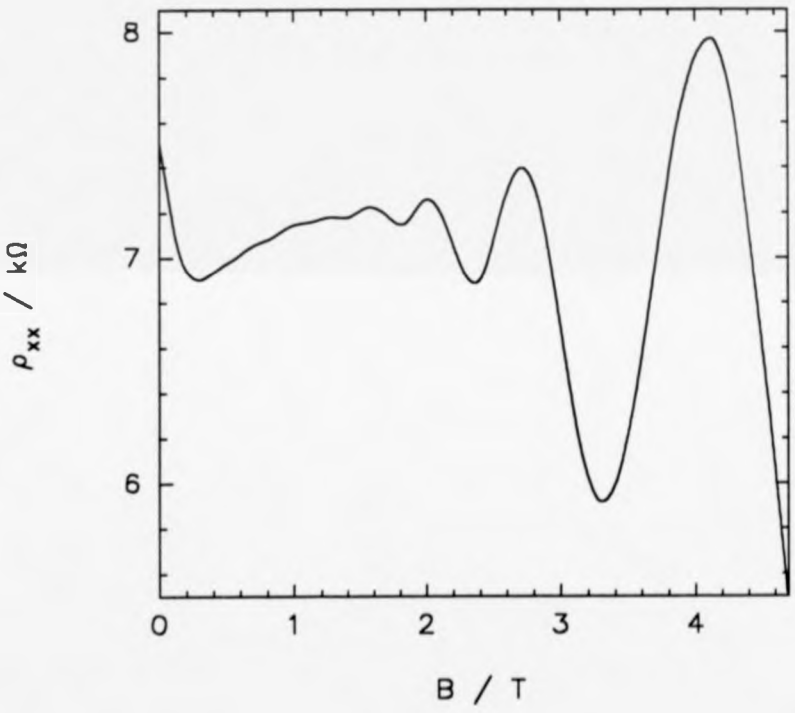

Fig. 4.14 Low perpendicular field MR (0-6 T) for 20/44 at T=0.33 K

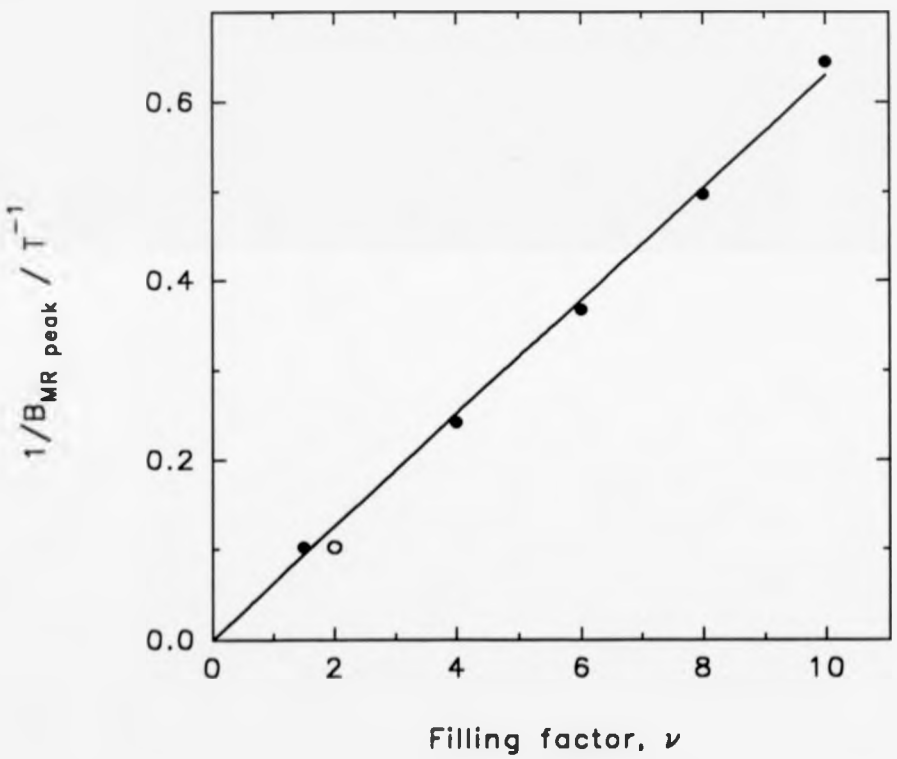

Fig. 4.15 Magnetic field at 0.33 K MR peaks as a function of filling factor for 20/44 (note that the highest field peak is better described by a $\nu=\frac{1}{2}$ than $\nu=2$ filling factor). The solid line is a fit to the $\nu\geq4$ data.

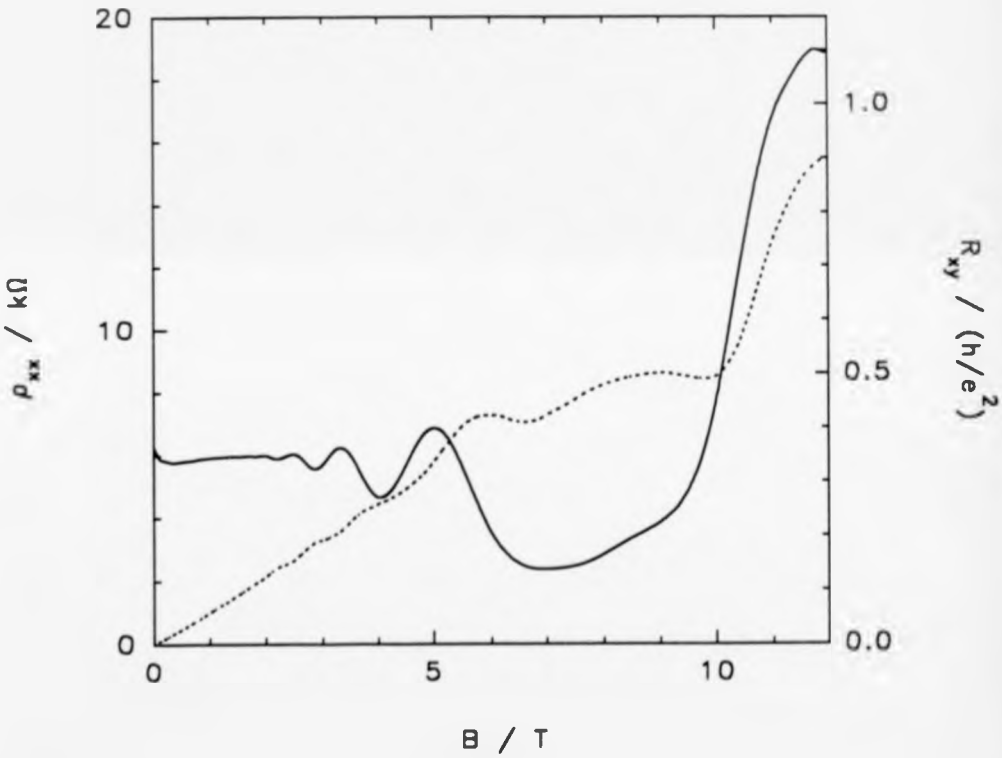

Fig. 4.16 Perpendicular field magnetotransport data (ρ_{xx} and ρ_{xy}) for 20/46 at T=0.33 K

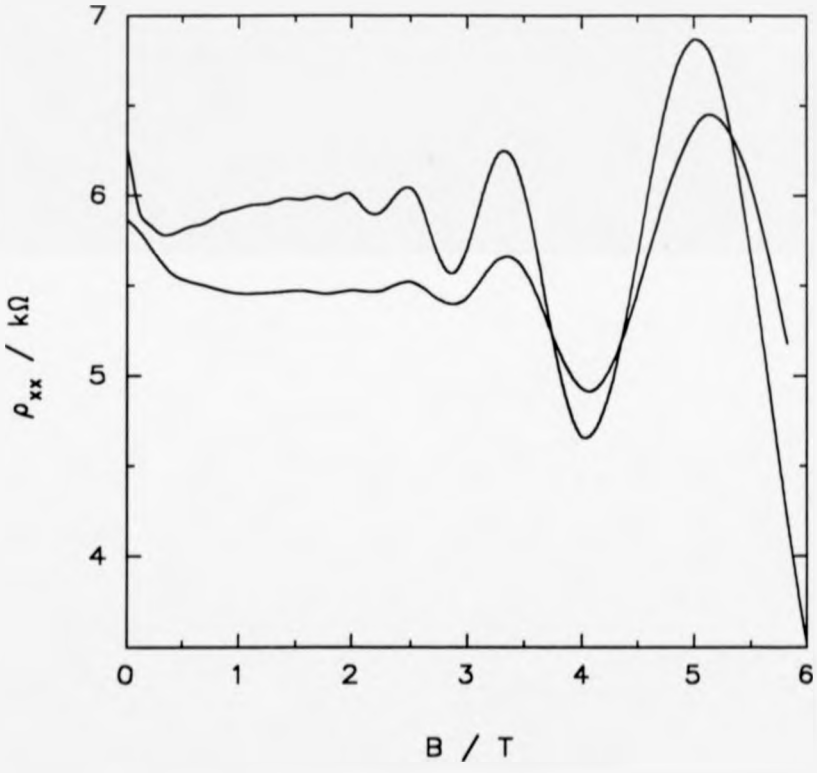

Fig. 4.17 Comparison of (0-6) T perpendicular field MR data for 20/46 taken at 0.33 and 1.61 K (the lower temperature MR exhibits larger oscillation amplitudes)

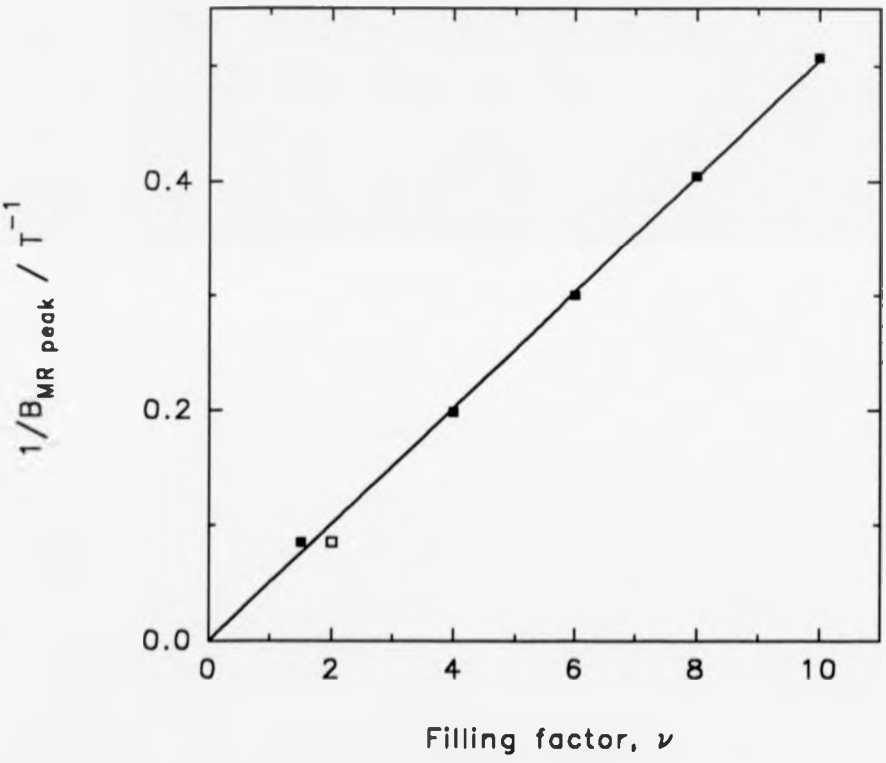

Fig. 4.18 Magnetic field at 0.33 K MR peaks as a function of filling factor for 20/46 (note that the highest field peak is better described by a $\nu=\frac{1}{2}$ than $\nu=2$ filling factor). The solid line is a fit to the $\nu\geq4$ data.

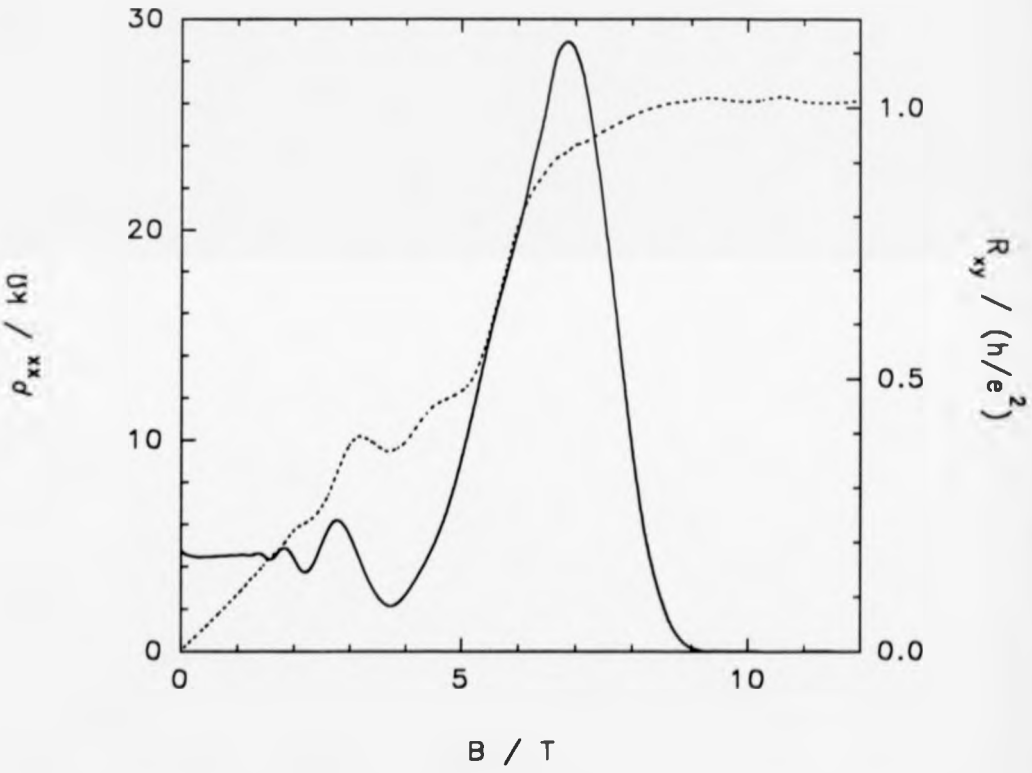

Fig. 4.19 Perpendicular field magnetotransport data (ρ_{xx} and ρ_{xy}) for 20/54 at T=0.32 K

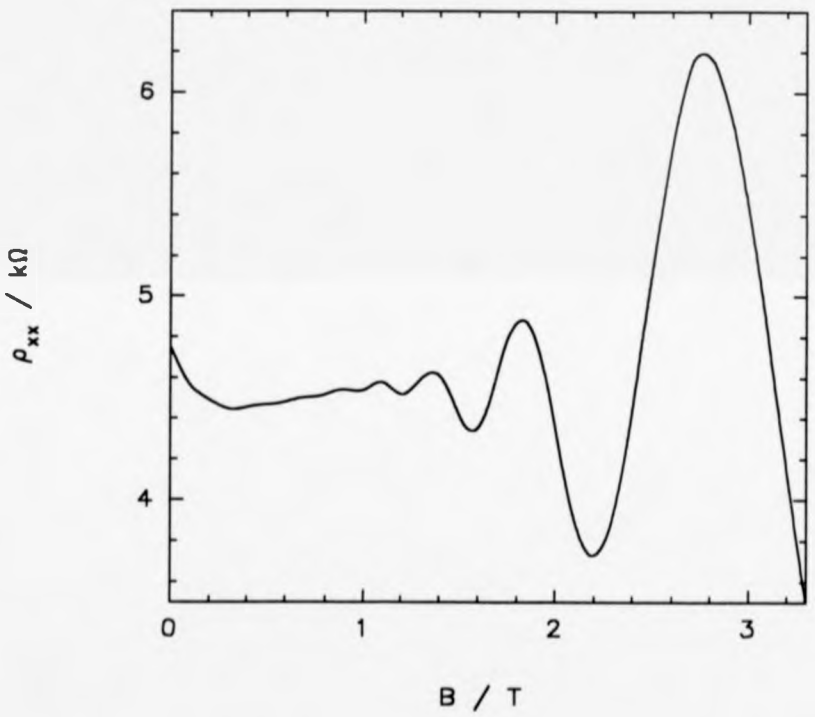

Fig. 4.20 Low perpendicular field MR (0-6 T) for 20/54 at T=0.32 K

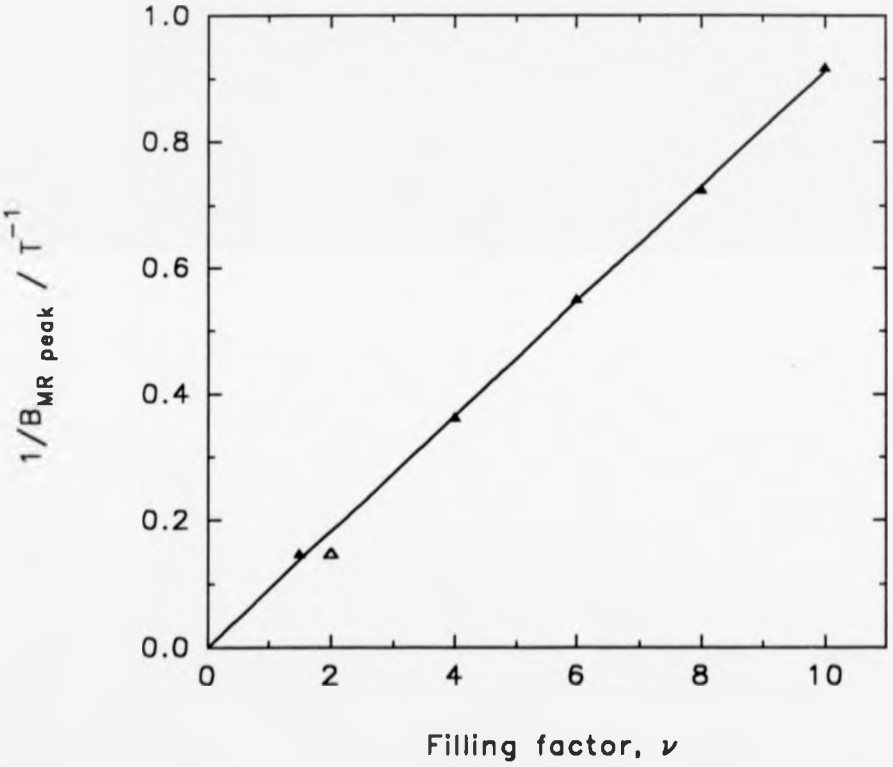

Fig. 4.21 Magnetic field at 0.32 K MR peaks as a function of filling factor for 20/54 (note that the highest field peak is better described by a $\nu=\frac{1}{2}$ than $\nu=2$ filling factor). The solid line is a fit to the $\nu\geq4$ data.

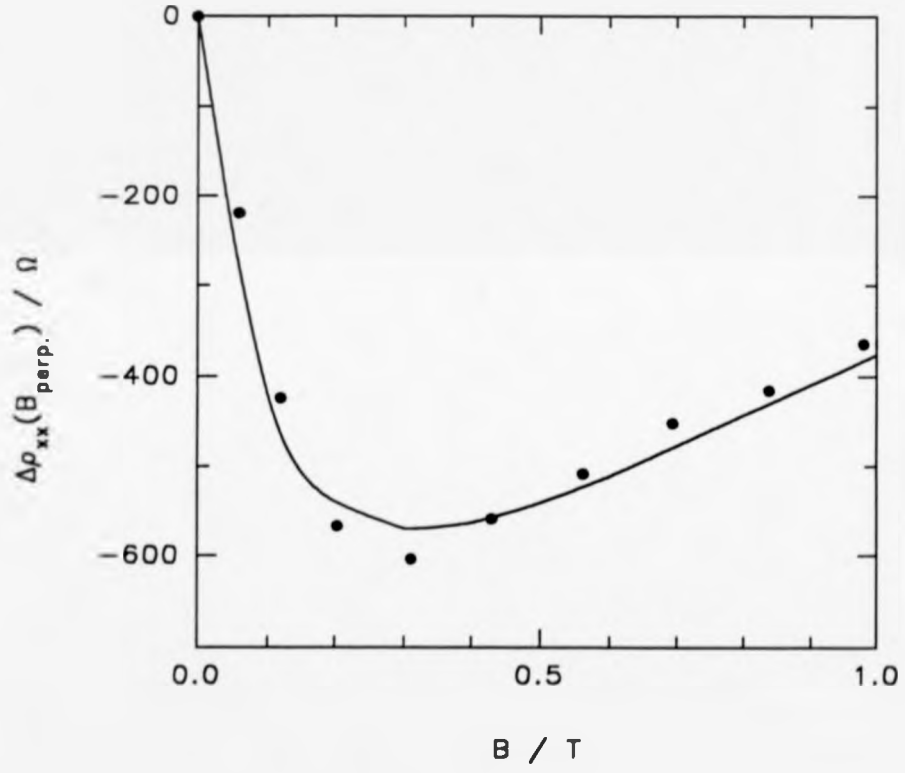

Fig. 4.22 Low perpendicular field MR (0-1 T) for 20/44 at 0.32 K (solid line is a theoretical fit)

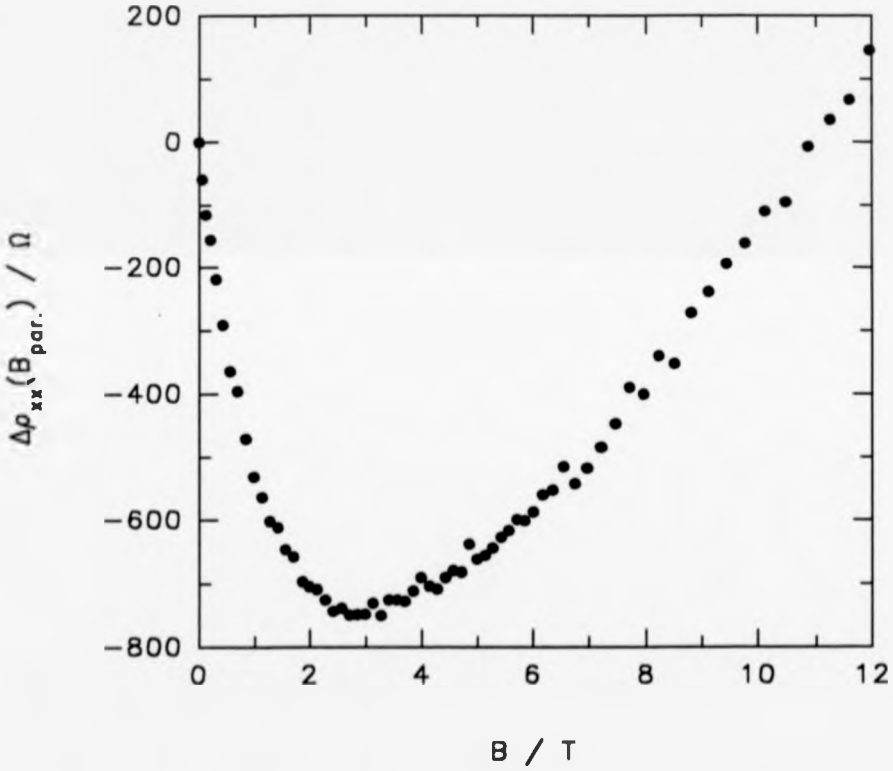

Fig. 4.23 Parallel field MR (0-12 T) for 20/44 at 0.35 K

4.3.3 TEMPERATURE DEPENDENCE OF THE CONDUCTIVITY AND HALL COEFFICIENT

4.3.3.1 INTRODUCTION

An initial investigation was made on one sample (20/18), across the whole region of accessible temperatures (0.3-300 K). This necessarily involved the use of two different cryostats (see section 3.2.3), and therefore a little overlap of the measured temperature ranges in each cryostat was allowed, in order to check for continuity in ρ_{xx} and R_H. In both cases, the same electrical measurement techniques were applied: 7.4 Hz a.c. sample current with lock-in voltage detection, making sure that the same phase angle for V_{meas}/I_{input} was used throughout.

In the plots of σ_{xx} and n_s against temperature (Figs. 4.24 and 4.25), it is clear that there are small but significant discontinuities between the sets of data taken in different cryostats. The discrepancy is too large to be attributable to disagreement between the different thermometers used at low and high temperatures, but in any case, both sets of data exhibit a minimum at the same temperature, to within measurement uncertainty, such that the reproducibility of this physical property, corresponding to the transition from screening effects to non-degenerate behaviour as the dominant contribution to the temperature varying part of the Boltzmann conductivity, in itself confirms a good agreement between the two thermometer calibrations.

The change in resistance is about 1.5%, roughly twice that in the Hall coefficient. The latter discrepancy could well be due to errors in calibration of the two different magnets used, but it is also possible that persistent photo-conductivity might play some role. The most likely explanation for the difference in resistance is that the thermal cycling to and from 300 K on moving the sample between cryostats results in a change of the impurity concentration in the quantum well. This is quite realistic: metallic

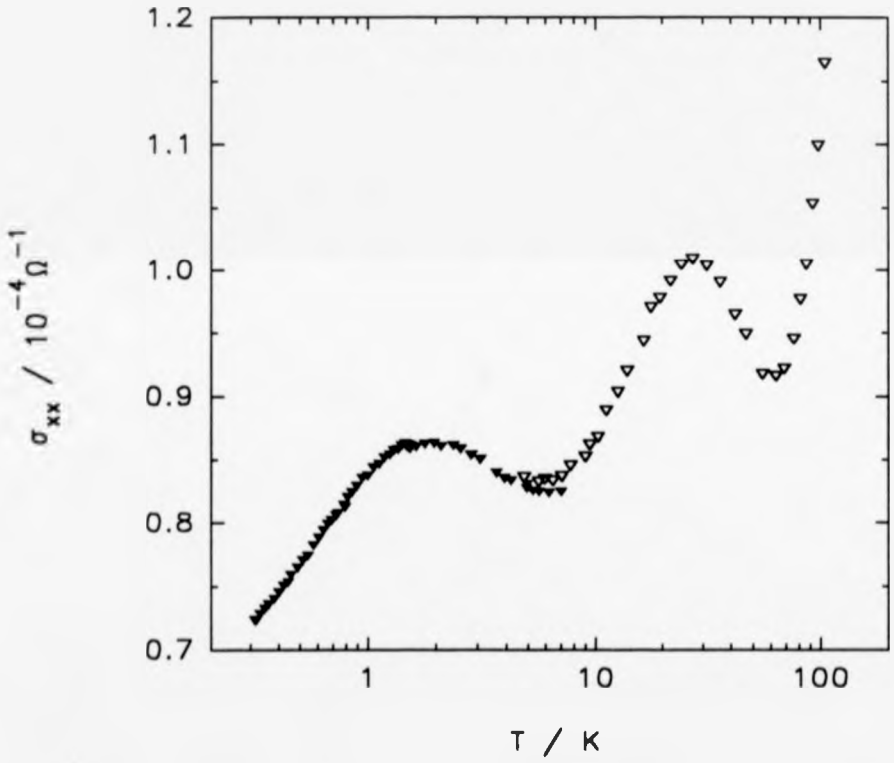

Fig. 4.24 Conductivity vs. temperature for 20/18 in the range (0.3-100) K (solid and open triangles represent data from different cryostats)

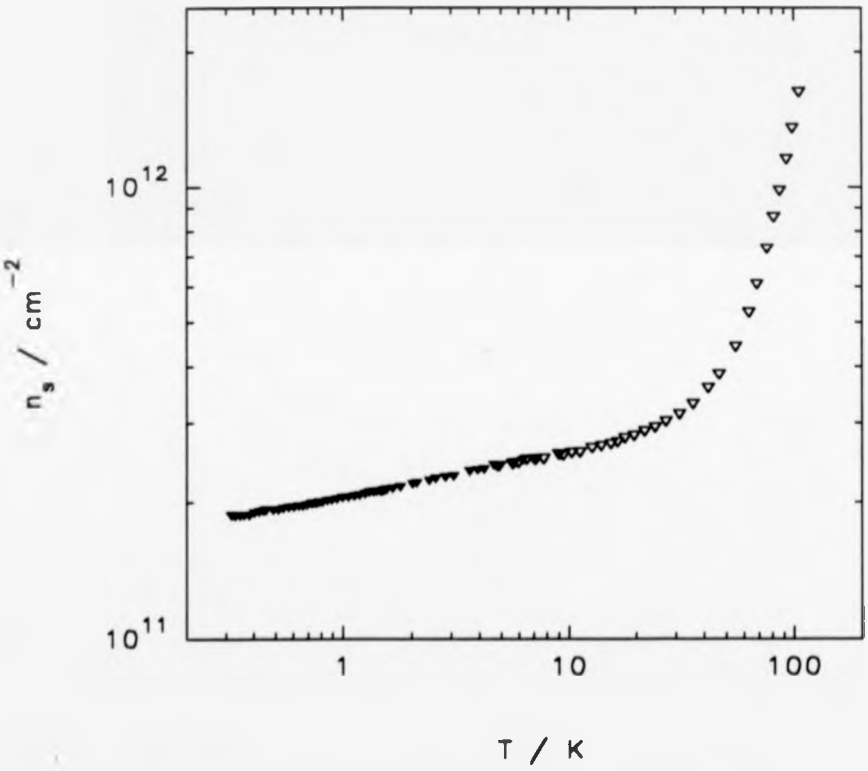

Fig. 4.25 Apparent hole density ($=1/eR_H$) vs. temperature for 20/18 in the range (0.3-100) K (solid and open triangles represent data from different cryostats)

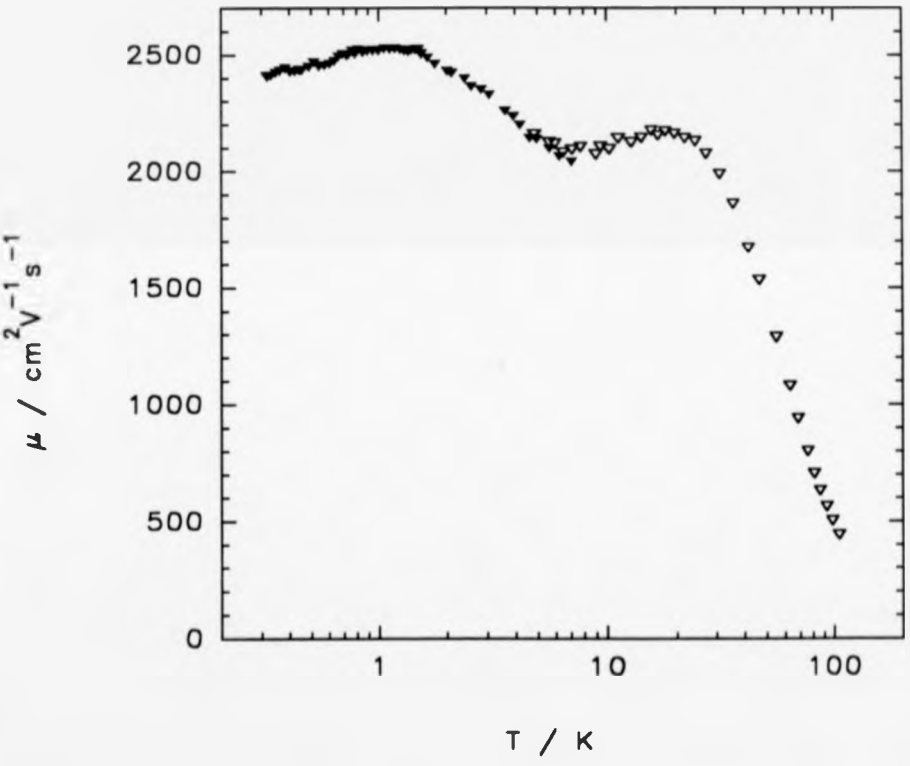

Fig. 4.26 Hole mobility vs. temperature for 20/18 in the range (0.3-100) K (solid and open triangles represent data from different cryostats)

impurities in the material are known to be fast diffusers, with Cu having a diffusion length, $\sqrt{Dt}$, of about $\frac{1}{10}$ mm for a period of 24 hours at room temperature (Hall and Racette, 1964), while the fact that the change in resistance is an increase concurs with the notion of the interface acting as a gettering site for mobile impurities.

4.3.3.2 SUMMARY OF THE PRINCIPAL CONDUCTION MECHANISMS IN THE REGION T=0.3-100 K

In the plot of the σ_{xx}-T data for sample 20/18 (Fig. 4.24), there are 5 different regions spanning the temperature range 0.3-100 K, each with distinctive behaviour. Identification of these at this stage, along with some explanation for the form of the conductivity, should aid the subsequent analysis for other samples, as well as pointing to the important and most interesting areas for study.

The temperature varying part of the resistance below ~ 1 K is dominated by weak localisation and enhanced hole-hole interaction effects arising from structural disorder in the samples. Direct evidence for this is provided by the lnT variation of the resistance (and Hall coefficient), which is also a signature of the two-dimensionality of the system. Between about 2 K and 5 K, the rise in resistance is caused by increasing thermal disorder in the 2DHG, with the result that holes are less able to screen one another from the prevalent scattering potentials (section 2.3.3). At higher temperatures still, the resistance decreases as the 2D gas departs from the degenerate limit and holes access vacant states above the Fermi energy: this is consistent with a Fermi temperature of 20 K, as appropriate to the hole density of 2.3×10^{11} cm^{-2}. Above 30 K, the increase in resistance is caused by lattice vibrations, with a significant increase of the phonon density and hence the frequency of hole-phonon interactions. This is very clearly seen in the

mobility-temperature plot (Fig. 4.26), where at 30 K the mobility commences an abrupt descent from a more or less constant low temperature value of ~ 2000 $cm^2V^{-1}s^{-1}$. Finally, above 60 K the resistance falls dramatically as the hole density in the sample increases with the onset of thermal activation of the large concentration ($\sim 10^{13}$ cm^{-2}) of undepleted B acceptors in the doping spike.

Complementary behaviour is observed in the variation of the Hall coefficient, R_H, with temperature, plotted as $(1/eR_H)=n_s$ against temperature in Fig. 4.25. At low temperatures, the lnT dependence of R_H is indicative of enhanced hole-hole interactions due to disorder in a 2D system and this is present up to temperatures of ~ 10 K. Thereafter, the decrease in R_H is much more rapid, becoming exponential in 1/T, as parallel conduction commences in the doping spike.

The aim of the research was to study the physical behaviour of holes in the quantum well formed at the heterojunction and therefore, having elected not to study phonon scattering, measurements were only taken below 20 K. In this temperature region, all the samples exhibit localisation, interaction and temperature dependent screening effects and have to some extent departed from the degenerate limit. In any case, the analytical expressions for degeneracy and screening corrections to the Boltzmann conductivity [(2.3.30) and (2.3.31) respectively] are derived in the limit $T << T_F$ and so a quantitative evaluation of data from the lowest density samples (20/18 and 54), for example, is not realistic at temperatures much above 10 K. Results for the temperature dependence of σ_{xx} are shown in Figs. 4.27-4.30, with the temperature dependences of the Hall coefficient for all 4 samples plotted on one set of axes (Fig. 4.31). The variation in transition temperature between the different regimes of conduction, as well as specific magnitudes of the localisation, interaction and screening parameters characterising ρ_{xx} and R_H in each sample, form the basis of a quantitative discussion of the results.

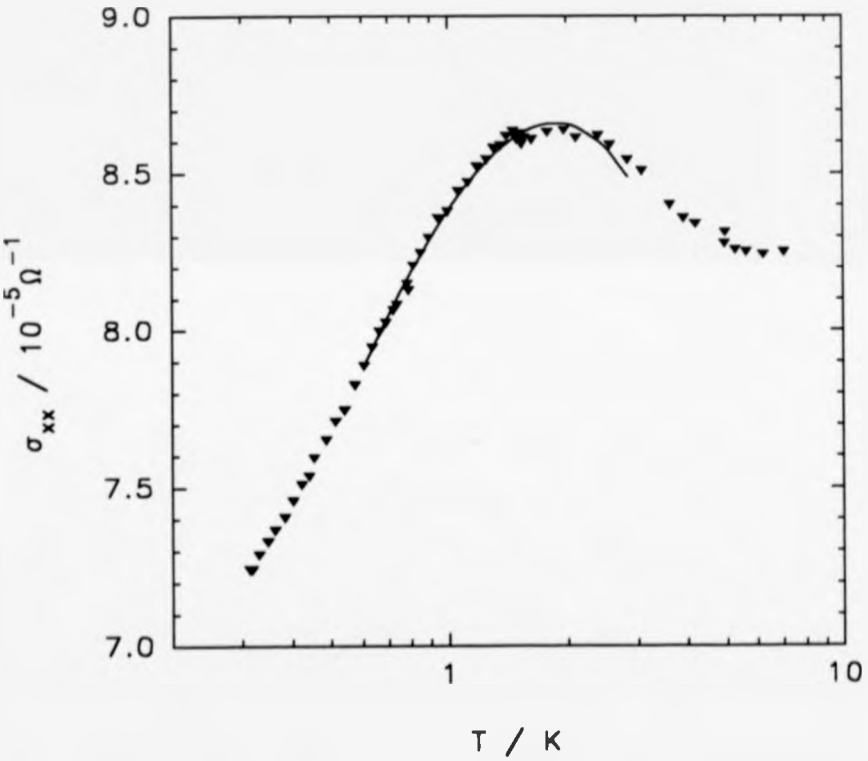

Fig. 4.27 Low temperature (0.3-8 K) conductivity for 20/18, plus a solid line fit across the conductivity peak

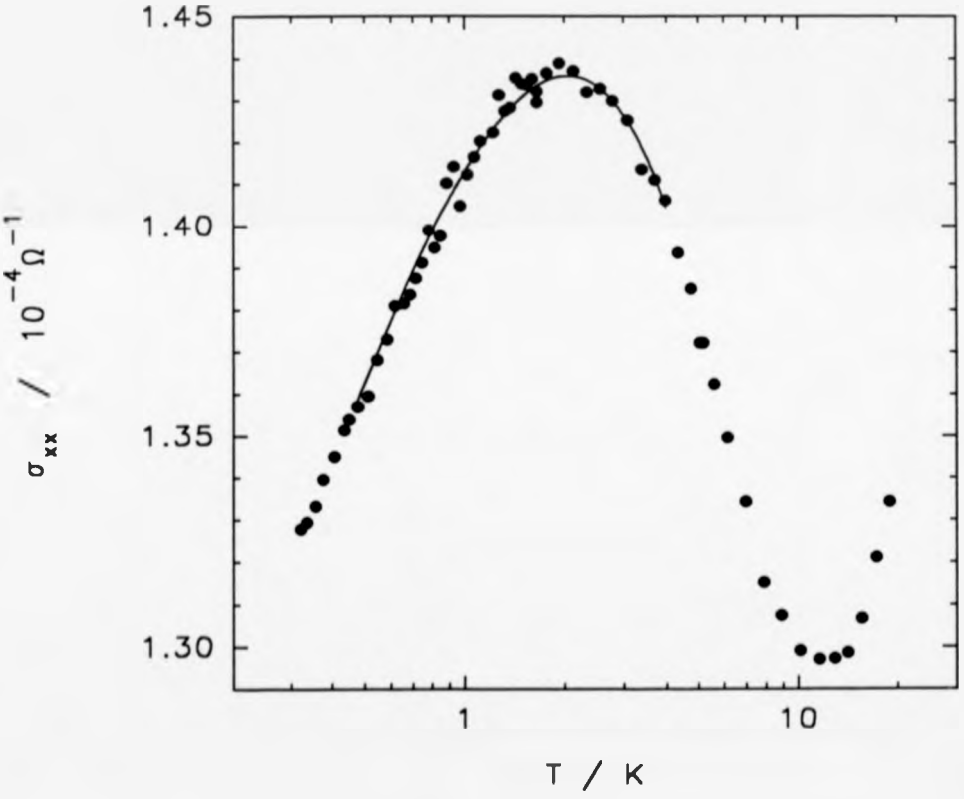

Fig. 4.28 Low temperature (0.3-20 K) conductivity for 20/44, plus a solid line fit across the conductivity peak

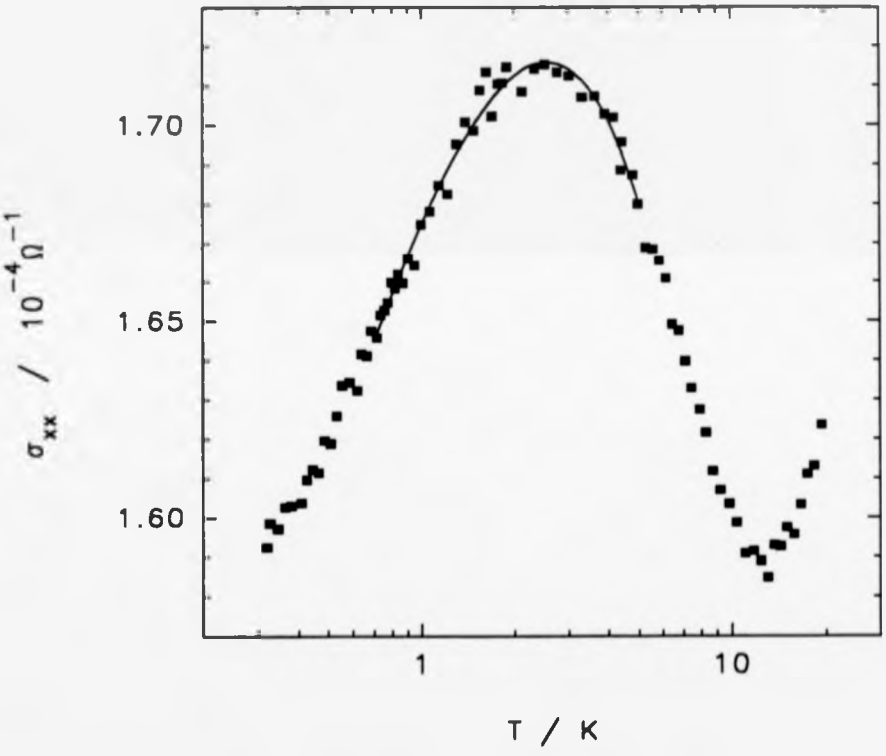

Fig. 4.29 Low temperature (0.3-20 K) conductivity for 20/46, plus a solid line fit across the conductivity peak

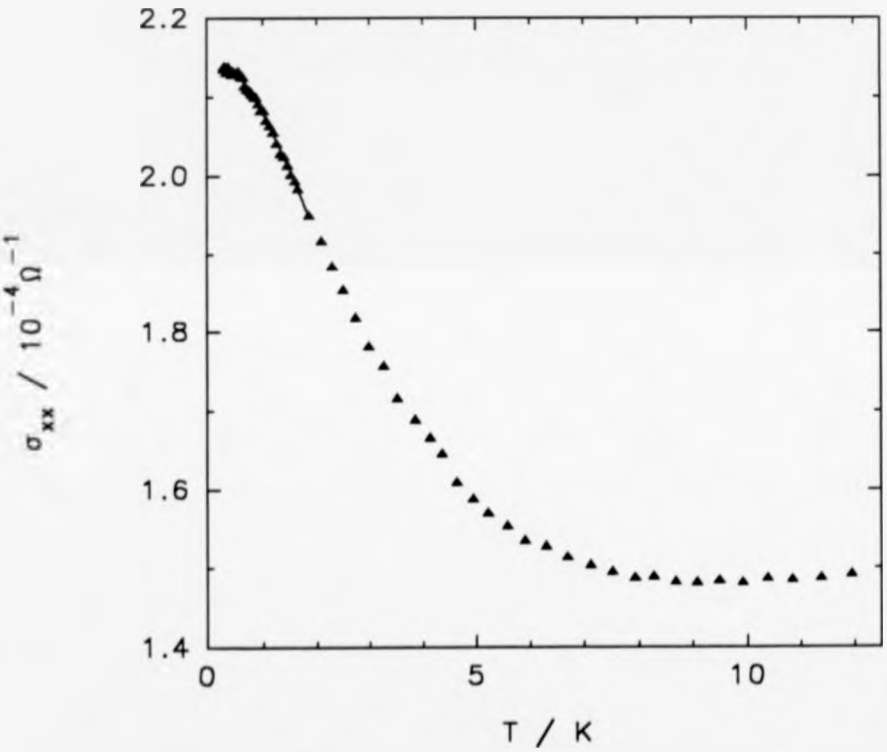

Fig. 4.30 Low temperature (0.3-12 K) conductivity for 20/54, plus a low temperature fit to the data

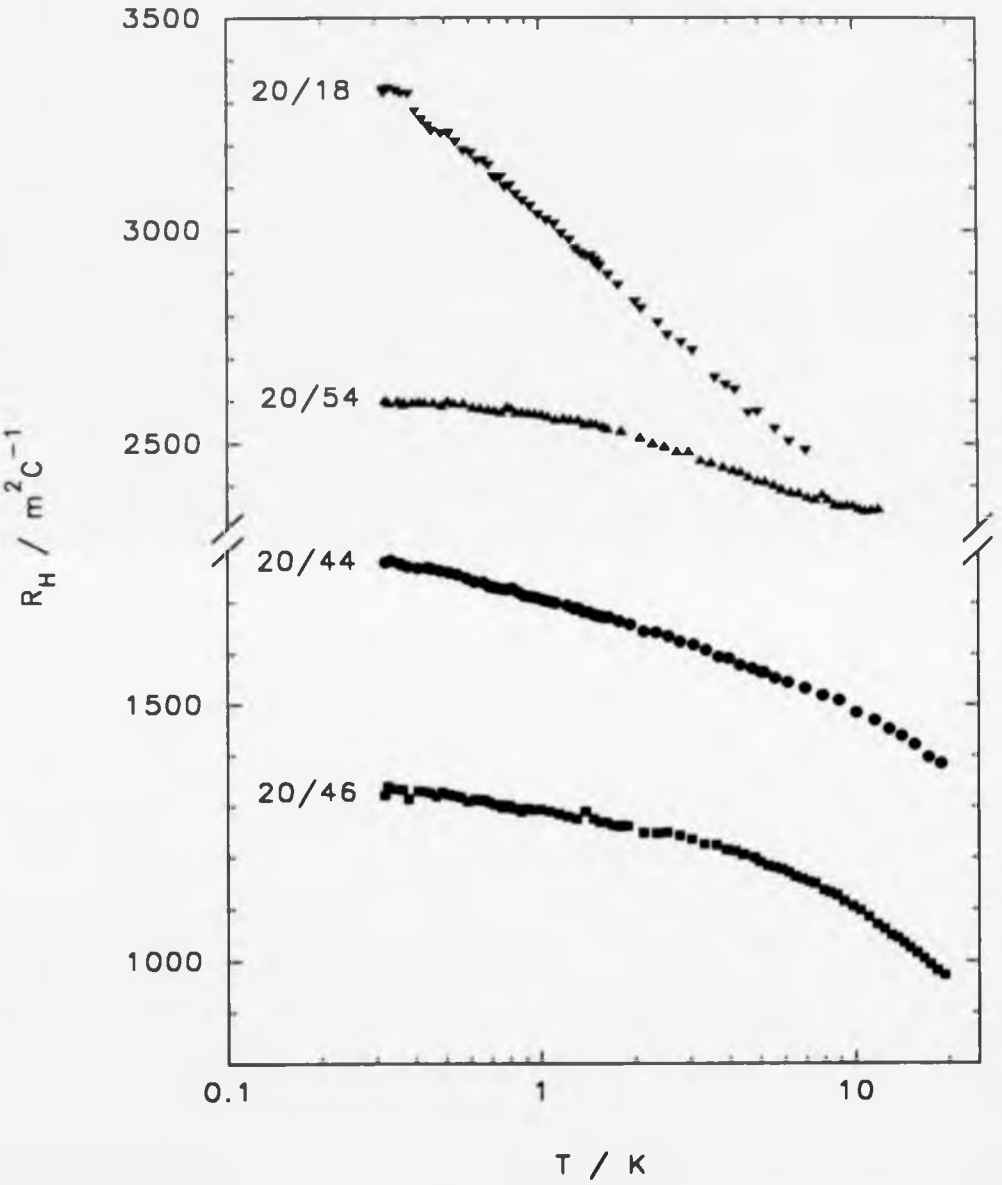

Fig. 4.31 Temperature dependence of the Hall coefficient in the range (0.3-20) K for samples 20/18, 44, 46 and 54

4.3.3.3 TEMPERATURE DEPENDENCE OF THE HALL COEFFICIENT

The principal feature of the data in most of the samples is a large, linear change of R_H with lnT, almost 25% per decade in the most disordered sample (20/18). However, it is also clear that the lnT variation is by no means universally present, with deviations occurring above 10 K and below about 2 K. The departure from a lnT dependence of R_H at high temperatures is due to the loss of phase coherence between interacting holes, which occurs once the de-phasing time, τ_φ, becomes similar to the time between elastic scattering events, τ. Taking the expression for τ_φ derived by Fukuyama (1984),

$$\tau_\varphi = \frac{2E_F\tau}{FkT} \Big/ \ln\left(\frac{4E_F\tau}{\hbar}\right) , \qquad (4.3.1)$$

then the temperature must satisfy

$$T \le \frac{2T_F}{F} \Big/ \ln\left(2\sqrt{2}\, k_F l\right) , \qquad (4.3.2)$$

in order that enhanced interaction effects are not destroyed. The disorder parameter $k_F l$ of a 2D system can be expressed in terms of the Boltzmann conductivity, σ, as

$$k_F l \approx \frac{\sigma}{\sqrt{2}}\left(\frac{h}{e^2}\right) . \qquad (4.3.3)$$

Using values of $k_F l$ deduced from (4.3.3) (see Table 4.5) then interaction effects should only be present well below about 30 K.

The departure of R_H from a lnT dependence at low temperatures is more surprising, as this was not observed in work on Si MOSFETs with similar mobilities (Uren *et al.*, 1981). The magnitude of the deviation seems to decrease as the value of $k_F l$ approaches unity. It is also notable that such effects are not present in the conductivity, at least on anything like the same scale. A number of physical phenomena might be thought to give

rise to such behaviour, but nearly all of them may be discounted, as follows.

i/ The application of a finite magnetic field necessary to generate a Hall voltage also results in changes to the conductivity, σ_{xx}, and resistivity, ρ_{xx}. Both **orbital and spin-splitting (Zeeman) effects** give rise to negative magnetoconductances (section 2.3.6.1), such that ρ_{xx} and ρ_{xy} increase in the presence of magnetic flux. However, the observed deviation of ρ_{xy} from 'ideal' lnT behaviour is negative and thus may not be understood in terms of either orbital or spin-dependent MR.

ii/ A second point to note is that while **fractional changes in ρ_{xx} and R_H are not small**, the calculation of $\Delta R_H/R_H$ has been carried out only to first order, with the assumption that $\Delta\sigma_{xx}/\sigma_{xx}$ and $\Delta\sigma_{xy}/\sigma_{xy}$ are both much less than unity. Taking the Taylor expansion for $\Delta\rho_{xy}/\rho_{xy}$ to second order in $\Delta\sigma_{xx}$ ($\Delta\sigma_{xy}\big|_{int.} = 0$ in any case), the correction to R_H is now

$$\left.\frac{\Delta R_H}{R_H}\right|_{int.} = -2\left(\frac{\Delta\sigma_{xx}}{\sigma_{xx}}\right) + 3\left(\frac{\Delta\sigma_{xx}}{\sigma_{xx}}\right)^2 . \qquad (4.3.4)$$

The inclusion of second order effects causes a deviation above the first order lnT ($\propto \Delta\sigma_{xx}$) dependence, with the effect becoming more pronounced at higher temperatures. This, however, does not provide an explanation for the form of the experimental data.

iii/ One conventional argument for this type of saturation in the measured resistance or Hall coefficient at low temperatures is that the 2D gas is not in thermal equilibrium with the crystal lattice and thus the Cu sample mounting block, to which the thermometers are thermally anchored. However, it was found that the use of electric fields less than 1 Vm^{-1} in strength did not give rise to **heating of the 2D gas** (section 3.2.6).

iv/ Recently, calculations of the correction to the Hall conductivity, σ_{xy}, due to localisation effects have been carried out for systems close to the metal-insulator transition ($k_F l \geq 1$). The result is (Wang *et al.*, 1992)

$$\left.\frac{\Delta\sigma_{xy}}{\sigma_{xy}}\right|_{loc.} = -\left(\frac{e^2}{2\pi^2\hbar}\right)\frac{1}{\sigma_{xx}}\left[1+\xi(k_F l)\right]\ln\left(\frac{L}{l}\right) \quad , \tag{4.3.5a}$$

where L is the smaller of the magnetic length, $l_c = (\hbar/eB)^{1/2}$, and the thermal dephasing length, $L_T = (\hbar D/kT)^{1/2}$, while for a system with parabolic bands the parameter $\xi(k_F l)$ is given by

$$\xi(k_F l) = 1 + \left(\frac{3}{4\pi}\right)\frac{\ln k_F l}{k_F l} \quad . \tag{4.3.5b}$$

In cases of weak disorder ($k_F l >> 1$), this expression for $\Delta\sigma_{xy}$ does infact reduce to give (2.3.49), the original expression for the weak localisation correction to the Hall conductivity derived in the same limit, but using perturbation theory, by Al'tshuler *et al.* (1980a).

A calculation of the weak localisation correction to the Hall coefficient using (2.3.34) and (4.3.5) now yields a non-zero result, which is

$$\left.\frac{\Delta R_H}{R_H}\right|_{loc.} = -\left(\frac{3}{4\pi^2}\right)\frac{\ln k_F l}{(k_F l)^2}\ln\left(\frac{L}{l}\right) \quad : \tag{4.3.6}$$

the implication is that $\Delta R_H|_{loc.}$ vanishes not only in the limit $k_F l >> 1$, but also as $k_F l$ approaches unity (from the conducting state), and that there exists a maximum value at $k_F l \sim 2$. The transition from thermal to magnetic length scale dominated behaviour occurs when the cyclotron length decreases below the inelastic thermal length; that is, at $l_c \sim L_T$, which for a 2D system may be written more explicitly as (see also section 2.3.7.2)

$$kT \approx (\mu_B B)(k_F l)\sqrt{2}\left(\frac{m^*}{m_o}\right)^{-1} \quad . \tag{4.3.7}$$

In the present samples, with B=0.12 T and $m^*=0.32m_o$, the crossover temperature, T_c, is given by $T_c = 0.36(k_F l)$ K. Both cases are now considered in detail:

a/ In the limit $L_T < l_c$, the localisation correction to the Hall coefficient is

$$\left.\frac{\Delta R_H}{R_H}\right|_{loc.} = -\frac{3}{4\pi^2}\left[\frac{\ln(k_F l)}{(k_F l)^2}\right]\left\{\ln\left(\frac{\hbar D}{k_B l^2}\right)^{1/2} - \tfrac{1}{2}\ln T\right\} \quad . \tag{4.3.8}$$

Given that the condition $l < L_T$ must be satisfied in order to establish the phase coherence necessary for weak localisation, then (4.3.8) predicts a reduction in R_H. The ratio of the localisation to interaction contributions to the gradient $\delta R_H/\delta \ln T$ is

$$\frac{\Delta R_H|_{loc.}}{\Delta R_H|_{int.}} = \left(\frac{3}{4\pi\sqrt{2}}\right)\frac{\ln k_F l}{k_F l}\left(1-\tfrac{3}{4}F^*\right)^{-1} \quad , \tag{4.3.8}$$

so that in these samples, with $F^* \sim 1$, the localisation correction is no more than about 10% of the interaction correction (exact values are contained in Table 4.4). The effect of weak localisation on the Hall coefficient is to cause the addition of a positive contribution to the negative gradient, $\delta R_H/\delta \ln T$; and, if not taken account of, will result in an overestimate of F^*.

b/ In the limit $L_T > l_c$, the change in the Hall coefficient due to localisation is

$$\left.\frac{\Delta R_H}{R_H}\right|_{loc.} = -\frac{3}{4\pi^2}\left[\frac{\ln(k_F l)}{(k_F l)^2}\right]\ln\left\{\left(\frac{\hbar}{eB}\right)^{1/2}\frac{1}{l}\right\} \quad . \tag{4.3.10}$$

The same value of magnetic field (0.12 T) is used in every Hall measurement on each sample, so a direct comparison between results for different samples is possible. The implication of (4.3.10) is that $\Delta R_H|_{loc.}$ should saturate to some constant value at low

temperatures: however, the interaction effect on ρ_{xy} is also present and thus no saturation should be apparent in the temperature dependence of the Hall coefficient.

Sample 20/54 has a value for T_c of (1.6±0.2) K, in good agreement with the theoretical estimate of 1.4 K, as deduced from (4.3.6). In sample 20/18, which has nearly the same carrier density as 20/54 but a much higher level of disorder, such that T_c is calculated to be 0.46 K, there is some hint of a change from a lnT dependence of R_H at $T \leq 0.5$ K; again, this is in good agreement with theory. However, in the other two higher density samples (20/44 and 46), the deviation from lnT behaviour occurs at much higher temperatures than expected (1-2 K). Nevertheless, the theory of Wang *et al.* (1992) does provide a possible explanation for the otherwise anomalous behaviour of the Hall coefficient at low temperatures, although many details remain to be explored.

The value of F* may now be extracted from the data. Two results are given for each sample: one taking no account of the localisation correction to the Hall coefficient, and a second estimate, which takes into account both interaction and localisation effects (see Table 4.4). Estimates of F* seem to be in rough agreement with theory, as displayed graphically in Fig. 2.10. The greater rate of change of R_H with T at higher temperatures for some samples (notably 20/44 and 20/46 - see Fig. 4.31) give anomalously small values for F*. The change in the value of F* by taking account of localisation effects in the analysis is seen to be negligible compared with errors and uncertainty in the measurements.

Sample	20/18	20/44	20/46	20/54
n_s / 10^{11} cm^{-2} (SdH)	(2.3±0.1)	(3.9±0.2)	(4.7±0.1)	(2.5±0.1)
R_H / m^2C^{-1}	(2710±120)	(1600±80)	(1330±30)	(2500±100)
$k_F l$	1.3 (±10%)	2.4 (±3%)	2.9 (±5%)	3.9 (±8%)
Temp. region used in calculation	(0.3→2) K	(3→8) K	(3.5→6.5) K	(2→7) K
$(\delta R_H/\delta \ln T)\|$ _____	-290.9..(±3%)	-93.8..(±5%)	-108.6..(±5%)	-111.2..(±3%)
F* (interaction only)	(0.92±0.16)	(0.92±0.12)	(0.63±0.08)	(0.82±0.12)
$(\delta R_H/\delta \ln T)\|_{loc.}$ (theoretical)	+15.98..	+9.239..	+6.397..	+8.500..
F* (loc. and int.)	0.90	0.88	0.59	0.78

Table 4.4 Values of the interaction parameter, F*, extracted from data for the temperature dependence of the Hall coefficient

4.3.3.4 TEMPERATURE DEPENDENCE OF THE CONDUCTIVITY

Although the transport coefficient measured in these experiments is ρ_{xx}, since the theoretical expressions are all written down in terms of changes to the conductivity, it is more convenient to work using the conductivity and make the conversion $\sigma_{xx} = \rho_{xx}^{-1}$ to the data at the outset.

A/ Maximal conductivity

The maximum in the conductivity is seen in 3 of the 4 samples and occurs at the same temperature, within experimental uncertainty, of 2.0 K. In the highest mobility sample (20/54), although a maximum is not directly observable, the data do indicate that $\partial\sigma/\partial T$ is tending towards zero as the lowest accessible temperature of 0.3 K is approached. The existence of a 'maximal conductivity' was predicted by Gold and Dolgopolov (1985) as a natural consequence of the interplay of screening in the Boltzmann term with localisation and interaction effects. Taking an expression for the total conductivity using (2.3.31), (2.3.36) and (2.3.42),

$$\sigma(T) = \sigma(0)\left[1 - C(\alpha)C(n_s)\left(\frac{T}{T_F}\right)\right] + \left(\frac{e^2}{2\pi^2\hbar}\right)\left[\alpha p + 1 - \tfrac{3}{4}F^*\right]\ln\left(\frac{kT\tau}{\hbar}\right) , \qquad (4.3.11)$$

the temperature, T_m, at the maximum is

$$T_m = \frac{T_F}{\sigma(0)C(\alpha)C(n_s)}\left(\frac{e^2}{2\pi^2\hbar}\right)\left[\alpha p + 1 - \tfrac{3}{4}F^*\right] . \qquad (4.3.12)$$

Writing $\sigma(0) = n_s e^2 \tau(E_F)/m^*$ and noting that T_F is proportional to n_s in a 2D system, then in (4.3.12) there remains only a relatively weak dependence of T_m on carrier density, because $C(n_s)$ and F^* vary slowly with n_s (see Figs. 2.7 and 2.10 respectively). The only significant variable in (4.3.12) is $\tau(E_F)$, so that the value of T_m should correspond roughly with the mobility. In this way, by comparing the hole mobility with that of 20/18, the most closely matched sample in terms of carrier density, the predicted maximum conductivity in the higher mobility sample (20/54) should occur around 0.6 K. This value is something of an overestimate (by a factor of two), but the observed trend is nevertheless in accord with theory.

The corresponding resistance minimum has been observed previously by Uren *et al.* (1981) in a Si MOSFET with a mobility of ~ 1600 cm^{2}V^{-1}s^{-1} at $T \sim 1$ K, which is

reasonably consistent with the present author's results. In addition, Uren *et al.* applied a weak magnetic field perpendicular to the sample and, in a number of stages, reduced the weak localisation correction in the conductivity to the point of quenching it. It is possible to explain the reduction of T_m with increasing B apparent in data (Fig. 4.32) to the vanishing of the localisation parameter, α, so that according to (4.3.12) there should be a corresponding reduction in the value of T_m.

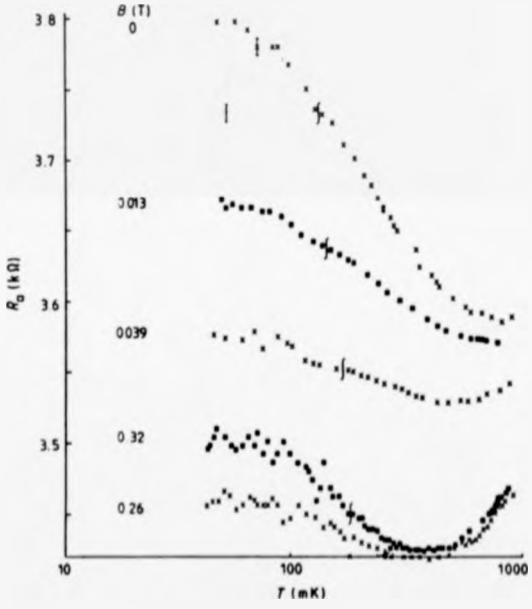

Fig. 4.32 Temperature dependence of the conductivity for a 2DEG in a Si MOSFET with a weak perpendicular magnetic field (from Uren *et al.*, 1981)

In the experiments of Uren *et al.* (1981), a dilution refrigerator was used which enabled measurements to be made in the temperature range 0.05→1 K. The maximal conductivity therefore occurs at the upper end of the region of accessible temperature and

so the data may be explained solely in terms of interaction and localisation effects with little loss of accuracy. In the present work, the value of T_m ($\sim$2 K) for 3 of the 4 samples lies, logarithmically, at the midpoint of the studied temperature region, so that in a quantitative analysis of the results, it is essential to fit the total conductivity expression (4.3.11) to the data. This has been done using the commercially available software 'Sigmaplot 5.00' (Jandel Scientific). In the analysis of each set of data, a temperature region is chosen for the fitting, which is bounded at the lower end by any departure from a clear lnT dependence of σ_{xx} and at the upper end by the lifting of degeneracy in the 2D gas, as indicated by the departure from a $\Delta\sigma_{xx} \propto T$ relationship (sometimes no such behaviour is observed and this transition temperature is seen only as a point of inflexion in the data). Independent parameters in the fitting are $\sigma(0)$, αp and $C_1 = C(\alpha)C(n_s)$, with T_F and F^* fixed using values previously determined. The results are contained in Table 4.5: in addition to the total conductivity fitting values, at the foot of the table are estimates of $\sigma(0)$, αp and C_1 obtained by assuming that variation of the conductivity in regions above and below the maximal temperature is dominated, respectively, by the screening part of the Boltzmann conductivity and the effects of localisation and interaction.

B/ Transition to non-degenerate conduction

The departure from degeneracy is seen in all the samples as a minimum in the conductivity, between 6 and 13 K. The characteristic temperature for this transition may be obtained by minimising the conductivity which is a sum of the two temperature dependent Boltzmann terms, (2.3.31) and (2.3.32): the result is

$$T_{dg} = \left[\frac{3C_1}{\pi^2\gamma(\gamma+1)}\right]T_F \quad , \qquad (T_{dg} << T_F) \, . \qquad (4.3.13)$$

Experimental measurements of T_{dg} and theoretical estimates are contained in Table 4.5. The theoretical values are about 50% too low for $n_s=2.5\times10^{11}$ cm^{-2} (20/18), with the discrepancy rising to 100% for sample 20/46, for which $n_s=4.7\times10^{11}$ cm^{-2}. It may be that the theory for the correction to the Boltzmann conductivity derived assuming strictly degenerate conditions is not valid, although it should be pointed out that the discrepancy appears to be largest in the sample which most closely satisfies the degeneracy criterion.

C/ Temperature variation due to screening in the Boltzmann conductivity

Considering the results of the total conductivity fitting procedure first of all, very close agreement between experiment and theory (Gold and Dolgopolov, 1986) is obtained for the value of C_1, assuming that the origin of the dominant scattering potential is charged interface impurities, rather than interface roughness. Only in the high mobility sample (20/54) is there some discrepancy (-20% difference), but this is probably because there is no data at temperatures below T_m (-0.3 K), even though localisation and interaction effects are present (they are seen in the variation of the Hall coefficient with temperature - Fig. 4.31) and are included in the fitting proceedure. On the other hand, a direct fit to the data of 20/54 in the temperature range 1.5-3 K, using only the screened Boltzmann conductivity (2.3.31), for which a linear T-dependence of $\Delta\sigma_{xx}$ exists, yields a value for C_1 of (1.50±0.11), in good agreement with the theoretical value of 1.46. In the case of the 3 lower mobility samples, the values of C_1 obtained via the total conductivity fitting proceedure are in very good agreement with theory, but attempts

to measure C_1 directly from the data plots yield values about $\frac{1}{4}$ of those expected theoretically and obtained through the total conductivity fitting proceedure. The problem with a direct estimation of C_1 in these cases is that the region of temperature in which the screened Boltzmann term is the dominant temperature dependent effect is narrow, bounded at the upper end by a transition to non-degenerate transport and in the lower limit by the prevalence of localisation and interaction effects. It is therefore not surprising that, even in the high mobility sample, there is no evidence of the $(T/T_F)^{3/2}$ term predicted by Gold and Dolgopolov (1985 and 1986), given that the prefactor for this term in σ_{xx} is about an order of magnitude smaller than $C(\alpha)C(n_s)$, the prefactor to the linear, T/T_F, term.

What is required for a detailed study of the temperature dependence of screening in the Boltzmann conductivity, with specific reference to the predictions of Gold and Dolgopolov (1986), are samples with much higher carrier densities, so that the upper limit of the relevant temperature region is increased due to a larger Fermi temperature. In addition, higher carrier mobilities would be desirable, so that the dominance of localisation and interaction effects in the temperature varying conductivity is restricted to lower temperatures.

Infact, such studies have been performed using n-channel MOSFETs, with electron mobilities of (1.5-2) $m^2V^{-1}s^{-1}$, and carrier densities in the range $(4\text{-}15)\times10^{11}$ cm^{-2} (Vyrodov *et al.*, 1988). The results of this work show essentially a linear temperature dependence of $\Delta\sigma_{xx}$ (Fig. 4.33), but it is possible to fit the conductivity expression which includes the $(T/T_F)^{3/2}$ term, (2.3.31), to the data. At the lowest temperatures (≤1-2 K), some deviation below the theoretically predicted conductivity is evident. Vyrodov *et al.* (1988) draw attention to the fact that lifetime broadening of the energy states can become important at low temperatures, once it exceeds the thermal broadening: in such cases, the

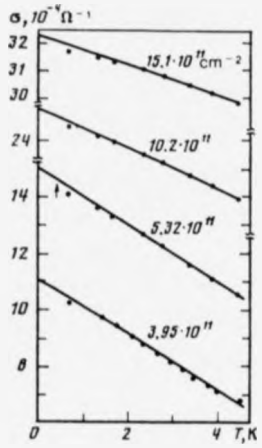

Fig. 4.33 Temperature dependence of the conductivity of a 2DEG in a high mobility Si MOSFET (from Vyrodov *et al.*, 1988)

$2k_F$ singularity in the dielectric function, $\varepsilon(q)$, is partially smeared out and the temperature dependence of the conductivity given by (2.3.31) weakened accordingly.

Writing this condition as $kT \leq \Gamma$, with $\Gamma = \hbar/\tau$ and $\mu = e\tau/m^*$, it follows that in the author's Si/SiGe 2DHG samples, broadening effects should be important in the temperature region $T \leq 4/(\mu/m^2V^{-1}s^{-1})$. This implies that for $\mu \sim 2000$ $cm^2V^{-1}s^{-1}$, as is the case for the three low mobility samples (20/18,44 and 46), the linear temperature dependence of the conductivity predicted by Gold and Dolgopolov (1986) should be partially destroyed at temperatures below 20 K. This, however, is in contradiction with the experimental results, which show that linear temperature dependences are present down to $T \sim 2$ K. In the higher mobility sample (20/54), which has a mobility of ~ 5000 $cm^2V^{-1}s^{-1}$ at $T = 1$ K, the linear temperature dependence is present down to 1.5 K, in contradiction with a predicted minimum temperature for the observation of such effects of 7 K.

The theoretical transition temperatures are roughly one order of magnitude larger than those suggested by the author's measurements. If level broadening effects are significant at temperatures lower than T_m, such that they are obscured by localisation and interaction effects, then the effect on the values of parameters deduced from the total-conductivity fit will be minimal, and taking no account of level broadening will result only in a small overestimate of the localisation parameter, αp.

Vyrodov *et al.* (1988) also mention that the departure from the expected screening related behaviour of the Boltzmann conductivity at low temperatures is of the correct magnitude to be attributable to the onset of localisation and interaction effects; and furthermore, they are able to induce an apparent increase in C_1 with the application of a 0.06 T magnetic field, consistent with the quenching of weak localisation in a sample with a carrier mobility of 2 $m^2V^{-1}s^{-1}$. However, a comparison of these results, for which the linear T-dependence holds only above 1-2 K, with those for the author's highest mobility sample ($\mu \sim 0.5$ $m^2V^{-1}s^{-1}$), where a linear temperature dependence persists down to 1.5 K, suggests that the notion of localisation and interaction effects being responsible for the observed departure from linearity in the results of Vyrodov *et al.* (1988) is not realistic (a maximal conductivity of 0.1 K is predicted for this sample). On the other hand, a quantitative estimate of the temperature at which level broadening effects become important in Vyrodov's material does appear to give good agreement with experiment, which is not the case with the author's results. It is interesting to note that in the results of Vyrodov *et al.* (1988) (Fig. 4.33), while the approximately linear temperature dependence of the conductivity is valid across a wide temperature region in gases with high carrier densities, it is possible to see that the region of validity is restricted to a rather narrow temperature range of 1.5→4 K for the low density gas ($n_s = 4\times10^{11}$ cm^{-2}), which is exactly the problem encountered by the author.

Smith and Stiles (1986) also made measurements on MOSFET 2DEGs with

mobilities of 1-2 $m^2V^{-1}s^{-1}$ in the temperature range 0.2-20 K. The results are basically similar to those of Vyrodov *et al.* (1988): however, because data points are not shown, only fits to the data plus a few error bars, no discussion of their results is offered.

D/ Results for the weak localisation and interaction regimes

Values of the localisation parameter, αp, and the zero-temperature conductivity, $\sigma(0)$, are collected alongside other sample parameters in Table 4.5. The measured value of αp differs from unity in all but the most disordered sample, 20/18, with an apparent decrease with increasing sheet density. In the high mobility sample (20/54), the value for αp is smaller still. In the absence of spin-orbit and spin-spin scattering, α should have a value of unity (Hikami *et al.*, 1980), while for 2D disordered systems, $p=1$ (Lee and Ramakrishnan, 1985). It has previously been argued from a theoretical perspective (section 2.2), and confirmed experimentally by low field MR measurements (section 4.3.2.1), that in this strained system spin-orbit scattering is suppressed. The possibility that significant spin-spin scattering is present in the author's samples is conceivable, given that a large concentration of magnetic scattering centres is present due to metallic contamination of the epi-layers. In the limit of dominant spin-spin scattering, $\alpha = 0$ (Hikami *et al.*, 1980), so the deviation of α below unity may be due to the presence of magnetic centres.

Attempts at fitting an expression for the weak localisation correction to the conductivity, (2.3.36) and (2.3.42), to the low temperature data ($T < T_m$) yielded rather different values of αp from those obtained through the total-conductivity fitting proceedure. The values of αp are all much lower, approaching zero in the higher density sample (20/46). Given that the fitting of the total conductivity expression (4.3.11) to the

data was found to give a much more satisfactory agreement with theory in the region where the temperature-varying part of the conductivity is dominated by the screened Boltzmann term, it is assumed that the 'total' fitting proceedure is necessary and values obtained from fitting only to the data below T_m using (2.3.36) and (2.3.42) are taken to be unphysical.

Adopting the viewpoint that, if spin dependent scattering effects are absent from the material, αp should be exactly equal to one in all the samples, then allowing the interaction parameter, F*, to vary in order to obtain a fit of (4.3.10) to the data merely results in anomalously small values of F*, such that discrepancies now arise between the observed temperature dependences of the Hall coefficient and these new values for F*.

Having discounted both spin-orbit and spin-spin scattering as conceivable explanations for the apparent departure of α from unity, there remains one other, more fundamental explanation for this behaviour. As in the R_H-T data, the fractional change of σ_{xx} with temperature is large ($\sim 25\%$ per decade in sample 20/18) and it may be that the experimental results cannot readily be compared with the theoretical expression for $\Delta \sigma_{xx}$, derived using perturbation theory in the limit of weak disorder ($k_F l >> 1$) (Abrahams *et al.*, 1979). Further insight might be achieved through a re-calculation of $\Delta\sigma_{xx}|_{loc}$ in the limit $k_F l \geq 1$ relevant to these experiments, to complement the work done on the localisation correction to the Hall conductivity, $\Delta\sigma_{xy}|_{loc}$, by Wang *et al.* (1992) [see section 4.3.3.3].

Sample	20/18	20/44	20/46	20/54
μ / $cm^2V^{-1}s^{-1}$	2000	2100	2000	3750
n_s / 10^{11} cm^{-2}	2.3 (±0.1)	3.9 (±0.2)	4.7 (±0.1)	2.5 (±0.1)
$R_{0.3\,K}$ / kΩ	13.8	7.5	6.3	4.7
$k_F l$	1.3	2.4	2.9	3.9
T_F / K	20 (±1)	34 (±2)	41 (±1)	22 (±1)
τ_φ / s	3.4×10^{-11}	4.2×10^{-11}	7.1×10^{-11}	6.2×10^{-11}
τ / s	3.5×10^{-13}	3.8×10^{-13}	3.8×10^{-13}	9.7×10^{-13}
l / nm	11	15	17	31
l_φ / nm	110	160	230	250
F*	0.92 (±0.16)	0.92 (±0.12)	0.63 (±0.08)	0.82 (±0.12)
$T_{max.\ cond}$ / K	2.0 (±0.2)	1.8 (±0.2)	2.2 (±0.2)	−0.3
$T_{min.\ cond}$ / K	6.0 (±0.1)	11.5 (±0.5)	12.5 (±0.5)	9.5 (±0.5)
$T_{min.}$ / K (theory)	4.6	6.5	7.2	4.9
αp	0.98 (±0.10)	0.60 (±0.09)	0.49 (±0.08)	0.23 (±0.04)
$\sigma(0)$	9.2×10^{-5}	1.47×10^{-4}	1.72×10^{-4}	2.29×10^{-4}
$C_1 = C(\alpha)C(n_s)$	1.78 (±0.2)	1.27 (±0.03)	1.25 (±0.07)	2.00 (±0.05)
$C(n_s)$ (theory)	0.54	0.45	0.42	0.53
C_1 (theory)	1.50	1.25	1.16	1.46
αp *	0.55 (±0.11)	0.32 (±0.06)	0.07 (±0.01)	--------
$\sigma(0)$ *	$(9.05\pm0.05)\times10^{-5}$	$(1.50\pm0.005)\times10^{-4}$	$(1.78\pm0.01)\times10^{-4}$	$(2.22\pm0.01)\times10^{-4}$
C_1 *	0.36 (±0.05)	0.55 (±0.05)	0.44 (±0.04)	1.50 (±0.11)

Table 4.5 This contains estimates of localisation and Boltzmann conductivity parameters extracted from plots of the low temperature σ_{xx}-T data (values for parameters at the foot of the table marked with an asterisk are obtained by direct fitting of (2.3.31) and (2.3.36)+(2.3.42), respectively to data above and below $T_{max.}$).

CHAPTER FIVE

CONCLUSIONS AND SUGGESTIONS FOR FURTHER WORK

Electrical properties of 2DHGs in strained SiGe layers have been studied in this thesis. In all cases, remote doping of SiGe layers by placing B atoms a little distance from the Si/SiGe heterointerface in the adjacent Si (potential barrier) regions, gives rise to well defined 2DHGs in the SiGe, with an absence of significant parallel conduction channels below 20 K.

The temperature dependence of resistance for the first set of samples showed that conduction of charge was between strongly localised states. It is suggested that this was caused by metallic impurity contamination of the layers during the growth, giving rise to distortion of the lattice at the interface, which along with charged impurities would be capable of inducing strong localisation of holes. The introduction of a growth interrupt in the Si, about 10 nm from the heterointerface, was found to change the nature of the conduction process profoundly, due to de-localisation of hole states. The role of the interrupt is thought to be as a gettering site for diffusing impurities, such that in this case the concentration of impurities in the well is reduced below a critical concentration for a insulator-metal transition and which results in a finite low temperature mobility of $\sim 450\ cm^2V^{-1}s^{-1}$. Insertion of the Ge source in a Si liner reduced Cu contamination of the layers and was accompanied by a four-fold increase in mobility to $\sim 2000\ cm^2V^{-1}s^{-1}$. Increasing the growth temperature from 550 °C to 640 °C resulted in an increase of 4 K mobility to $\sim 3700\ cm^2V^{-1}s^{-1}$, which was attributed to solid state diffusion of impurities out of the quantum well. A sample set with different spacer thicknesses was then grown, to provide a range of 2DHG densities, suitable for further electrical investigations.

The dependence of QW hole density on spacer thickness and other structural and doping parameters was modelled by the author, with good agreement between experiment and theory obtained for a depletion charge density of $N_{Depl} \sim 1\times10^{11}$ cm^{-2} and density of charged interface states, n_i, equal to 2×10^{11} cm^{-2} . In addition, the hole mobility has been calculated using available theories incorporating minor adjustments for all the likely low temperature scattering mechanisms: alloy potential fluctuations, remote ionised impurities, interface roughness and interface impurities. Comparison of experimental data with theory shows that only interface impurity scattering with $n_i \sim 2\times10^{11}$ cm^{-2} is capable of accounting for the observed magnitude of the mobility. While this value might seem large, it is consistent with the dependence of hole density on spacer thickness and also with the results of CV profiling (Brighten *et al.*, 1992). It is notable that alloy and interface roughness scattering are unable to account for the experimental data; with a large reduction of material contamination necessary before such scattering processes make a significant contribution to the electrical resistance.

Magnetotransport experiments were carried out in fields up to 12 T in strength and at temperatures down to 0.3 K. The form of the low field MR is due to the suppression of weak localisation, and the fact that the sign of the MR is negative confirms that the degeneracy of light and heavy holes is absent in these strained systems. Above 0.5 T, the positive MR is attributed to Zeeman splitting of interacting holes. Parallel field MR measurements provide confirmation that the hole gas has a finite thickness ($\sim$5 nm) and also that the g-factor is highly anisotropic. High perpendicular field MR measurements exhibit Shubnikov-de Haas oscillations above 1 T (at T$\sim$0.3 K) and quantum Hall plateaux at higher fields. The existence of odd and even filling factor plateaux indicates that the quantum well $|J,M_J\rangle$ eigenstates have their $\pm M_J$ spin degeneracy lifted: it is also possible to see a doublet spin structure in the highest magnetic field MR peak in some of the samples, in the form of a broad shoulder. Assigning filling factors to the MR peaks enables the hole densities to be estimated.

The temperature varying part of the conductivity shows a number of different physical effects: at the lowest temperatures, weak localisation and enhanced hole-hole interaction effects dominate, but above ~ 2 K thermal disorder reduces the screening efficiency and causes a decrease in magnitude of the dominant Boltzmann term. The temperature dependence of the conductivity resulting from the interplay of these two effects gives quite a good agreement with available theories. The onset of non-degenerate effects occurs above about 10 K. The Hall coefficient exhibits the lnT temperature dependence characteristic of interaction effects up to 10 K, but with a small deviation at the lowest temperatures. A promising explanation is given for this, based on a recent calculation of the Hall conductivity for systems near the metal insulator transition, as appropriate to the samples studied in this work. The fact that theories of weak localisation and electron-electron interaction effects derived using perturbation theory (assuming disorder is weak) are able to account for the form and magnitude of the effects seen in this work is noteworthy. This is one area which might benefit from further theoretical investigation.

A number of possible experiments are now mentioned, some of which have already been commenced by other members of the Warwick group. Measurements of the MR as a function of temperature and also in tilted magnetic fields could be used to resolve the spin-splitting structure in the material. In connection with this, it would be useful to have available results of calculations of the Landau level structure for this strained system. Cyclotron resonance measurements are underway as part of a collaboration with the Clarendon Laboratory, University of Oxford.

Further investigations of the growth temperature dependence of transport coefficients are being made at Warwick and it is also proposed to use gated Hall bar structures, in order to test the 'temperature dependence of conductivity' theory of Gold and Dolgopolov (1986); these samples would enable the variation of carrier density with a constant scattering potential, with its strength changed only by screening. It would also be very useful to test further the theory of Wang *et al.* (1992) for the

localisation correction to the Hall conductivity, by making Hall and resistance measurements as a function of temperature **and** magnetic field. Some interesting experiments would be possible in 2DHG samples grown on relaxed buffer layers with different compositions. It might be possible to correlate changes in the low field MR with variation in separation of the light and heavy hole energy states. Finally some useful investigations of hopping conduction could be performed with the gated Hall bar structures, by reducing the QW hole density below a critical metal-insulator transition and measuring resistance as a function of temperature.

References

Abrahams, E., Anderson, P.W., Licciardello, D.C. and Ramakrishnan, T.V., Phys. Rev. Lett. (1979), 42, 673

Abstreiter, G., Brugger, H., Wolf, T., Jorke, H. and Herzog, H.-J., Phys. Rev. Lett. (1985), 54, 2441

Airaksinen, V.M., Harris, J.J., Lacklison, D.E., Beall, R.B., Hilton, D., Foxon, C.T. and Battersby, J., J. Vac. Sci. Technol. B (1988), 6, 1151

Al'tshuler, B.L., Khmel'nitskii, D., Larkin, A.I. and Lee, P.A., Phys. Rev. B (1980a), 22, 5142

Al'tshuler, B.L., Aronov, A.G. and Lee, P.A., Phys. Rev. Lett. (1980b), 44, 1288

Al'tshuler, B.L., Aronov, A.G., Larkin, A.I. and Khmel'nitskii, D.E., Sov. Phys. JETP (1981), 54, 411

Al'tshuler, B.L. and Aronov, A.G., JETP Lett. (1981), 33, 499

Al'tshuler, B.L. and Aronov, A.G. in "Electron-Electron Interactions in Disordered Systems", (1985), ed. Efros, A.L. and Pollak, M., Elsevier Science Publishers (Amsterdam)

Anderson, D.A., Bass, S.J., Kane, M.J. and Taylor, L.L., Appl. Phys. Lett. (1986), 49, 1360

Ando, T., Fowler, A.B. and Stern, F., Rev. Mod. Phys. (1982), 54, 437

Ashcroft, N.W. and Mermin, N.D.: "Solid State Physics", (1976), HRW International

Barlow, R.D. and Dowsett, M.G., Private communication (1992)

Bastard, G., Appl. Phys. Lett. (1983), 43, 591

Bastard, G.: "Wave Mechanics applied to Semiconductor Heterostructures", (1988), Les Editions de Physique (Les Ulis)

Bergmann, G., Phys. Rev. Lett. (1982a), 49, 162

Bergmann, G., Sol. St. Comm. (1982b), 42, 815

Bergmann, G., Phys. Rev. B (1983), 28, 2914

Bergmann, G., Phys. Reports (1984), 107, 1

Bishop, D.J., Tsui, D.C. and Dynes, R.C., Phys. Rev. Lett. (1980), 44, 1153

Biswas, R.G., (1992), PhD Thesis, University of Warwick

Blakemore, J.S.: "Solid State Physics", (1985), Cambridge

Brighten, J.C., Kubiak, R.A., Phillips, P.J., Whall, T.E., Parker, E.H.C., Hawkins, I.D. and Peaker, A.R., Thin Solid Films (1992), 222, 116

Bube, R.H.: "Electronic Properties of Crystalline Solids", (1974), Academic Press (New York)

Burdis, M.S. and Dean, C.C., Phys. Rev. B (1988), 38, 3269

Butcher, P.N., in "Crystalline Semiconducting Materials and Devices" (1986), ed. Butcher, P.N., March, N.H. and Tosi, M., Plenum (New York)

Cham, K.M. and Wheeler, R.G., Phys. Rev. Lett. (1980), 44, 1472

Chattopadhyay, D., Sutradhar, S.K. and Nag, B.R., J. Phys. C: Solid State Phys. (1981), 14, 891

Clark, R.G. and Maksym, P.A., Physics World (1989), (Sept.), 39

Dai, P., Zhang, Y. and Sarachik, M.P., Phys. Rev. B (1992), 45, 3984; *ibid.* 46,6724

Dämbkes, H., Herzog, H.-J., Jorke, H., Kibbel, H. and Kasper, E., IEEE Trans. Electr. Dev. (1986), 33, 633

Dingle, R., Störmer, H.L., Gossard, A.C. and Wiegmann, W., Appl. Phys. Lett. (1978), 33, 665

Dodson , B.W., Appl. Phys. Lett. (1988), 53, 394

Dodson, B.W. and Tsao, J.Y., Appl. Phys. Lett. (1987), 51, 1325

Dolan, G.J. and Osheroff, D.D., Phys. Rev. Lett. (1979), 43, 721

Ebert, G., von Klitzling, K., Probst, C., Schuberth, E., Ploog, K. and Weimann, G., Solid State Comm. (1983), 45, 625

Ekenberg, U., Batty, W. and O'Reilly, E.P., Journal de Physique C (1987), 5, 553

Emeleus, C.J., Whall, T.E., Smith, D.W., Kubiak, R.A., Parker, E.H.C. and Kearney, M.J., Thin Solid Films (1992), 222, 24

Emeleus, C.J., Whall, T.E., Smith, D.W., Kubiak, R.A., Parker, E.H.C. and Kearney, M.J., J. Appl. Phys. (1993), 73, (to appear)

Emeleus, C.J., Whall, T.E., Smith, D.W., Mattey, N.L., Kubiak, R.A., Parker, E.H.C. and Kearney, M.J., Phys. Rev. B (1993), 47 (to appear)

Fang, F.F. and Howard, W.E., Phys. Rev. Lett. (1966), 16, 797

Fang, F.F., Wang, P.J., Meyerson, B.S., Nocera, J.J. and Ismail, K.E., Surf. Sci. (1992), 263, 175

Forgan, E., in notes from the "Low temperature techniques course", (1991), Institute of Physics (UK)

Foxon, C.T., Harris, J.J., Hilton, D., Hewett, J. and Roberts, C., Semicond. Sci. Technol. (1989), 4, 582

Fukuyama, H., J. Phys. Soc. Jpn. (1984), 53, 1415

Glaser, E., Trombetta, J.M., Kennedy, T.A., Prokes, S.M., Glembocki, O.J., Wang, K.L. and Chern, C.H., Phys. Rev. Lett. (1990), 65, 1247

Gnutzmann, U. and Clausecker, Appl. Phys. (1974), 3, 9

Gold, A., Phys. Rev. B (1985), 32, 4014

Gold, A., Phys. Rev. B (1991), 44, 8818

Gold, A. and Dolgopolov, V.T., J. Phys. C: Solid St. Phys. (1985), 18, L463

Gold, A. and Dolgopolov, V.T., Phys. Rev. B (1986), 33, 1076

Gusev, G.M., Kvon, Z.D., Neizvestnyi, I.G., Ovsyuk, V.N. and Palkin, A.M., JETP Lett. (1982), 35, 256

Gusev, G.M., Kvon, Z.D., Neizvestnyi, I.G., Ovsyuk, V.N. and Cheremnykh, P.A., JETP Lett. (1984), 39, 541

Hall, R.N. and Racette, J.H., J. Appl. Phys. (1964), 35, 379

Harris, J.J., Pals, J.A. and Woltjer, R., Rep. Prog. Phys. (1989), 52, 1217

Higgs, V., Kightley, P., Goodhew, P.J. and Augustus, P.D., Appl. Phys. Lett. (1991), 59, 829

Hikami, S., Larkin, A.I. and Nagaoka, Y., Prog. Theor. Phys. (1980), 63, 707

Houghton, R.F., (1991), PhD Thesis, University of Warwick

Hull, R. and Bean, J.C., Appl. Phys. Lett. (1989), 55, 1900

Hull, R., Bean, J.C., Bonar, J.M., Higashi, G.S., Short, K.T., Temkin, H. and White, A.E., Appl. Phys. Lett. (1990), 56, 2445

Isawa, Y. and Fukuyama, H., J. Phys. Soc. Jpn. (1984), 53, 1415

Iyer, S.S., Patton, G.L., Stork, J.M.C., Meyerson, B.S. and Harame, D.L., IEEE Trans. Electron Dev. (1989), 36, 2043

Jesson, D.E., Pennycook, S.J., Baribeau, J.-M. and Houghton, D.C., Phys. Rev. Lett. (1992), 68, 2062

Jiang, C., Tsui, D.C. and Weimann, G., Appl. Phys. Lett. (1988), 53, 1533

Jonson, M., J. Phys. C: Solid State Phys. (1976), 9, 3055

Kasper, E., Herzog, H.J. and Kibbel, H., Appl. Phys. (1975), 8, 199

Kastner, M.A., Rev. Mod. Phys. (1992), 64, 849

Kawabata, A., Surf. Sci. (1982), 113, 527

Kelly, M.J. and Nicholas, R.J., Rep. Prog. Phys. (1985), 48, 1699

Kesan, V.P., Subbanna, S., Tejwani, M.J., Restle, P.J. and Iyer, S.S., MRS Proc. (1991), 220, 471

Khorram, S., Chern, C.H. and Wang, K.L., MRS Proc. (1991), 220, 181

Kh. Azhdarov, G., Kyazimzade, R.Z. and Mir-Bagirov, V.V., Sov. Phys. Semicond. (1992), 26, 314

Kubiak, R.A., Parker, E.H.C. and Iyer, S.S., in "Silicon Molecular Beam Epitaxy: Volume I", (1988), ed. Kasper and Bean, (CRC Press)

Kukushkin, I.V. and Timofeev, V.B., Sov. Phys. JETP (1988), 67, 594

Landau, L.D. and Lifshitz, I.M.: "Quantum Mechanics", (1977), 3rd Ed., Pergamon

Landwehr, G. and Uchida, S., Surf. Sci. (1986), 170, 719

Lee, P.A. and Ramakrishnan, T.V., Rev. Mod. Phys. (1985), 57, 287

Lee, K., Shur, M.S., Drummond, T.J. and Morkoç, H., J. Appl. Phys. (1983), 54, 6432

LeGoues, F.K., Copel, M. and Tromp, R., Phys. Rev. Lett. (1989), 63, 1826

Leong, W.Y., Kubiak, R.A. and Parker, E.H.C., in "Proceedings of the First International Symposium on Si MBE", (1985), 85-7, ed. Bean, J.C. (Electrochem. Soc., New Jersey)

Liou, H.K., Mei, P., Gennser, U. and Yang, E.S., Appl. Phys. Lett. (1991), 59, 1200

Lo, Y.H., Bhat, R., Hwang, D.M., Chua, C. and Lin, C.-H., Appl. Phys. Lett. (1993), 62, 1038

Lyo, S.K. and Fritz, I.J., Phys. Rev. B (1992), 46, 7931

Manasevit, H.M., Gergis, I.S. and Jones, A.B., Appl. Phys. Lett. (1982), 41, 464

Manku, T. and Nathan, A., Phys. Rev. B (1991), 43, 12634

Martin, R.W., Nicholas, R.J., Rees, G.J., Haywood, S.K., Mason, N.J. and Walker, P.J., Phys. Rev. B (1990), 42, 9237

Mattey, N.L., Whall, T.F., Biswas, R.G., Kubiak, R.A. and Kearney, M.J., Philos. Mag. B (1992), 66, 379

Matthews, J.W. and Blakeslee, A.E., J. Cryst. Growth (1974), 27, 118

Mendez, E.E. and Wang, W.I., Appl. Phys. Lett. (1985), 46, 1159

Mii, Y.J., Xie, Y.H., Fitzgerald, E.A., Monroe, D., Thiel, F.A., Weir, B.E. and Feldman, L.C., Appl. Phys. Lett. (1991), 59, 1611

Mishima, T., Fredriksz, C.W., van de Walle, G.F.A., Gravesteijn, D.J., van den Heuvel, R.A. and van Gorkum, A.A., Appl. Phys. Lett. (1990), 57, 2567

Morin, F.J. and Maita, J.P., Phys. Rev. (1954), 96, 28

Mott, N.F. and Davis, E.A.: "Electronic Processes in Non-crystalline Materials", 2nd Ed., (1979), Clarendon (Oxford)

Nelson, S.F., Ismail, K., Nocera, J.J., Fang, F.F., Mendez, E.E., Chu, J.O. and Meyerson, B.S., Appl. Phys. Lett. (1992), 61, 64

Ni, W.-X. and Hansson, G.V., Phys. Rev. B (1990), 42, 3030

Noble, D.B., Hoyt, J.L., Nix, W.D., Gibbons, J.F., Laderman, S.S., Turner, J.E. and Scott, M.P., Appl. Phys. Lett. (1991), 58, 1536

Nützel, J.F., Meier, F., Friess, E. and Abstreiter, G., Thin Solid Films (1992), 222, 150

Ogale, S.B. and Madhukar, A., J. Appl. Phys. (1984), 56, 368

Ono, Y., J. Phys. Soc. Jpn. (1982), 51, 237

Orlov, L.K., Kuznetsov, O.A., Rubtsova, R.A., Chernov, A.L., Gavrilenko, V.I., Mironov, O.A., Nikanorov, V.V., Skrylev, I.Yu. and Chistyakov, S.V., Sov. Phys. JETP (1990), 71, 573

Parry, C.P., Kubiak, R.A., Newstead, S.M., Whall, T.E. and Parker, E.H.C., MRS Proc. (1991a), 220, 103; *ibid.* (1991b), 220, 79

Pearsall, T.P., Bean, J.C., People, R. and Fiory, A.T., in "Proceedings of 1st International Symposium on Si MBE" (1985), ed. Bean, J.C., 85-7, 400, Electrochem. Soc. (New Jersey)

Pearson, G.L. and Bardeen, J., Phys. Rev. (1949), 75, 865

People, R., Bean, J.C., Lang, D.V., Sergent, A.M., Störmer, H.L., Wecht, K.W., Lynch, R.T. and Baldwin, K., Appl. Phys. Lett. (1984), 45, 1231

People, R., Bean, J.C. and Lang, D.V., J. Vac. Sci. Technol. A (1985), 3, 846

People, R., Phys. Rev. B (1985), 32, 1405

People, R. and Bean, J.C., Appl. Phys. Lett. (1986), 48, 538

People, R., Bean, J.C., Sputz, S.K., Bethea, C.G. and Peticolas, L.J., Thin Solid Films (1992), 222, 120

Pepper, M., Contemp. Phys. (1985), 26, 257

Pepper, M. and Wharam, D.A., Physics World (1988), 1(Oct.), 48

Pidduck, A.J., Robbins, D.J., Cullis, A.G., Leong, W.Y. and Pitt, A.M., Thin Solid Films (1992), 222, 78

Powell, A.R., Kubiak, R.A., Whall, T.E., Parker, E.H.C. and Bowen, D.K., MRS Proc. (1991), 220, 277

Powell, A.R., Kubiak, R.A., Parker, E.H.C., Bowen, D.K. and Polcarova, M., Proceedings of the "Advances in surface and thin film diffraction" symposium of the 1990 MRS Fall meeting

Powell, A.R., Bowen, D.K., Wormington, M., Kubiak, R.A., Parker, E.H.C., Hudson, J. and Augustus, P.D., Semicond. Sci. Technol. (1992), 7, 627

Presting, H., Kibbel, H., Jaros, M., Turton, R.M., Menczigar, Abstreiter, G. and Grimmeiss, H.G., Semicond. Sci. Technol. (1992), 7, 1127

Sakomoto, K., Miki, K., Sakamoto, T., Yamaguchi, H., Oyanagi, H. and Matsuhata, H.: the figure quoted for incorporation of Sb when used as a surfactant was given orally at the EMRS Spring Meeting (1992), but was not mentioned in the written version of the work [Thin Solid Films (1992), 222, 112]

Sajoto, T., Suen, Y.W., Engel, L.W., Santos, M.B. and Shayegan, M., Phys. Rev. B (1990), 41, 8449

Schäffler, F., Többen, D., Herzog, H.-J., Abstreiter, G. and Holländer, B., Semicond. Sci. Technol. (1992), 7, 260

Smith, D.W., Emeleus, C.J., Kubiak, R.A., Parker, E.H.C. and Whall, T.E., Appl. Phys. Lett. (1992), 61, 1453

Smith, R.P. and Stiles, P.J., Solid State Comm. (1986), 58, 511

Spanier, J. and Oldham, K.B.: "An Atlas of Functions", (1979), Chapter 44 (The Digamma Function), Hemisphere (Washington)

Stern, F., Phys. Rev. Lett. (1980), 44, 1469

Störmer, H.L., Schlesinger, Z., Chang, A., Tsui, D.C., Gossard, A.C. and Wiegmann, W., Phys. Rev. Lett. (1983), 51, 126

Sze, S.M.: "The Physics of Semiconductor Devices", (1982), 2nd Edition, Wiley-Interscience

Thornton, T.J., Pepper, M., Ahmed, H., Andrews, D. and Davies, G.J., Phys. Rev. Lett. (1986), 56, 1198

Timbrell, P.Y., Baribeau, J.-M., Lockwood, D.J. and McCaffrey, J.P., J. Appl. Phys. (1990), 67, 6292

Többen, D., Schäffler, F., Zrenner, A. and Abstreiter, G., Thin Solid Films (1992), 222, 15

Tremblay, F., Pepper, M., Newbury, R., Ritchie, D.A., Peacock, D.C., Frost, J.E.F., Jones, G.A.C. and Hill, G., J. Phys. C. M. (1990), 2, 7367

Uren, M.J., Davies, R.A. and Pepper, M., J. Phys. C: Solid St. Phys. (1980), 13, L985

Uren, M.J., Davies, R.A., Kaveh, M. and Pepper, M., J. Phys. C: Solid State Phys. (1981), 14, 5737

Van de Walle, C.G. and Martin, R.M., Phys. Rev. B(1986), 34, 5621

Van der Merwe, J. H., J. Appl. Phys. (1963), 34, 123

Van der Pauw, L.J., Philips Research Reports (1958), 13, 1

Van der Pauw, L.J., Philips Technical Review (1958/59), 20, 220

Venkataraman, V., Schwartz, P.V. and Sturm, J.C., Appl. Phys. Lett. (1991), 59, 2871

Versnel, W., Solid-State Electronics (1979), 22, 911

Vinter, B., Appl. Phys. Lett. (1984), 45, 581

Von Klitzing, K., Dorda, G. and Pepper, M., Phys. Rev. Lett. (1980), 45, 494

Vyrodov, E.A., Dolgopolov, V.T., Dorozhkin, C.I. and Zhitenev, N.B., Sov. Phys. JETP (1988), 67, 998

Wang, P.J., Meyerson, B.S., Fang, F.F., Nocera, J. and Parker, B., Appl. Phys. Lett. (1990a), 54, 2701; *ibid.* (1990b), 55, 2333

Wang, X.-F., Wang, Z., Kotliar, G. and Castellani, C., Phys. Rev. Lett. (1992), 68, 2504

Washburn, S. and Webb, R.A., Rep. Prog. Phys. (1992), 55, 1311

Weisbuch, C. and Vinter, B.: "Quantum Semiconductor Structures", (1991), Academic Press (London)

Wieder, H.H.: "Laboratory notes on electrical and galvanomagnetic measurements", (1979), Elsevier (Amsterdam)

Yu, E.T., Croke, E.T., Chow, D.H., Collins, D.A., Phillips, M.C., McGill, T.C. and McCaldin, J.O., J. Vac. Sci. Technol. B (1990), 8, 908

Zalm, P.C., van de Walle, G.F.A., Gravesteijn, D.J. and van Gorkum, A.A., Appl. Phys. Lett. (1989), 55, 2520